Interphases Between Alkali Metals (Li, Na) and Battery Electrolytes: Ion Transport and Growth Behavior

Von der Fakultät Chemie der Universität Stuttgart

zur Erlangung der Würde eines

Doktors der Naturwissenschaften

(Dr. rer. nat.) genehmigte Abhandlung

Vorgelegt von

Kyungmi Lim

aus Seoul, Republik Korea

Hauptberichter: Prof. Dr. Joachim Maier

Mitberichter: Prof. Dr. Oliver Clemens

Prüfungsvorsitzender: Prof. Dr. Rainer Niewa

Tag der mündlichen Prüfung: 14.07.2022

Max-Planck-Institut für Festkörperforschung

Stuttgart

2022

You cannot connect the dots looking forward; you can only connect them looking backwards.

So you have to trust that the dots will somehow connect in your life.

-Steve Jobs

Abstract

Secondary batteries are of great importance in a variety of electrochemical energy storage applications such as portable devices and electrical vehicles. One of the most important future directions for the battery development is increasing the energy density. Li and Na metal batteries hold great advantages in terms of energy density, but the high chemical reactivity of alkali metals leads to the continuous formation of solid-electrolyte interphase (SEI) at the alkali metal/electrolyte interface. SEI is critical for stable battery operation, as it is responsible for capacity retention upon cycling and overpotential in the electrochemical cells. From the fundamental point of view, these battery operation behaviors originate from the ion transport in the SEI and the SEI growth.

In this work, ion transport and growth behavior of the SEIs on Li and Na are investigated by a systematic combination of electrochemical and chemical characterizations. Two different types of SEIs are examined: i) SEIs formed spontaneously by the contact with liquid electrolyte in the electrochemical cells and ii) SEIs synthesized prior to the cell assembly (i.e., artificial SEIs). Studying of the former one provides understanding about the ion transport and growth behavior of SEIs occurring in next generation battery technologies (e.g. metal-sulfur, metal-oxygen). Using artificial SEIs has been suggested in the previous literature as a key method towards application of alkali metal batteries. However, the ion transport mechanism in the artificial SEIs, as well as their chemical/mechanical stability over the storage under open-circuit have not been inspected in detail.

The first part of this thesis deals with ion transport and growth behavior of SEIs formed spontaneously on contact with the liquid electrolytes. Prior to the main discussion, native films on Li and Na are investigated. The chemical characterizations on bare Li and Na reveal that they are partially covered with native films composed of oxides, hydroxides, carbonates and fluorides. Li films synthesized with molecular beam epitaxy (MBE) are compared with freshly cut commercial Li, as MBE-synthesized-Li is believed to have higher purity owing to the high-vacuum

environment (~10^{-11} mbar) during its synthesis. The results show that MBE-synthesized-Li has similar native films as the bulk commercial Li in terms of chemical composition, implying that the native films stemmed from the storage environment (glovebox, airtight transfer tools, or measurement chamber). Next, electrochemical impedance spectroscopy (EIS) was performed in four different electrochemical cell systems, which are symmetric Li and Na cells with glyme- and carbonate-based liquid electrolytes. The activation energies of ion transport in the SEIs (E_a(SEI)), derived from the SEI resistances at different temperatures, are treated as a key factor to determine the major ion transport pathways (either liquid in the pores or solid SEI constituents), as they are independent to the SEI's morphological structure which is difficult to be characterized in detail. When the particular electrolytes (i.e. glyme- and carbonate-based liquid electrolytes) are used, SEIs on Na are revealed to have smaller E_a(SEI) compared to the one on Li, indicating the major transport pathways on Na SEIs are the liquid ones. This means that the solid part of SEIs on Na are more porous compared to the SEIs on Li. The following morphological/chemical characterizations with tools such as focused-ion beam-scanning electron microscopy (FIB-SEM), X-ray photoelectron spectroscopy (XPS) and time-of-flight secondary ion mass spectroscopy (ToF-SIMS) support the higher porosity in the Na SEIs. The porosity of the SEIs on Na is believed to originate from the smaller molar volumes of the reaction products (inorganic SEI components) in comparison to the molar volume of Na metal.

Additionally, the ion transport properties of the bulk liquid electrolytes used in the previous EIS measurements are investigated. Cation transference numbers and salt diffusion coefficients of the liquid electrolytes are determined with a galvanostatic polarization method, and the difference between Li and Na electrolytes are discussed. Finally, stripping-plating cyclic behavior was tested on Li and Na symmetric cells with glyme- and carbonate-based liquid electrolytes. The results indicate that the denser SEIs are not electrochemically beneficial in such processes, most possibly owing to their high electrical resistivity and poor mechanical properties.

Based on the previous understanding about the ion transport and growth behavior on Li and Na with the liquid electrolytes, a suitable equivalent circuit model for the porous SEI is developed.

The model takes account of the channels (in reality pores in the SEI) where the liquid electrolyte is infiltrated. As the electrolyte contacts with the metal, a thin SEI forms within the channels. Depending on the molar volume change during the reaction, it either equally grows and closes the channels, or breaks up and forms pores on a smaller scale. The latter phenomenon more applies to the Na cases. On the basis of the E_a(SEI) values and the measured frequency ranges in EIS, it is concluded that at early stage of storage, the SEI resistance is dominated by the liquid in the channel while the SEI capacitance is dominated by the solid part in which the channel is embedded.

The second part of this thesis examines the ion transport and growth behavior of the two types of the artificial SEIs (sulfide-based SEIs and Al_2O_3) with liquid and solid electrolytes. The sulfide-based artificial SEIs were synthesized by a chemical reaction between Li/Na and S vapor. The chemical characterizations with FIB-SEM, X-ray diffraction (XRD), XPS and ToF-SIMS reveal that in the sulfide-based SEIs, the concentration gradients of Li/Na and S are established throughout the layers (i.e. surface is covered with polysulfides while the bulk consists of sulfides), and the one on Na (Na_xS_y) is more porous compared to the one on Li (Li_xS_y). The EIS measurements on the symmetric Li/Na cells with sulfide-based artificial SEIs in combination with the liquid and solid electrolytes under open-circuit show that the Li_xS_y/Na_xS_y film surfaces are composed of polysulfides, and imply that Na_xS_y is more porous than Li_xS_y. The stripping-plating behavior of all-solid-state symmetric Li/Na cells with the sulfide-based artificial SEIs is compared to the ones without the artificial SEIs. The results demonstrate that the artificial SEIs are more resistive than the one formed spontaneously by the contact between the alkali metals and the solid electrolytes, and they are not stable over the cyclic stripping-plating, especially for Na case. Finally, Al_2O_3 was synthesized by atomic layer deposition (ALD) on Li and Na and such electrodes were assembled in the electrochemical cells with the glyme-based liquid electrolyte, and subsequently measured with EIS. Theoretically, Al_2O_3 thin film is blocking for both electrons and ions, but the EIS results show relatively small SEI resistances and E_a(SEI) values in comparison to the completely-blocking interface. This strongly suggests that the synthesized Al_2O_3 is also porous,

allowing for liquid electrolyte infiltration into the pores, and subsequent formation of another SEIs on the surface of the alkali metals.

In summary, the present thesis focuses on the ion transport and growth behavior of the spontaneously-formed SEIs (by the contact with the electrolytes) and the artificial SEIs in contact with the liquid and solid electrolytes in light of the SEI porosity. All the results together strongly show that the porosity plays an essential role in the ion transport and the growth behavior of the SEI on Li and Na, as the SEI pores become either major transport pathways when the liquid electrolyte is utilized, or the space allowing the metal to creep. Both phenomena result in a direct contact between the alkali metals and the electrolyte, leading to continuous SEI formation. Therefore, the porosity of the SEI should be carefully taken into account in battery applications.

Zusammenfassung

Sekundärbatterien sind in einer Vielzahl von elektrochemischen Energiespeicheranwendungen, wie tragbaren Geräten und Elektrofahrzeugen, von großer Bedeutung. Eine der wichtigsten zukünftigen Richtungen für die Batterieentwicklung ist die Erhöhung der Energiedichte. Li- und Na-Metallbatterien haben große Vorteile in Bezug auf die Energiedichte, aber die hohe chemische Reaktivität von Alkalimetallen führt zur kontinuierlichen Bildung einer Festelektrolyt-Zwischenphase (solid-electrolyte interphase, SEI) an der Alkalimetall/Elektrolyt-Grenzfläche. Dieses SEI ist entscheidend für einen stabilen Batteriebetrieb, da es für die Kapazitätserhaltung beim Zyklisieren sowie für die Überspannung in der elektrochemischen Zelle verantwortlich ist, aus fundamentaler Sicht ist das Betriebsverhalten der Batterie auf den Ionentransport in der SEI und das SEI-Wachstum zurückzuführen.

In dieser Arbeit werden Ionentransport und Wachstumsverhalten der SEIs auf Li und Na durch eine systematische Kombination von elektrochemischen und chemischen Charakterisierungen untersucht. Zwei verschiedene Arten von SEIs werden untersucht: i) SEIs, die spontan durch den Kontakt mit flüssigem Elektrolyt in den elektrochemischen Zellen gebildet werden, und ii) SEIs, die vor dem Zellzusammenbau synthetisiert werden (künstliche SEIs). Das Studium der ersteren trägt zum Verständnis des Ionentransports und des Wachstumsverhaltens von SEIs bei, welche in den meisten Batterietechnologien der nächsten Generation auftreten (z. B. Metall-Schwefel, Metall-Sauerstoff). Künstliche SEIs wurden in der früheren Literatur als Schlüsselverfahren zur Anwendung von Alkalimetallbatterien vorgeschlagen. Der Ionentransportmechanismus in den künstlichen SEIs sowie deren chemische/mechanische Stabilität während der Lagerung im Leerlauf wurden jedoch bislang noch nicht im Detail untersucht.

Der erste Teil dieser Arbeit befasst sich mit dem Ionentransport und dem Wachstumsverhalten von SEIs, welche spontan durch den Kontakt der Alkalimetalle mit flüssigen Elektrolyten gebildet werden. Vor der Hauptdiskussion werden die nativen Filme untersucht. Die chemischen

Charakterisierungen des blanken Li und Na zeigen, dass diese teilweise mit nativen Filmen bedeckt sind, die aus Oxiden, Hydroxiden, Carbonaten und Fluoriden bestehen. Der mit Molekularstrahlepitaxie (MBE) synthetisierte Li-Film wird mit dem Verhalten von frisch geschnittenem kommerziellem Li verglichen, da angenommen wird, dass MBE-synthetisiertes Li aufgrund der Hochvakuumumgebung während der Synthese (~10^{-11} mbar) eine höhere Reinheit aufweist seine Synthese. Die Ergebnisse zeigen, dass MBE-synthetisiertes Li in Bezug auf die chemische Zusammensetzung ähnliche native Filme aufweist wie kommerzielles Li, was darauf hindeutet, dass die nativen Filme aus der Lagerumgebung stammen (Glovebox, luftdichte Transferwerkzeuge oder Messkammer). Elektrochemische Impedanzspektroskopie (EIS) wurden in vier verschiedenen elektrochemischen Zellsystemen durchgeführt, bei denen es sich um symmetrische Li- und Na-Zellen mit Flüssigelektrolyten auf Glyme- und Carbonatbasis durchgeführt. Die Aktivierungsenergien des Ionentransports in den SEIs (E_a(SEI)), lassen sich aus den mithilfe der EIS gemessenen Widerständen der SEI bei verschiedenen Temperaturen berechnen. Diese werden als Schlüsselfaktor zur Bestimmung der wichtigsten Ionentransportwege (entweder Flüssigkeit in den Poren oder feste SEI) behandelt, da die morphologische Struktur der SEIs im Detail schwer zu charakterisieren ist. Die auf Na gebildeten SEIs weisen ein kleineres E_a(SEI) auf als SEIs auf Li, was darauf hindeutet, dass bei Na-SEIs der Ionentransport hauptsächlich über die Flüssigkeit in der Poren geschieht und der feste Teil der SEIs auf Na poröser ist als dieses bei den SEIs auf Li der Fall ist. Zusätzliche morphologischen/chemischen Untersuchungen mit Werkzeugen wie fokussierter Ionenstrahl-Rasterelektronenmikroskopie (FIB-SEM), Röntgen-Photoelektronenspektroskopie (XPS) und Flugzeit-Sekundärionen-Massenspektroskopie (ToF-SIMS) unterstützen die elektrochemische Beobachtung der Porosität der Na SEIs. Es wird angenommen, dass die Porosität von SEI auf Na auf das kleinere Molvolumen der Reaktionsprodukte (anorganische SEI-Komponenten) im Vergleich zum Molvolumen von Na-Metall zurückzuführen ist.

Zusätzlich werden die Ionentransporteigenschaften der in den vorherigen EIS-Messungen verwendeten Bulk-Flüssigelektrolyte untersucht. Kationenübertragungszahlen und

Salzdiffusionskoeffizienten der verwendeten Flüssigelektrolyte wurden mit galvanostatischer Polarisation bestimmt und der Unterschied zwischen Li- und Na-Elektrolyten diskutiert. Zudem wurde das zyklische Verhalten (z. B. Stripping-Plating) an Li- und Na-symmetrischen Zellen mit flüssigen Elektrolyten auf Glyme- und Carbonatbasis durchgeführt. Die Ergebnisse zeigen, dass die dichteren SEIs in solchen Prozessen elektrochemisch nicht vorteilhaft sind, was höchstwahrscheinlich auf ihren hohen spezifischen elektrischen Widerstand und ihre schlechten mechanischen Eigenschaften zurückzuführen ist.

Basierend auf dem bisherigen Verständnis des Ionentransports und des Wachstumsverhaltens der SEIs auf Li und Na mit flüssigen Elektrolyten wird ein geeignetes Ersatzschaltbildmodell für poröse SEI entwickelt. Das Modell berücksichtigt die Kanäle (in Wirklichkeit Poren der SEI), in welche der flüssige Elektrolyt eindringt. Zwei Extremfälle können unterschieden werden: Entweder wächst die Kontaktschicht im Kanal schnell und verschließt diesen oder - im Falle extremer Reaktionsvolumina, wie es bei Na häufig der Fall ist – er bricht auf und wird selber porös. Aufgrund der E_a(SEI)-Werte und der mit EIS gemessenen Frequenzbereiche wird geschlussfolgert, dass der SEI-Widerstand von der Flüssigkeit im Kanal dominiert wird, während die SEI-Kapazität von der bulk-SEI dominiert wird.

Der zweite Teil dieser Arbeit untersucht den Ionentransport und das Wachstumsverhalten zweier Arten künstlicher SEIs (sulfidbasierte SEIs und Al_2O_3) mit flüssigen und festen Elektrolyten. Die künstlichen SEIs auf Sulfidbasis wurden durch Aufdampfen von Schwefel auf Li und Na hergestellt. Die chemischen Charakterisierungen mit FIB-SEM, Röntgenbeugung (XRD), XPS und ToF-SIMS zeigen einen zur Oberfläche orthogonalen Konzentrationsgradienten: Die Oberfläche ist mit Polysulfiden bedeckt während tieferliegende Schichten aus Sulfiden bestehen; die sulfidbasierte SEI auf Na (Na_xS_y) ist poröser als die SEI auf Li (Li_xS_y). Die EIS-Messungen an den symmetrischen Li/Na-Zellen mit künstlichen SEIs auf Sulfidbasis in Kombination mit den flüssigen und festen Elektrolyten im Leerlauf zeigen, dass die Li_xS_y/ Na_xS_y-Filmoberflächen aus Polysulfiden bestehen und dass Na_xS_y poröser ist als Li_xS_y. Das Stripping-Plating-Verhalten von symmetrischen Li/Na-Festkörperzellen mit künstlichen SEIs auf

Sulfidbasis wird mit denen ohne künstliche SEIs verglichen. Die Ergebnisse zeigen, dass die künstlichen SEIs widerstandsfähiger sind als die, die spontan durch den Kontakt zwischen den Alkalimetallen und den Festelektrolyten gebildet werden, und dass sie über das zyklische Stripping-Plating hinweg nicht stabil sind, insbesondere im Na-Fall. Zudem wurde Al_2O_3 durch Atomlagenabscheidung (ALD) auf Li und Na synthetisiert aufgetragen, diese Elektroden wurden in den elektrochemischen Zellen mit dem auf Glyme basierenden flüssigen Elektrolyten zusammengesetzt und anschließend mit EIS gemessen. Theoretisch blockiert der Al_2O_3-Dünnfilm sowohl Elektronen als auch Ionen, aber die EIS-Ergebnisse zeigen relativ kleine SEI-Widerstände und E_a(SEI)-Werte im Vergleich zu der vollständig blockierenden Grenzfläche. Dies deutet stark darauf hin, dass das synthetisierte Al_2O_3 ebenfalls porös ist, was das Eindringen des flüssigen Elektrolyten in die Poren und die anschließende Bildung weiterer SEIs auf der Oberfläche der Alkalimetalle ermöglicht.

Zusammenfassend konzentriert sich die vorliegende Arbeit auf den Ionentransport und das Wachstumsverhalten der spontan durch Kontakt mit den Elektrolyten gebildeten SEIs und der künstlichen SEIs in Kontakt mit den flüssigen und festen Elektrolyten im Hinblick auf die Porosität der SEI. Alle Ergebnisse zusammen zeigen deutlich, dass die Porosität eine wesentliche Rolle für den Ionentransport und das Wachstumsverhalten der SEI auf Li und Na spielt, da die SEI-Poren entweder zu Haupttransportwegen werden, wenn der flüssige Elektrolyt verwendet wird, oder dem Metall Raum zum Kriechen bieten. Beide Phänomene führen zu einem physikalischen Kontakt zwischen den Alkalimetallen und den Elektrolyten, was zu einem kontinuierlichen SEI-Wachstum führt, daher sollte die Porosität des SEI sorgfältig berücksichtigt werden.

Contents

1. Introduction 1

1.1. Motivation and goals 1

1.2. Survey of past solid-electrolyte interphase (SEI) research 4

1.2.1. Formation and growth of SEI 4

1.2.2. Ion transport in SEI 7

1.2.3. Artificial SEI 10

2. Experimental methods 11

2.1. Sample preparation 11

2.1.1. Li/Na metal electrode and liquid electrolyte preparation 11

2.1.2. Synthesis of sulfide-based solid electrolytes and artificial SEIs 12

2.1.3. Li thin film synthesis with molecular beam epitaxy 14

2.2. Characterization 14

2.2.1. Chemical and morphological characterization 14

2.2.2. Cell assembly and electrochemical measurements 16

3. SEIs on Li/Na formed by the contact with liquid electrolytes 23

3.1. Native films on Li and Na 23

3.2. Ion transport in SEI 28

3.2.1. Impedance results of symmetric Li/Na cells with salt-free triglyme solvent 28

3.2.2. Impedance results of symmetric Li/Na cells with glyme- and carbonate-based liquid electrolytes 33

3.2.3. Morphology of SEI on Li/Na: FIB-SEM results 37

3.2.4. Chemical composition of the SEIs over depth: XPS and ToF-SIMS results 40

3.2.5. Origin of the porosity of Na SEIs 44

3.2.6. Cation transference number and salt diffusion coefficient of the liquid electrolytes....46
3.2.7. Stripping-plating results of symmetric Li/Na cells....50
3.3. Equivalent circuit models for the ion transport in the porous SEI....53
3.4. Long-term SEI growth behavior under open-circuit potential....62
3.5. Conclusion....67
4. Artificially-formed SEIs on Li/Na....69
4.1. Sulfide-based SEIs formed by solid-vapor chemical reaction....69
4.1.1. Morphological and chemical characterization of sulfide-based SEIs on Li/Na....69
4.1.2. SEI growth behavior in contact with liquid/solid electrolytes under open-circuit condition....74
4.1.3. Performance in all-solid-state batteries: Stripping-plating results....83
4.2. Al_2O_3 SEIs formed by atomic layer deposition....85
4.2.1. Electrochemical impedance spectroscopy of symmetric Al_2O_3-Li/Na cells with liquid electrolytes....85
4.2.2. Morphological and chemical characterization of Al_2O_3 on Li....91
4.3. Conclusion....96
5. Summary, conclusion and outlook....97
List of symbols and abbreviations....99
Acknowledgements....101
References....103

1. Introduction

1.1. Motivation and goals

One undeniable fact is that the climate change crisis is now facing us. [2] One of ways to deal with this issue is to replace the internal combustion engine-vehicles with electric vehicles and increase the use of renewable energy, both of which require the development of energy storage system with high energy density. [3-5] Li metal batteries and Na metal batteries, the batteries in which metallic Li and Na are used as anode, have been in the spotlight of a next-generation technologies due to their high gravimetric energy densities (3,860 mAh g^{-1} and 1,166 mAh g^{-1} for Li and Na, respectively) when compared with cells using of graphite (372 mAh g^{-1}) as anode. [6, 7] Yet their commercialization remains hindered by the high chemical reactivity of Li/Na with most liquid and solid electrolytes. [8] The chemical reaction between Li/Na and electrolytes results in the formation of solid electrolyte interphase (SEI), an interfacial layer composed of a variety of organic/inorganic phases with the thickness ranging from several nm to hundreds of nm or thicker, depending on the type of the electrolyte/anode material. The SEI has been pinpointed as a key factor for successful battery operation in terms of their power capability and cycle life, since SEI becomes a bottleneck of ion transport in many cases. In addition, chemo-mechanically unstable SEI leads to continuous electrolyte consumption, and eventually to cell failure. [9-11] In order to have a desirable performance of batteries, SEI should be an ionic conductor (with no considerable electronic conductivity) and chemo-mechanically stable during the storage under open-circuit condition as well as upon electrochemical cycling. [12] Additionally, chemical and morphological homogeneity is required, especially for Li/Na metal batteries, in order to prevent the preferable

Li/Na deposition on the specific sites, as this can lead to dendrite formation. [13] Ever since the concept of the SEI was first proposed by E. Peled in 1979 [14], SEI has been studied for decades by a number of scientists. [8, 9, 15, 16] However, studies on SEI still have a long way to go, as its growth behavior and ion transport mechanism has not been fully elucidated owing to a high level of complexity as well as experimental issues related to air-sensitivity and nano-structure. [8, 17-20]

The present thesis deals with fundamental questions related to ion transport in and the growth of SEI on Li and Na. Two types of SEI are studied here: SEI formed spontaneously after the contact of alkali metals with liquid electrolytes under open circuit, and artificial SEIs (sulfide-based SEI and Al_2O_3) formed *ex situ*, prior to electrochemical cell assembly. [21]

In the first part, the growth and transport mechanism of SEIs on Li and Na formed spontaneously by the contact with glyme- and carbonate-based electrolytes are examined by combining electrochemical measurements such as temperature- and time-dependent electrochemical impedance spectroscopy (EIS), and chemical characterization (focused ion beam-scanning electron microscopy, FIB-SEM); X-ray photoelectron spectroscopy, XPS; and time-of-flight secondary ion mass spectroscopy, ToF-SIMS). The analysis of the activation energy of transport (E_a) is shown to be the key information to understand the ion transport in the SEI. SEIs on Li and Na are systematically compared in terms of their porosity, and the suitable equivalent circuit model of EIS to account for the transport and growth of the porous SEI is developed. Finally, the long-term (~600 hours) growth behavior of the SEIs on Li and Na under open-circuit condition is observed and explained in terms of SEI densification and mechanical instability.

Second part of the thesis deals with two different artificial SEIs (sulfide-based SEIs and Al_2O_3) synthesized by chemical reaction between Li/Na and S vapor and atomic-layer deposition (ALD),

respectively. Sulfide-based SEIs are selected since both Li_2S and Na_2S are known to be pure ion conductors [22, 23]. The Al_2O_3-SEI was chosen as a model system to study SEI porosity, as it is a material with negligible ionic/electronic conductivity. Chemical composition and morphology of the artificial SEIs are investigated in detail by X-ray diffraction (XRD), XPS, ToF-SIMS, energy-dispersive X-ray (EDX) and FIB-SEM in consideration of porosity. Electrochemical tests (EIS and stripping-plating) in symmetric cells with liquid/solid electrolytes examine the role of artificial SEIs in battery systems in terms of the ion transport mechanism and interfacial changes.

In summary, this thesis contributes to the fundamental understanding of the SEI on Li/Na by dealing with different types of SEI combining electrochemical/chemical/morphological inspection tools. The consideration of the porosity of SEI is stressed for the first time in depth, not only for the spontaneously-formed SEI but also for the artificial SEI.

1.2. Survey of past solid-electrolyte interphase (SEI) research

1.2.1. Formation and growth of SEI

The high Li/Na chemical potential of metallic Li/Na triggers the chemical reaction with liquid/solid electrolytes. The driving force of the reaction, which is the Gibbs free energy difference between reactants (Li or Na and electrolyte) and products (SEI), can be described by the equation of the chemical potential of each compound.

$$\Delta_R G = \sum_i N^i_{reaction\ product}\mu^i_{reaction\ product} - N_{alkali\ metal}\mu_{alkali\ metal} - \sum_j N^i_{electrolyte}\mu^i_{electrolyte} \quad (1.1)$$

where $\Delta_R G$ is a Gibbs free energy change over the reaction, $\mu^i_{reaction\ product}$, $\mu_{alkali\ metal}$ and $\mu^i_{electrolyte}$ are chemical potentials of each reaction product (includes SEI compounds and the released gas), alkali metal, and each single electrolyte molecule, and N^i_{SEI}, $N_{alkali\ metal}$ and $N^i_{electrolyte}$ are the stoichiometric coefficients of SEI compounds, alkali metal and electrolyte molecules, according to the reaction equation. The same equation applies to Na. When $|\Delta_R G| \ll RT$, the reaction rate and, if the rate is directly translated into transport (no storage), also the particle flux (J) is proportional to the reaction driving force. [24]

$$J \propto -\Delta_R G \quad (1.2)$$

The driving force of the SEI formation is often explained only by the disparity between the electric potential of Li (or Na) and the level of the lowest unoccupied molecular orbital (LUMO) for liquid electrolyte (or conduction band in case of solid electrolyte). [25, 26] However, since the actual decomposition involves local free energy of forming neutral Li (or Na), electrolytes and SEI compounds, all chemical components participating the chemical reaction should be considered.

[27, 28] In reality, the defined kinetics is characterized by a complex interplay of local reactions and transport processes.

The previous studies revealed that SEIs on carbons or alkali metals are generally thin films (few nm to hundreds of nm, depending on the chemical environment) with a complex and heterogeneous structure. [29-31] The SEI structure is considered to be composed of inorganic inner layer in the vicinity of Li (or Na) (LiF, Li_2CO_3, Li_2O, LiOH, Li_2S, etc) and the organic layer at the inorganic layer/electrolyte interface (dilithium ethylene glycol dicarbonate, Li_2EDC; ROLi, where R refers to functional group which depends on the used solvent). [11, 15, 32-34] Observing the chemical composition and crystal structure of the SEI on alkali metals experimentally in a precise way is a highly challenging task, owing to its air-sensitivity and inherently fragile SEI morphology. [35] A number of novel experimental tools have been developed to investigate the chemo-mechanical properties of SEI, including cryo-transmission electron microscopy (TEM) [36-39], X-ray-based analytical tools [40-42], nuclear magnetic resonance (NMR) spectroscopy [39, 43-47], X-ray photoelectron spectroscopy [16, 48, 49] and Fourier-transform infrared spectroscopy (FT-IR) [16].

Capturing the chemical reaction between Li (or Na) and electrolyte is another challenging work as the reactions accompany a variety of chemical compounds (Li or Na, salts, organic solvents and impurities) and as they could occur at different timescales. [15] Therefore, based on the observed chemistry of the SEI and the fact that gases (H_2, C_2H_4, CO and CO_2) are produced during the chemical reaction [50, 51], quantum chemistry and molecular dynamics simulations have been employed to discover the reaction routes. As a characteristic example, the following reaction scheme for the reaction of Li with carbonate-based liquid electrolytes suggested by theory shall be given as follows. [52-55]

$$EC\text{-}Li^+ + e^- \rightarrow C_2H_4OCO_2^- + Li^+ \quad (1.3)$$

$$2(EC\text{-}Li^+) + 2e^- \rightarrow Li_2EDC + C_2H_4\uparrow \quad (1.4)$$

$$EC + 2Li^+ + 2e^- \rightarrow Li_2CO_3 + C_2H_4\uparrow \quad (1.5)$$

$$EC + 2e^- \rightarrow OC_2H_4O^{2-} + CO\uparrow \quad (1.6)$$

$$LiPF_6 \rightarrow LiF + PF_5 \quad (1.7)$$

$$LiPF_6 + H_2O \rightarrow LiF + POF_3 + 2HF \quad (1.8)$$

Note that the above reactions are only a small part of manifold reaction pathways that can be found the literature. [56] The comprehensive and precise picture of the chemical reaction mechanism remains to be elaborated for any of the SEI formation reactions.

Another factor that should be taken into account is that the electrochemical reaction (*i.e.* reaction accompanying electron transfer) can be driven by the applied current or potential. According to the transition state theory, the reaction rate of the electrochemical reaction with single electron process can be described by a function of the applied potential and the concentration of the reactants and products. [57] The present thesis, however, only deals with the situations where such effects can be excluded, since rather small potential (~0.01 V) is applied to the electrochemical cells only during the EIS measurements. The influence of the applied potential on the SEI formation becomes critical in the actual battery operations.

The SEI growth mechanism under open-circuit is complex. Usually SEI growth has been agreed to be a diffusion-controlled reaction which in the ideal case follows a parabolic law [58-62], similar to the oxidation models developed by Wagner [63] Evans [64], Deal and Grove [65], and Cabrera and Mott [66]. These theories have been developed for the formation of uniform and dense layer of oxides on metals (or Si) where oxidation is driven only by the oxygen (or metal) diffusion within the oxide layers. However, recent statistical analyses show that SEI growth does not always scale with $t^{0.5}$, since SEI growth may not necessarily be diffusion-limited, or SEI is

morphologically complex. [67] In a real situation, other factors such as space charge effects [68], three-dimensional morphologies [11], electron tunneling [60], and a variety of chemical reactions having different reaction orders make the growth behavior more complicated. One of the simplest way to predict whether the formed oxide film is dense or porous is to examine the ratio between the molar volume of the product and the one of initial material, which is called Pilling-Bedworth ratio (R_{PB}).[69] When the molar volume of the products (e.g. SEI components) is smaller or much greater than the molar volume of Li or Na metal (R_{PB}<1 or R_{PB}>>1), the reaction layer is non-passivating as the formed layer will be porous or has cracked. This kind of passivating layer allows the infiltration of the liquid electrolytes, finally resulting in quick and continuous chemical reactions between alkali metals and electrolytes.

1.2.2. Ion transport in SEI

The thermodynamics of ion transport is represented by ionic conductivity (σ) which can be described as

$$\sigma = |z|Fcu \tag{1.9}$$

where z is a charge number, F is the Faraday constant, c is ion concentration and u is mobility. The ionic conductivity follows the Arrhenius equation.

$$\sigma T = Aexp(-\frac{E_a}{k_B T}) \tag{1.10}$$

where E_a is the activation energy for ion transport, A is the Arrhenius prefactor at infinite temperature, and k_B is the Boltzmann constant. In the present thesis, E_a, rather than resistance, is considered to be a critical indicator for the determination of the nature of ion transport. Only for an extended laterally homogenous film, geometrical factor is simple ($R_{SEI} = \frac{d}{\sigma A}$, d is a thickness

and *A* is the surface area). However, SEI has a complex geometry, which is experimentally difficult to be identified.

The electrical conductivities as well as activation energies of ion transport of the Li/Na SEI compounds measured experimentally in the literature are summarized in Table 1 and Table *2*. Generally, bulk organic/inorganic SEI compounds are poor ionic conductors with ionic conductivities smaller than 10^{-11} S cm^{-1}. However, the observed SEI resistances with liquid/solid electrolytes are only hundreds to thousands of Ω. [70, 71] This means that they typically do not block ion transport from Li/Na to electrolyte, and the SEI conductivities are higher than the values for the respective bulk SEI compounds. Even though doping could vary the conductivities greatly [22, 72-74], it is very likely that higher-dimensional defects and interfaces are involved. [75, 76] This can offer passages due to higher mobility (e.g. dislocations) but also higher carrier concentration (e.g. space charges). Pores play a particularly important role here. [77] If the pores are filled by electrolyte, these particular channels may become the major transport pathways, since ion conduction in liquid electrolyte is much more favorable due to its high ionic conductivities and low activation energies of the liquid electrolyte. [77]

Table 1. Ionic conductivities (σ_{ion}) and activation energies of ionic transport (E_a) of Li SEI compounds.

Compound	$\boldsymbol{\sigma_{ion}}$ **/ S cm^{-1} (at room temperature)**	$\boldsymbol{E_a}$ **/ eV**	**Reference**	**Notes**
LiF	~10^{-13}	0.88	[78]	Extrapolated from 250 ˚C, 333 nm-thick-thin film
Li_2S	~10^{-11}	0.90	[22]	
Li_2CO_3	~10^{-13}	1.09	[79]	Extrapolated from 300 ˚C
Li alkyl carbonates (C_1Li-C_8Li)	~10^{-13}	0.72	[80]	Extrapolated from 40 ˚C
LiOH	~10^{-13}	0.90	[81]	Extrapolated from 120 ˚C
Li_2O	~10^{-12}	0.86	[72]	

Table 2. Ionic conductivities (σ_{ion}) and activation energies of ionic transport (E_a) of Na SEI compounds.

Compound	$\boldsymbol{\sigma_{ion}}$ **/ S cm^{-1} (at room temperature)**	$\boldsymbol{E_a}$ **/ eV**	**Reference**	**Notes**
NaF	~10^{-16}	2.38	[82]	Extrapolated from 496 ˚C
Na_2S	~10^{-10}	0.59	[23]	
Na_2CO_3	10^{-13} to 10^{-10}	0.74	[83]	Extrapolated from 315 ˚C
Na alkyl carbonates (C_1Na-C_8Na)	< 10^{-14}	> 1.40	[80]	Extrapolated from 72 ˚C
NaOH	~10^{-15}	1.10	[84]	Extrapolated from 144 ˚C, most likely H^+ conduction

1.2.3. Artificial SEI

SEI formed spontaneously by the contact between Li or Na with electrolytes can be problematic for the battery application since it does not completely passivate the alkali metals and the layer is chemo-mechanically inhomogeneous. The incomplete passivation leads to the continuous chemical reaction between alkali metals and electrolytes, resulting in low coulombic efficiency of the battery cells. [12] Inhomogeneity of the layer causes non-uniform Li^+ (or Na^+) flux and finally dendrite formation. [13] In order to produce chemo-mechanically uniform and stable SEI, many efforts such as using fluorine-rich electrolytes [85], utilizing high salt concentration electrolytes [86, 87], and application of self-healing electrostatic shield mechanism with Cs^+ or Rb^+ [88, 89] have been introduced. Another promising and widely studied strategy is to form SEI *ex situ* prior to the electrochemical cell assembly, namely, artificial SEI. [7, 21, 90-95] Artificial SEIs cover a wide range of materials, including inorganic compounds (e.g. hollow carbon nanospheres [96], Li_3PO_4 [97] and Al_2O_3 [98]), organic films (e.g. polydimethylsiloxane [99]) and composite materials [100-102]. Although many materials have been developed so far, very little fundamental understanding is given about the detailed chemical properties, stabilities against Li/Na, transport mechanism, and the SEI growth behavior of such artificial SEIs. These fundamental studies must be performed in parallel with the development of the materials for the artificial SEIs.

2. Experimental methods

2.1. Sample preparation

2.1.1. Li/Na metal electrode and liquid electrolyte preparation

Due to the high reactivity of metallic Li and Na, surface degradation is expected even in the Ar-filled-glovebox. Thus, the alkali metals (Li rod with 99.9% trace metals basis, Na cubes contains mineral oil with 99.9% trace metals basis, both purchased from Sigma Aldrich) were cut freshly in the Ar-filled-glovebox (atmosphere: O_2 <0.1 ppm, H_2O <0.1 ppm) each time, right before the electrodes were prepared. Li and Na were subsequently sandwiched between two Celgard separators, roll-pressed to approximately the same thickness (0.15 mm), and then cut into discs with a diameter of 10 mm. Triethylene glycol dimethyl ether (triglyme, 99%) and molecular sieves (pore size of 3Å, 1-2 mm) were purchased from Alfa Aesar. Ethylene carbonate (EC, 98%) and dimethyl carbonate (DMC, 98%) were purchased from Sigma-Aldrich. In order to remove the residual moisture, molecular sieves were firstly activated by heating to 180 ˚C under vacuum overnight, and then added to the solvents. LiTf ($LiCF_3SO_3$, 98%, Sigma-Aldrich) and NaTf ($NaCF_3SO_3$, 99.5%, Solvionic) salts were dried prior to use (at 120 ˚C under vacuum, overnight). The moisture in the electrolytes was controlled to be under 20 ppm, as confirmed by Karl-Fischer titration performed in an Ar-filled-glovebox

2.1.2. Synthesis of sulfide-based solid electrolytes and artificial SEIs

β-Li_3PS_4 was synthesized via a solvent-mediated synthesis as reported in the literature. [103-108] Li_2S (99.9%, Sigma Aldrich) and P_2S_5 (98+%, Acros Organics) were mixed in a 3:1 molar ratio and poured to tetrahydrofuran (Fischer Scientific, anhydrous, synthesis grade) with a volume ratio of 1:20. The mixture was stirred for 24 hours at room temperature under Ar atmosphere. Subsequently, the mixture was centrifuged at 9000 rpm for 10 minutes, and dried under vacuum at 140 ˚C for 24 hours. Na_3PS_4 was synthesized via a mechanical ball-milling. [109, 110] Na_2S (nonhydrate, extra pure, Fischer Scientific) and P_2S_5 (anhydrous, synthesis grade, Fischer Scientific) were mixed in a 3:1 molar ratio and put in a ZrO_2 jar with 5 ZrO_2 balls. The ball-to-sample weight ratio was 7:1. The powder mixture was milled using a planetary mill apparatus (Fritsch, planetary mill apparatus pulverisette 5) at 250 rpm for 48 hours. The samples were neither heat-treated nor exposed to air during the synthesis and handling procedure.

For synthesizing sulfide-based artificial SEI, the prepared Li/Na electrodes in section 2.1.1. were placed in the homemade glass ampoules with a length of 600 mm, together with the sulfur powder. The glass ampoule was placed in an oven and heated at different temperatures (in the temperature range from 298 to 433 K). All processes were performed in a glovebox (both O_2 and H_2O level below 0.1 ppm). A schematic diagram of the Li_xS_y (Na_xS_y) synthesis is shown in Figure 1. The temperature of the alkali metal ($T_{Li(or\ Na)}$) and the temperature of S (T_s) are were controlled in a separate way for distinguishing the temperature effect on the reaction kinetics and the concentration of the S vapor. $T_{Li(or\ Na)}$ was always higher than T_s to avoid the S condensation on the alkali metals.

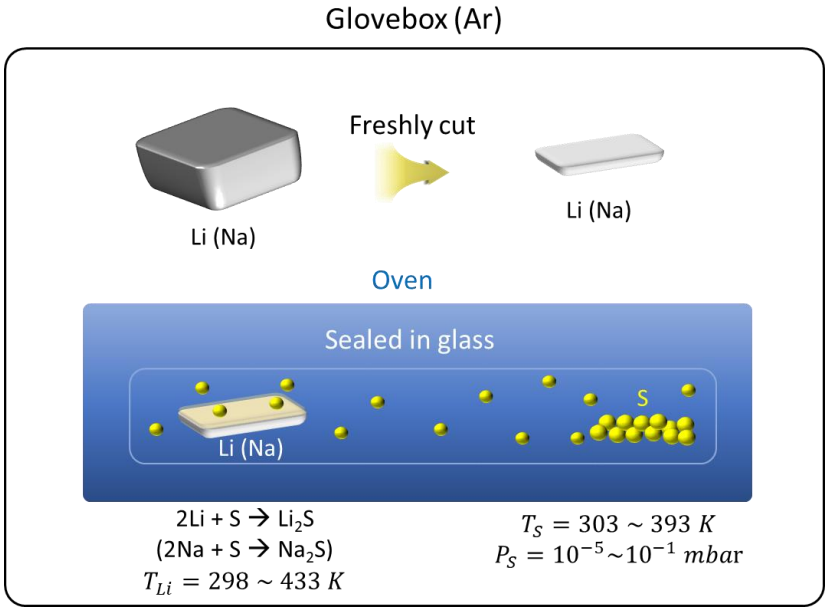

Figure 1. Schematic diagram of the synthetic method for sulfide-based artificial SEIs (Li_xS_y and Na_xS_y). T_s: temperature of sulfur, P_s: vapor pressure of sulfur, T_{Li}: temperature of Li.

Al_2O_3 was synthesized by atomic layer deposition (ALD) method. ALD is a thin-film deposition technique which exposes the substrate surface to the gaseous species and induces subsequent chemical reaction under vacuum. The Li/Na metal electrodes on stainless steel as made in section 2.1.1. were transferred to the Ar-filled glovebox connected to the Sentech PEALD instrument with Real Time Monitor. The precursors used for ALD process were trimethlyaluminium (TMA, from Sigma-Aldrich) and water. The reactor temperature was 100 ˚C for Li and 90 ˚C for Na. The synthesis proceeds in four steps: TMA pulse for 150 ms, N_2 purge for 2 s (120 sccm), H_2O pulse for 150 ms, and N_2 purge for 2 s (120 sccm). The thickness of the deposited layer was measured by Real Time Monitor (ellipsometer) on a blank Si wafer piece which was placed in the vicinity of the sample during the ALD process. The Al_2O_3 growth rate is approximately 0.6 Å s^{-1}. ALD was performed by Marion Hagel from Nanostructuring Lab of Max Planck Institute for Solid State Research.

2.1.3. Li thin film synthesis with molecular beam epitaxy

Molecular beam epitaxy (MBE) is a thin film synthesis method which uses thermal evaporation in an ultrahigh vacuum chamber (pressure $<10^{-10}$ mbar) in order to produce high purity materials. The pressure in the growth chamber was kept being $\sim10^{-11}$ mbar by a combination of a turbo-pump and cryo-pump. During the Li film synthesis, the temperature of the effusion cell where the bulk Li piece is stored was increased to 560 ˚C with an increasing rate of 10 ˚C min^{-1}. The synthesis was performed for 2 hours during which the substrate temperature was kept at room temperature. The substrate used for the synthesis is single-crystal MgO purchased from Cryotec.

2.2. Characterization

2.2.1. Chemical and morphological characterization

Scanning electron microscopy (SEM) is a tool for observing the morphology of the materials in a few hundreds of nm to μm scale, and it is often combined with focused-ion beam (FIB) to prepare the cross-section cutting of the sample. For FIB-SEM analyses, electrochemical coin cells were disassembled and electrodes were collected. Li/Na electrodes from the cells containing 1M LiTf (NaTf) in triglyme and 1M LiTf (NaTf) in EC/DMC=50/50 (v/v) were washed with triglyme and EC/DMC=50/50 (v/v), respectively to avoid salt precipitation in the SEI. Subsequently, they were dried overnight under vacuum at room temperature and transferred from Ar-filled-glovebox to the FIB-SEM measurement chamber with self-made airtight transfer tools. Cross-section images of SEI on Li and Na metal electrodes were measured by Zeiss Crossbeam SEM with FIB. FIB cutting was performed using Ga^+ beam (acceleration voltage: 30 kV) with current ranging from 200 pA to 2 nA, depending on the sample and its reactivity. FIB-SEM is performed by Bernhard

Fenk and Ulrike Waizmann from Nanostructuring Lab of Max Planck Institute for Solid State Research.

XPS is an X-ray based technique used to identify the chemical compounds and the related binding energies by measuring kinetic energies of the ejected electrons from the photoelectric effect. XPS is a surface-sensitive tool (few nm depending on the material) since only the electrons close to the surface can escape without the energy loss. XPS of Li samples was performed on a Kratos Axis Ultra system with a monochromatic Al Kα X-ray source. High-resolution data were acquired with a pass energy of 20 eV. Ar^+ sputtering was performed using a scanning Minibeam III sputter gun (Kratos) with a beam energy of 4 kV and an emission current of 20 mA. XPS data were analysed with the CasaXPS software (version 2.3.23PR1.0 by Casa Software Ltd). For accurate phase identification, the peak shift due to charging was corrected based on the binding energy of Li_2S,[111] and the phase identification was confirmed again with the binding energy separation between O 1s and Li 1s in Li_2O, as discussed in the literature. [112] For fitting the S 2p peaks, the binding energy difference between the spin-orbit split components (S $2p_{3/2}$ and S $2p_{1/2}$) and their area ratio was constrained to 1.2 eV and 2:1, respectively.[113] Samples were transferred to the XPS chamber under Ar atmosphere in an airtight transfer tool. XPS was performed by Kathrin Küster from Interface Analysis group in Max Planck Institute for Solid State Research.

ToF-SIMS is an additional surface-sensitive method which identifies the type of elements by measuring the mass of molecules emitted from the surface by a high-energy (few keV) particle beam. ToF-SIMS measurements were carried out using a ToF-SIMS V instrument (IONTOF), version NCS. Dual beam depth profiles were acquired by a cyclic sputter-probe series. The sputter gun and the analysis gun were operated in a non-interlaced mode with an additional flood gun in order to avoid sample charging. For sputtering, a Cs^+ source was employed with 2 keV ion energy

and 132 nA current on a 500 × 500 μm^2 crater area. For probing, monoatomic Bi_1^+ ions were used, accelerated by 30 keV, with a current of 1.7 pA on a 100 × 100 μm^2 analysis area. Negatively-charged ions ejected from the sample were collected and measured. Data analysis was carried out using the software Surfacelab 7.1. The ion intensities were normalized to the total ion count for each sputter time data point. Samples were transferred under Ar atmosphere to the chamber using a commercial (ION-TOF) airtight transfer vessel. ToF-SIMS was performed by Tolga Acartürk from Interface Analysis group of Max Planck Institute for Solid State Research.

X-ray diffraction (XRD) is typically used for determining the crystal structure of the materials. XRD was measured using an X-ray diffractometer from PANalytical GmbH (Empyrean Series 2) with a Cu K$\boldsymbol{\alpha}$ radiation energy of 40 kV and a current of 40 mA. The samples were mounted in a domed airtight sample holder from Anton Paar. For phase determination, the HighScore Plus software, Version 3.0e, was used. XRD was performed by Helga Hoier from Department of Physical Chemistry of Solids in Max Planck Institute for Solid State Research.

Inductively coupled plasma optical emission spectroscopy (ICP-OES) was done with Spectro Ciros device. Liquid samples were diluted in water in a ratio of 1:1000. ICP-OES was performed by Samir Hammoud from Max Planck Institute for Intelligent Systems.

2.2.2. Cell assembly and electrochemical measurements

Working principles of electrochemical impedance spectroscopy (EIS)

Electrochemical impedance spectroscopy (EIS) is a technique to measure the impedance of a system by applying alternating voltage ($\widetilde{U}$) or alternating current ($\tilde{I}$) in a wide range of frequencies (MHz to mHz). EIS is a powerful technique to understand the electrical transport mechanism of a material, as it allows distinguishing different kinetic processes having different relaxation times.

[114-118] In particular, EIS is an irreplaceable method for SEI investigation as it enables *in situ* decoupling of different electrochemical transport processes in a non-destructive way. [116, 119-121] The impedance (*Z*) can be written as

$$Z(\omega) = \frac{\tilde{U}(\omega)}{\tilde{I}(\omega)} = \left|\frac{\tilde{V}(\omega)}{\tilde{I}(\omega)}\right| \left(cos\ \phi(\omega) + j\ sin\ \phi(\omega)\right) = Z_{Re} - jZ_{Im} \tag{2.1}$$

where $\tilde{U}(\omega)$ is the voltage, $\tilde{I}(\omega)$ is the current, ω is the angular frequency ($\omega = 2\pi f$), ϕ is the phase angle between the input and output signals, and *j* is the imaginary number ($\sqrt{-1}$). As can be seen in equation (2.1), impedance is a frequency-dependent complex number consisting of real part (Z_{Re}, also be represented by *Z'*) and imaginary part (Z_{Im}, or *Z''*). In case of parallel connection of resistance (*R*) and capacitance (*C*), impedance becomes

$$Z = \frac{R}{1 + \omega^2 R^2 C^2} - j\frac{\omega R^2 C}{1 + \omega^2 R^2 C^2} \tag{2.2}$$

which results in the semicircle in Nyquist plot as depicted in Figure 2.

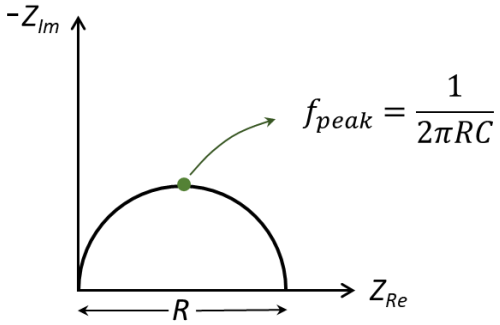

Figure 2. Schematic diagram of Nyquist plot of RC parallel circuit. f_{peak} refers to the frequency in which $|Z_{Im}|$ becomes maximum in the semicircle.

In the real material system, the electrodes are not uniformly active and there is a distribution of time constants, which can be modeled by a constant phase element (CPE). [122] CPE is given by

$$Z_{CPE} = \frac{1}{(j\omega)^{\alpha} Q} \tag{2.3}$$

where α and Q are the magnitude and the exponent of CPE. $\alpha = 1$ indicates completely homogeneous material without distribution of time constant, while $\alpha \neq 1$ accounts for the non-ideal situation where the capacitive response is inhomogeneous. The effective capacitance of a CPE is as follows [123]

$$C = Q^{1/\alpha} R^{1/\alpha - 1}. \quad (2.4)$$

Typical processes occurring in the symmetric Li/Na battery system involves charge transfer at metal/SEI, SEI/liquid, metal/liquid interfaces, ion migration across SEI, and ion diffusion in the liquid (in the pores or in the bulk). In the ideal case, when the disparity of these processes' relaxations times are significant, EIS is capable of splitting the complex processes into elementary constituents. However, in the real measurement, it is very often that the several semicircles corresponding to different processes overlap to each other in the Nyquist plot, which makes the evaluation more challenging. [116]

The cation transference number (t_+ or t_{eff}) can be derived by another method, suggested by Sørensen and Jacobsen, which is a technique assuming that both the cation and anion transport contributes to the bulk resistance (R_{bulk}), and the final impedance from the bulk diffusion at lowest frequency where Z_{Im}=0 (Z_d(0)) is solely dependent on the cation transport. [124] Thereby, the cation transference number is calculated from the following equation.

$$t_+ = \frac{1}{1 + \frac{Z_d(0)}{R_{bulk}}} \quad (2.5)$$

Working principles of galvanostatic polarization

Galvanostatic polarization, often called as direct current (DC) measurement, is an electrochemical technique in which a constant current is applied, while the change of voltage in

time is observed. This technique has been extensively used in solid-state electrochemistry to determine the major charge carrier of the electrical materials, which is represented by transference number (t).

$$t_i = \frac{\sigma_i}{\sum_j \sigma_j} \tag{2.6}$$

where t_i is a transference number of specific charge carrier (i) and σ is conductivity. In case of liquid electrolyte in which the electronic conductivity is negligible, main charge carriers are cations and anions which originate from the salts. When the symmetric Li (or Na) electrodes are adopted in the electrochemical cells, they act as selective blocking electrodes which are reversible for Li^+ (or Na^+) and blocking for anions. Therefore, combining galvanostatic polarization and impedance allows one to derive cation transference number (t_+). When constant current (I) is applied, initially both the cations and anions migrate to the opposite direction, and the anion-blocking electrode stops the anion flux at the steady state (t=∞), meaning that the steady-state voltage solely depends on the cation transport. The initial total resistance ($R_{tot,0}$) can be described as follows.

$$R_{tot,0} = R_{SEI,0} + R = \frac{U_0}{I} \tag{2.7}$$

where $R_{SEI,0}$ represents the initial SEI resistance and R is the resistance contributed by the migration of both cations and anions, U_0 is the initial voltage. As time goes by and the steady state is reached, the final total resistance ($R_{tot,\infty}$) can be written as

$$R_{tot,\infty} = R_{SEI,\infty} + R_+ = \frac{U_\infty}{I} \tag{2.8}$$

where $R_{SEI,\infty}$ is the final SEI resistance, R_+ is the resistance contributed by the migration and diffusion of the cations only and U_∞ is the final voltage at a steady state.

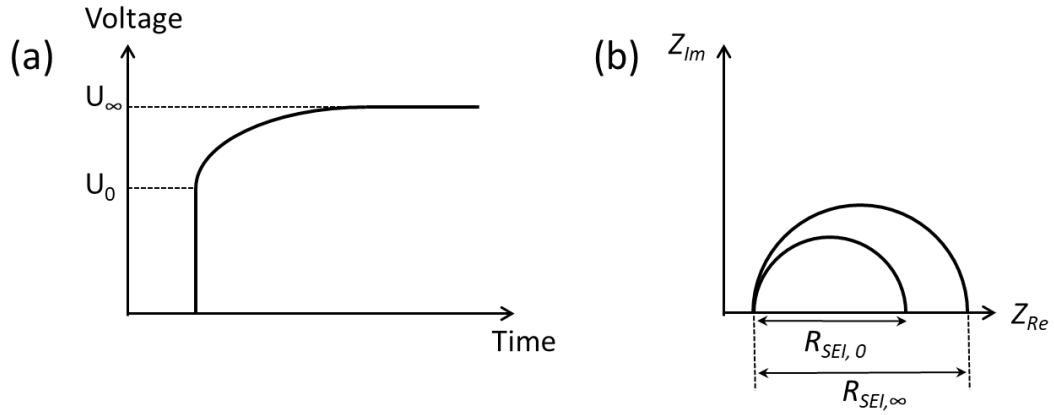

Figure 3. Schematic diagram of (a) time *vs.* voltage profile and (b) Nyquist plot before and after galvanostatic polarization during galvanostatic polarization.

Combining equation (2.7) and (2.8), t_+ is derived as

$$t_+ = \frac{R}{R_+} = \frac{I(R_{tot,0} - R_{SEI,0})}{U_\infty - IR_{SEI,\infty}} \tag{2.9}$$

The time-dependent concentration profile within the liquid electrolyte in the symmetric Li (or Na) cell during the polarization is depicted in Figure 4.

The time-voltage profile of the galvanostatic polarization (Figure 3a) exhibits an exponential behavior for long times ($t > \tau^\delta$) as follows. [24]

$$ln(U(t) - U(\infty)) = C \pm t/\tau^\delta \tag{2.10}$$

where $\tau^\delta = \frac{L^2}{\pi^2 D^\delta}$ (D^δ: chemical diffusion coefficient, L: length of the sample where polarization occurs). Thereby, by fitting the time *vs.* $ln(U(t) - U(\infty))$ curve with a linear function, chemical diffusion coefficient can be obtained from the slope.

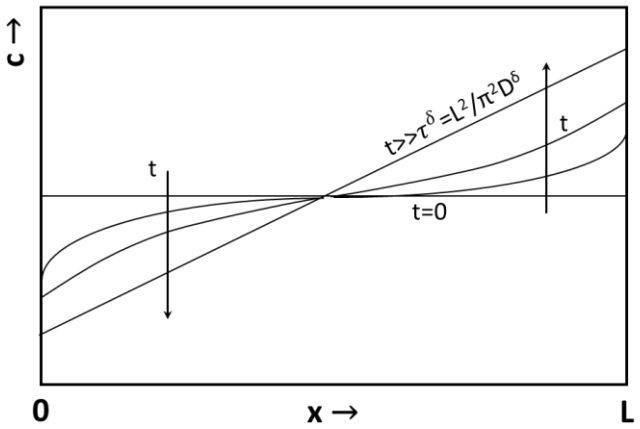

Figure 4. Concentration profile in the liquid electrolyte during polarization experiments for electrochemical cells with two symmetric selective blocking electrodes.[1]

Experimental

CR2032-type coin cells made of stainless steel were assembled with two Li (Na) symmetric electrodes and liquid or solid electrolytes. Liquid electrolytes were prepared by dissolving 1M $LiCF_3SO_3$ (LiTf, 98%, Sigma-Aldrich) and 1M $NaCF_3SO_3$ (NaTf, 99.5%, Solvionic) into triethylene glycol dimethyl ether (triglyme, 99%, Alfa Aesar). The H_2O content in the liquid electrolyte was controlled to be below 1 ppm (using Karl-Fischer titration technique). For the cells with liquid electrolytes, two symmetric electrodes were separated by a 20 μm-thick Celgard separator (H2013) soaked with 20 μL of liquid electrolyte. Here, a spring was included in the cell for achieving better contact between the different components. For the solid-state cells, synthesized solid electrolyte powders (Li_3PS_4 and Na_3PS_4) were pressed uniaxially (380 MPa, 10 mm diameter, between 70 to 80% of pellet density) in the glovebox, and sandwiched between two Li (Na) electrodes in a coin cell. In solid-state cells, a spring was not used due to the limited space.

In order to determine the ionic conductivity of the solid electrolytes, the pellets were produced in the same way but were sputtered with Ru (400 nm thickness) on both flat sides in the glovebox.

EIS was performed in the frequency range from 10^6 to 0.01~1 Hz, depending on the specific cells. The experiments were conducted in the potentiostatic mode, with an amplitude of 10~100 mV, using Solatron 1260 and Novocontrol Alpha-A devices. Temperature-dependent EIS measurements (in the range between 5˚C and 50˚C) were performed using an external thermostat (Lauda RC6CP). In this setup, two thermocouples were employed: one was placed in the vicinity of the coin cell for the precise sample temperature measurement and the other was located inside the water/oil bath for control purposes. Temperature-dependent EIS measurements were carried out for 30 minutes for each temperature (25 minutes to reach the equilibrium and 5 minutes for EIS measurement) to minimize the changes of the SEI changes during the experiment. Analysis of the impedance spectra was performed with ZView software (Scribner Associates, version 3.5c).

Galvanostatic polarization was performed using Keithley current source (model 220). Galvanostatic stripping-plating tests were performed in Li/electrolyte/Li and Li/electrolyte/Cu cells by a Neware Battery Testing system (BTS V.5.3 by Neware Technlogy Limited) with a constant current of 0.1 mA cm^{-2}. Other parameters affecting the stripping-plating behavior such as thickness of the electrode, amount of liquid electrolyte, and thickness of the separator were kept constant in every cell.

3. SEIs on Li/Na formed by the contact with liquid electrolytes

3.1. Native films on Li and Na

Due to the high reactivity of Li and Na, alkali metals are already partially covered with native films consisting of carbonates, hydroxides and oxides (e.g. Li_2CO_3, LiOH and Li_2O), even in the glovebox or high-vacuum chamber. [125, 126] The composition of the native films depends on the alkali metal storage condition (e.g. purity of Ar in the glovebox atmosphere) and aging time. First, the surface of the pure commercial Li (Sigma Aldrich, 99.9%) used in this study was examined by XPS and FIB-SEM. Li was cut freshly in the Ar-filled glovebox as the surface was assumed to be covered by chemical compounds formed during the storage. Figure 5 shows XPS results of commercial bulk Li. The Li is oxidized on the surface, with presence of the composition of Li_2CO_3 and carbon-based materials. As sputtering proceeds, Li_2O and LiF are found to be distributed throughout the samples. This is consistent with our previous measurements. [127] The cross-section image of the pure bulk Li measured by FIB-SEM in Figure 6 shows approximately a 200 nm-thick film on the surface. For comparison, a Li thin film (thickness of ~5 μm) synthesized by molecular beam epitaxy (MBE) is also examined. The MBE-grown-Li was synthesized under highly airtight conditions (pressure~10^{-11} mbar). The MBE-grown-Li sample exhibits a similar behavior to commercial Li in terms of XPS results (Figure 7), and the thickness of the native passivation film is approximately 250 nm (Figure 7).

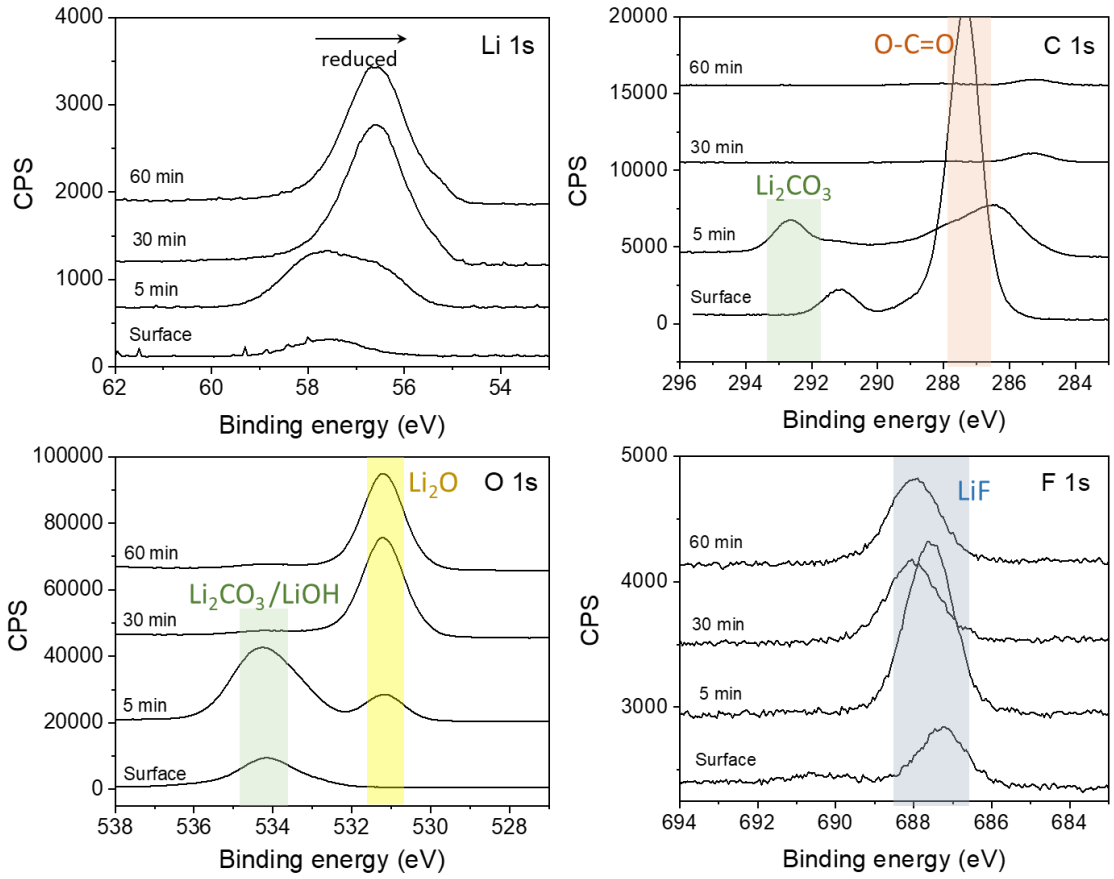

Figure 5. XPS results of commercial bulk Li freshly cut in the glovebox.

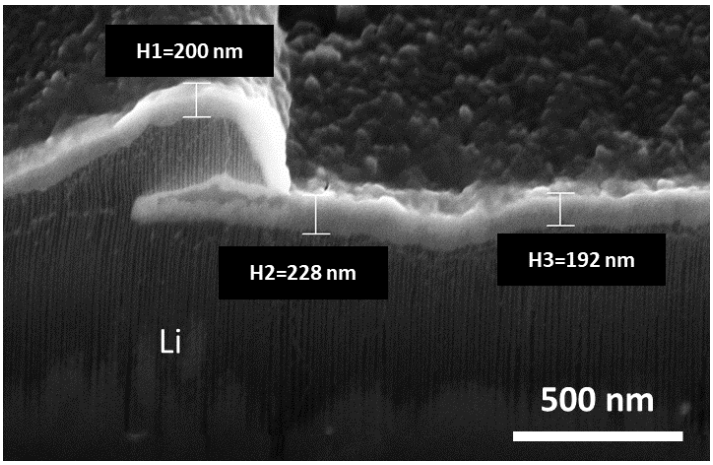

Figure 6. Cross section image of the native film on commercial bulk Li measured by FIB-SEM.

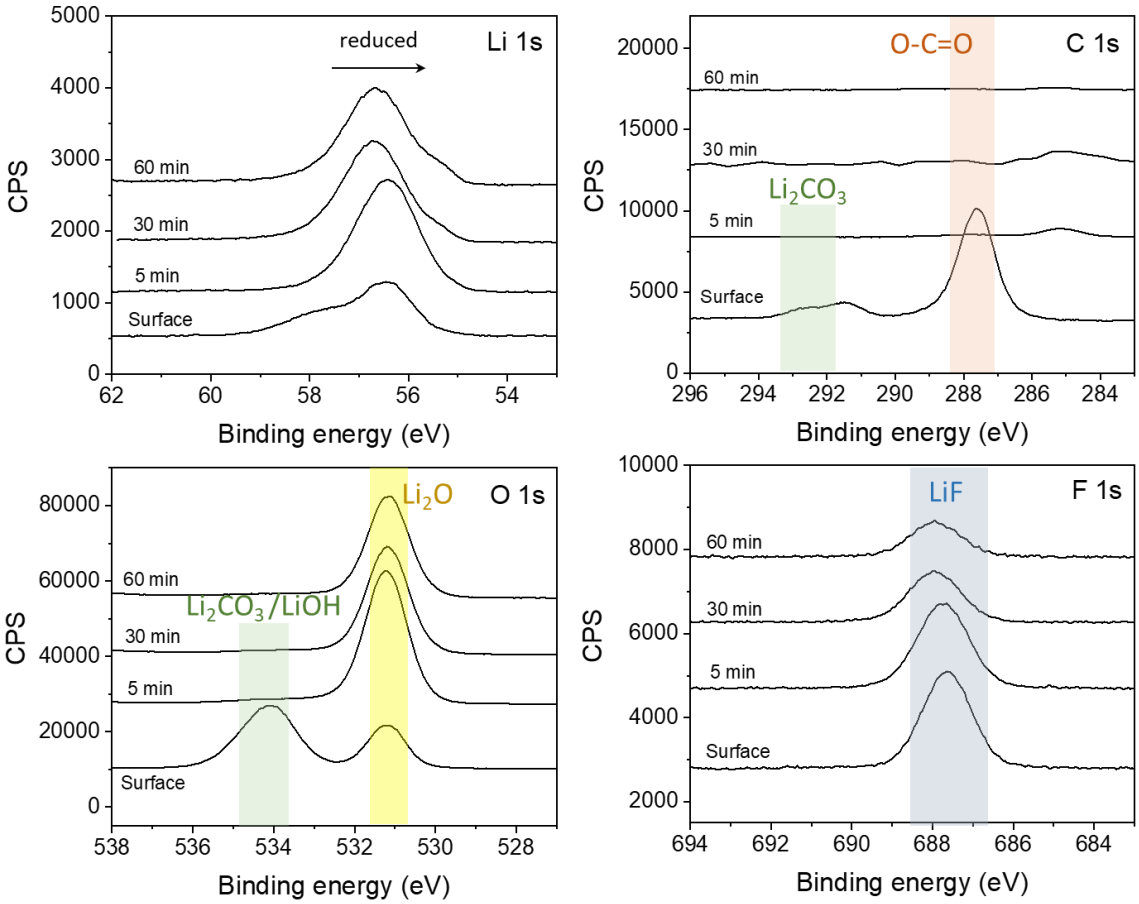

Figure 7. XPS results of MBE-grown Li film.

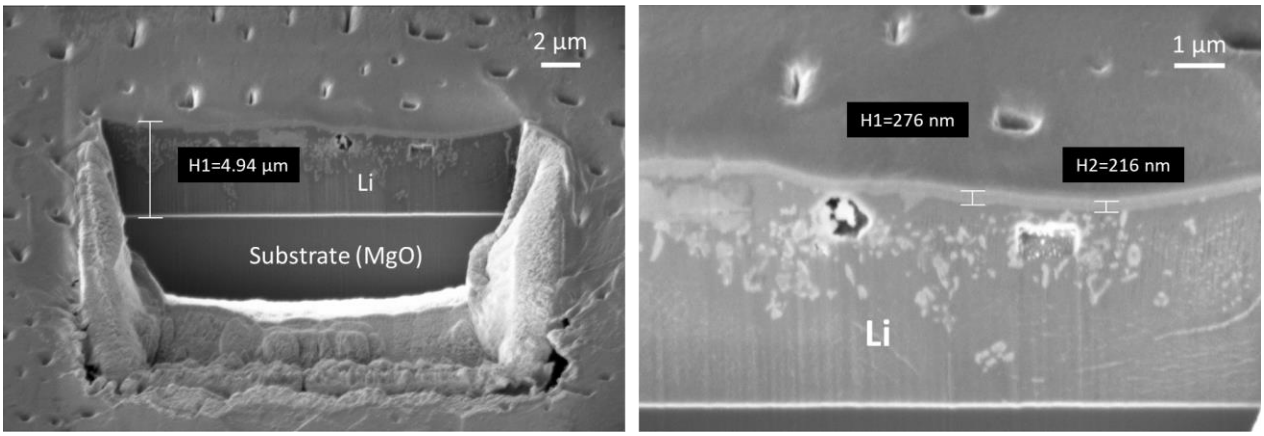

Figure 8. Cross section image of the MBE-grown-Li. Li was deposited on MgO single crystal substrate.

The fact that native films on commercial bulk Li and MBE-grown-Li share similarity in terms of chemical composition and thickness suggests that the native films including impurities stemmed from the storing environment (e.g. glovebox, transfer tools and XPS vacuum chamber).

Native films on Na were examined only by FIB-SEM, as XPS on Na was not performable because of potential Na evaporation in the XPS chamber in view of its relatively high vapor pressure of ~10^{-8} mbar at room temperature [128]. In addition, measurements of the native films on pure Na were very challenging due to the high reactivity of Na. Storage of Na under Ar (purity of >99.98%) appears to impact the native film formation as the Na surface becomes whitish and less smooth after only few hours of exposure in the glovebox. During the transfer from the glovebox to the FIB-SEM chamber, a color change (from silver-shining to white) was also observed. In the cross-section SEM images of the pure Na (Figure 9), a porous film with a thickness of 100~300 nm was identified. It is assumed that the films are composed of NaOH, whose presence was confirmed by XRD (Figure 10).

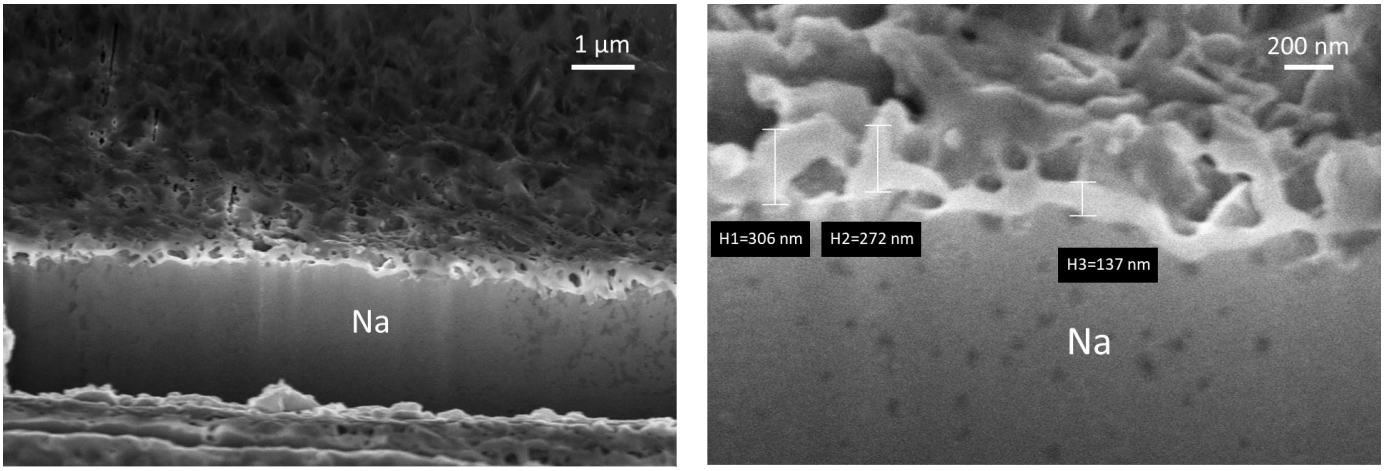

Figure 9. Cross-section images of the films on Na.

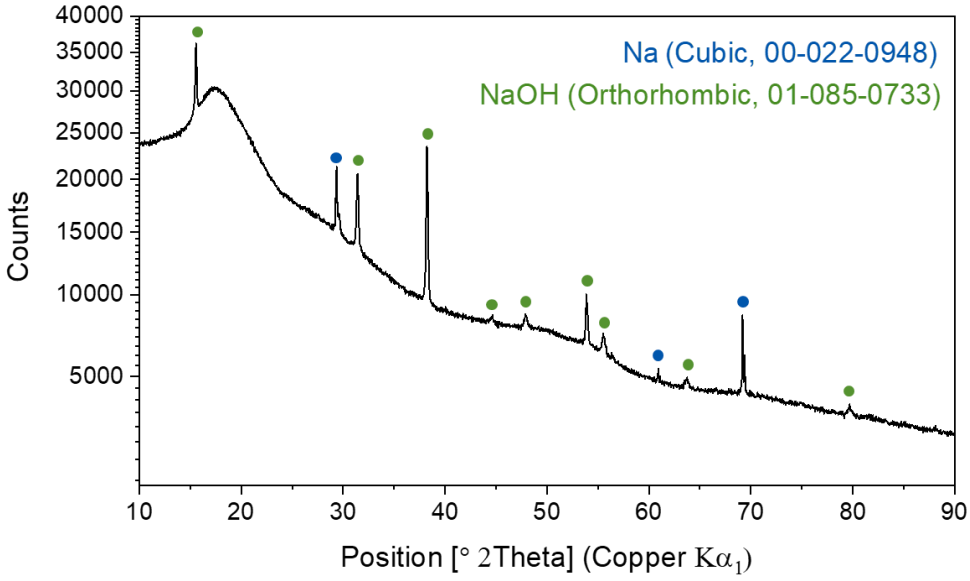

Figure 10. XRD pattern of bare Na after FIB-SEM measurements.

3.2. Ion transport in SEI

The results of this section are published in [77].

3.2.1. Impedance results of symmetric Li/Na cells with salt-free triglyme solvent

Liquid electrolytes consist of salts and solvents, where salts become dissociated and solvated by the solvents. When Li/Na contacts the liquid electrolyte, both the salts and solvents react with the alkali metals, forming SEIs. In order to rule out the influence of salts on the SEI formation and ion transport behavior, contacts of Li/Na with pure triglyme solvent were first studied. Typical impedance spectra (Figure 11) of symmetric Li/Na cells with pure triglyme solvent include three distinct semicircles appearing at different frequency ranges. The first semicircle at highest frequencies (hundreds of kHz) corresponds to the ion transport in the bulk electrolyte (R_{bulk}), considering the fact that the capacitance is in the order of 10^{-10} F cm^{-2}. The second semicircle at medium frequencies (tens of Hz) most likely represents the ion transport through the interfacial region ($R_{interface}$ or R_{SEI}) as the capacitance is in the range of 10^{-6} F cm^{-2}. [129] The final one appearing at the lowest frequencies (lower than 1 Hz) is the concentration polarization (finite-length diffusion) in the bulk of the liquid electrolyte, based on the peak frequencies (the frequency where $|Z_{Im}|$ becomes maximum, $f_{peak} \sim \frac{D}{L^2}$ [130]) and also its Warburg-type behavior. Figure 12 shows how their impedance spectra change over storage under open-circuit potential. For both Li and Na cases, the decrease of R_{bulk} over time was observed which may be attributable to the i) dissolution of the Li and Na (or Li/Na compounds) from the electrodes as the increase of Li/Na concentration was measured by ICP-OES (Table 3), and ii) decrease of the distance of the two

electrodes over time (possibly owing to the pressure on the spring within the cell) which is confirmed by the decrease of R_{bulk} in a symmetric stainless steel cell (Figure 13).

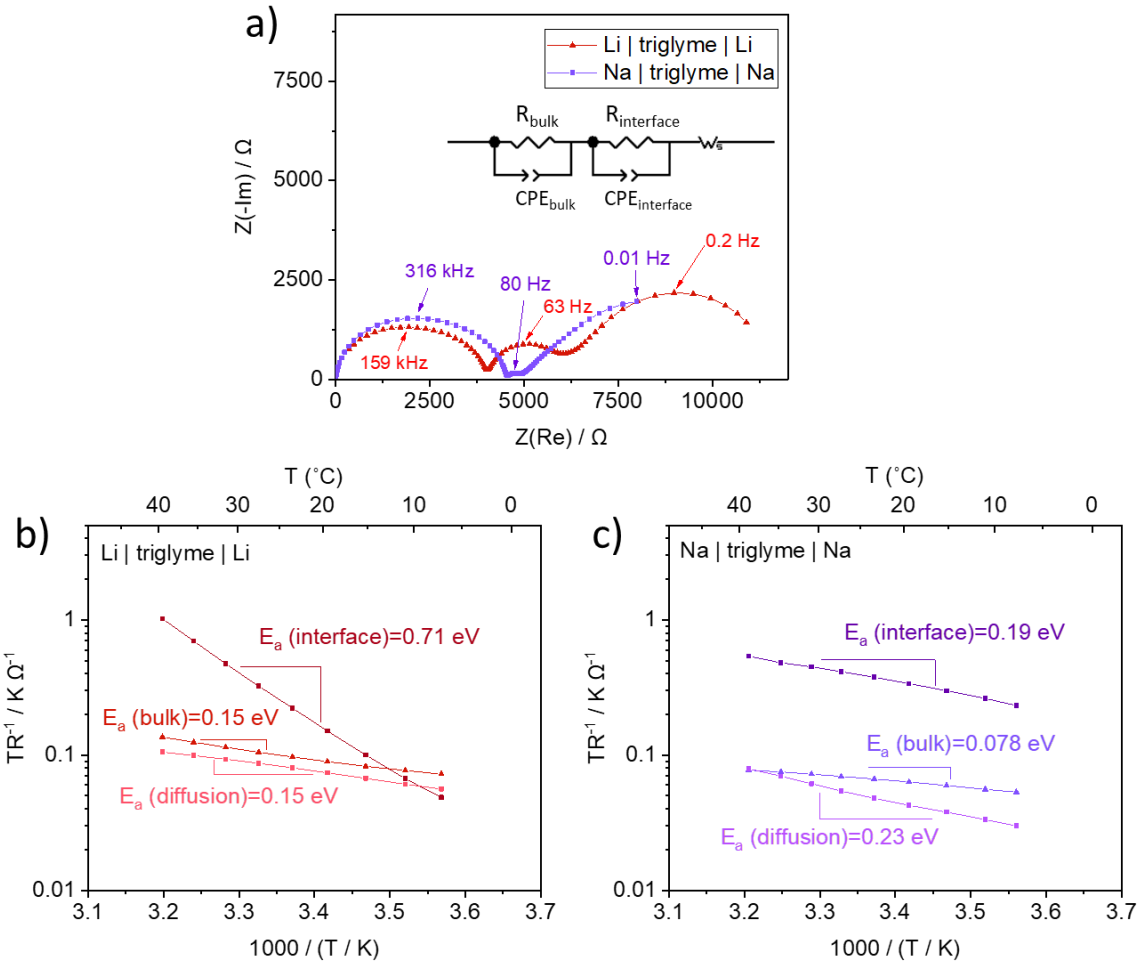

Figure 11. Impedance analyses of symmetric Li/Na cells containing salt-free triglyme solvents stored for 150 hours. (a) Nyquist plots with characteristic frequencies and the inset shows equivalent circuit which corresponds to the observed impedance results. R_{bulk} and CPE_{bulk} are the resistance and the capacitance from the bulk liquid electrolyte (pure triglyme), $R_{interface}$ and $CPE_{interface}$ are from the interface (possibly SEI) and Ws is a finite-length Warburg response.

The clear distinction of the three different contributions (ion conduction in the bulk electrolyte, interfacial transport, and diffusion in the bulk electrolyte) allows the determination of the activation energy (E_a) of each contribution by varying the temperature of the electrochemical cells. Figure 11b and c show the E_a values of the three different processes. In the Li case, the E_a values

for bulk ion conduction and diffusion are identical (0.15 eV) while the one related to the interfacial transport is much higher (0.71 eV). In the Na case the E_a of interfacial process is much smaller (0.19 eV) in comparison to the one of Li interface (0.71 eV), and this value is in-between the values for the bulk (0.078 eV) and ion diffusion (0.23 eV) in the liquid electrolyte. This implies that the interfacial transport behavior at Na-glyme interface is similar to the one in the liquid rather than solid, considering the fact that the E_a values of ion conduction in inorganic/organic SEI compounds are higher than ~0.6 eV (see Table 1 and Table 2). The same impedance measurements were performed with salt-free carbonate-based solvent (mixture of ethylene carbonate (EC) and dimethyl carbonate (DMC) with a volume ratio of 50:50), but a clear distinction of the three different processes (bulk ion conduction in liquid electrolyte, interfacial transport and diffusion in liquid electrolyte) was not performable owing to the high resistance in the order of MΩ (Figure 14).

Table 3. Concentration of Li and Na measured by ICP-OES. Pure triglyme was contacted with Li/Na metal for 150 hours. (Unit: mmol L^{-1})

Sample	Li	Na
1) Pure triglyme	--	6.09×10^{-4}
2) Pure triglyme contacted to Li metal	14.9	3.48×10^{-4}
3) Pure triglyme contacted to Na metal	2.88×10^{-4}	16.8

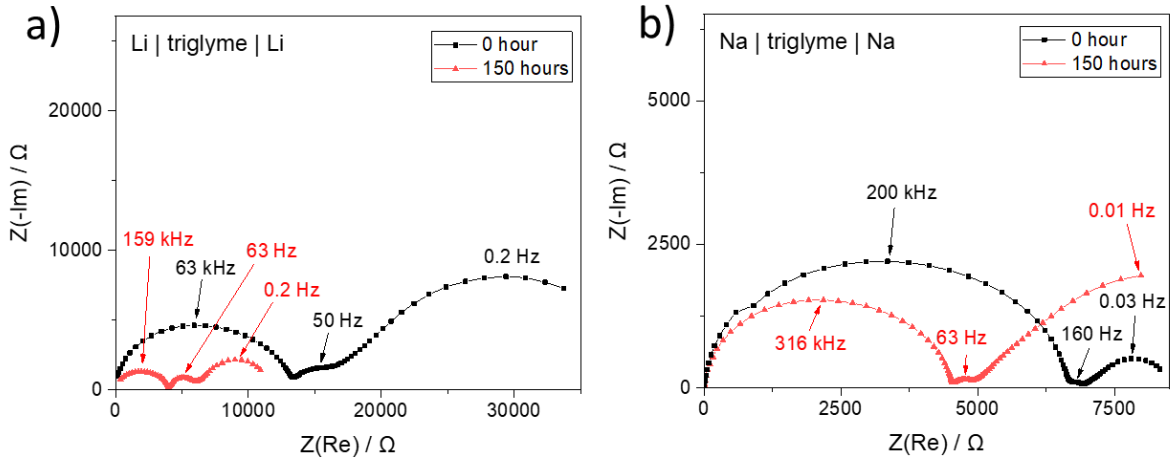

Figure 12. Nyquist plots of (a) Li and (b) Na symmetric cells in contact with pure triglyme solvent and their evolution over time.

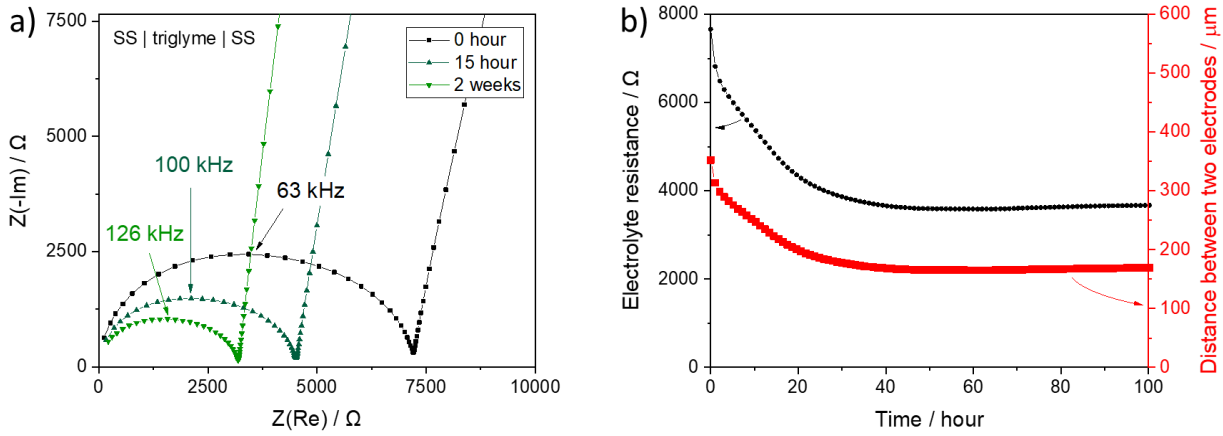

Figure 13. (a) Nyquist plots of stainless steel | triglyme | stainless steel symmetric cell. (b) Resistance and corresponding distance between two electrodes over time. The distance between two electrodes was calculated from $L = \sigma RA$ (L: distance, σ: ionic conductivity of triglyme, R: resistance measured in (a), A: surface area of the electrode)

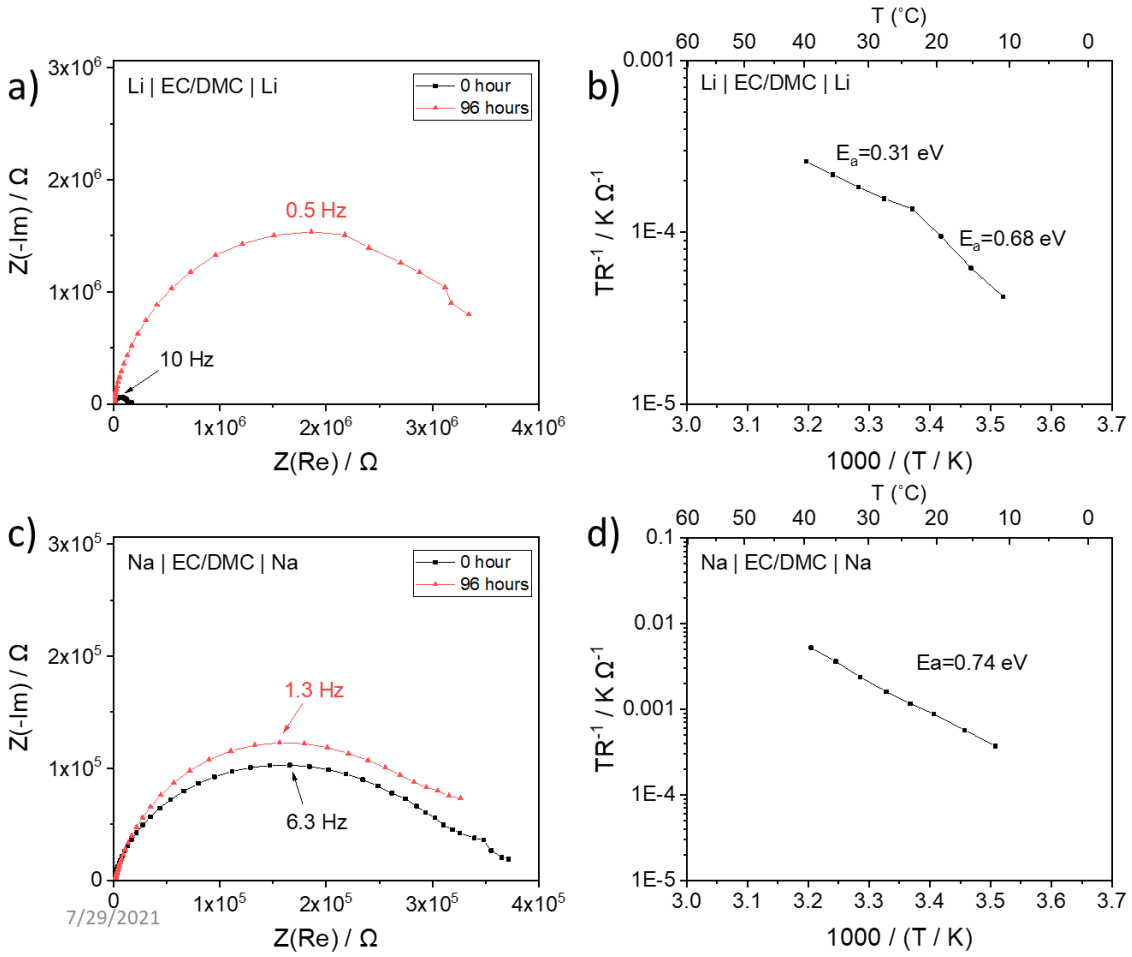

Figure 14. EIS investigation of Li/Na symmetric cells containing salt-free carbonate solvent which is EC/DMC=50/50 (v/v). (a, c) Nyquist plots with characteristic frequencies in Li and Na, respectively and (b, d) Arrhenius plots and E_a of Li and Na symmetric cells, respectively.

3.2.2. Impedance results of symmetric Li/Na cells with glyme- and carbonate-based liquid electrolytes

The next step is to observe the interfacial ion transport behavior with EIS of the electrochemical cells using solvents to which the salts (LiTf and NaTf) have been added. For all impedance spectra, the main semicircles appearing at tens of kHz to hundreds of Hz correspond to the interfacial process based on their capacitance values (10^{-7} to 10^{-6} F), which as of now is called SEI resistance (R_{SEI}). Figure 15 shows the evolution of E_a(SEI) of Li/Na symmetric cells containing glyme-based electrolytes over storage under open-circuit potential after 2 hours and 600 hours. For Li case in Figure 15a, E_a(SEI) is initially 0.52 eV and increases to 0.77 eV after 600 hours. Considering that the E_a values of ion transport in the bulk solid inorganic/organic SEI compounds (Table 1 and Table 2) are higher than 0.6 eV and the ones of bulk liquid electrolytes are 0.15~0.16 eV (Figure 16), the increase of E_a(SEI) implies increased solid portion in the SEI, which in other words can be expressed as SEI densification. In the case of Na in Figure 15c, E_a(SEI) starts with a value of 0.15 eV and finally reaches 0.62 eV, indicating densification of SEI over storage time. The noticeable fact about the Na case is that the initial E_a(SEI) value is identical to the one of ion conduction in bulk liquid electrolyte (Figure 16, marked as light green color). This strongly suggests that the major ion transport pathway in the Na SEI is via liquid electrolyte pathways embedded in the bulk solid SEI part, implying that the Na SEI is initially more porous compared to the Li SEI.

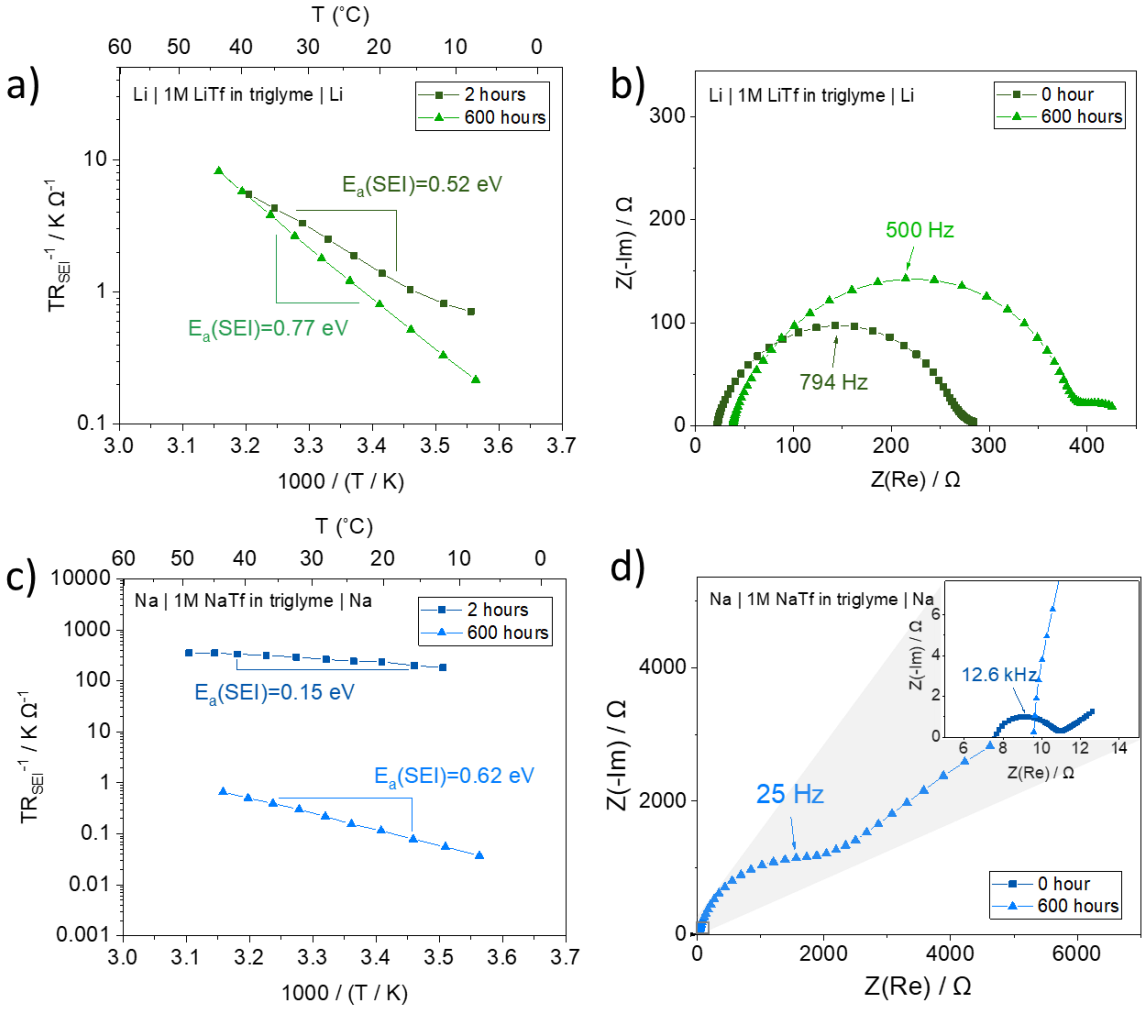

Figure 15. Impedance analyses of symmetric Li/Na cells containing glyme-based electrolytes. (a, c) Arrhenius plot with respect to the SEI resistance where E_a of ion transport in SEI was derived from. E_a was measured after 2 hours and 600 hours of storage under open-circuit. (b, d) Impedance spectra corresponding to (a, c) measured at room temperature.

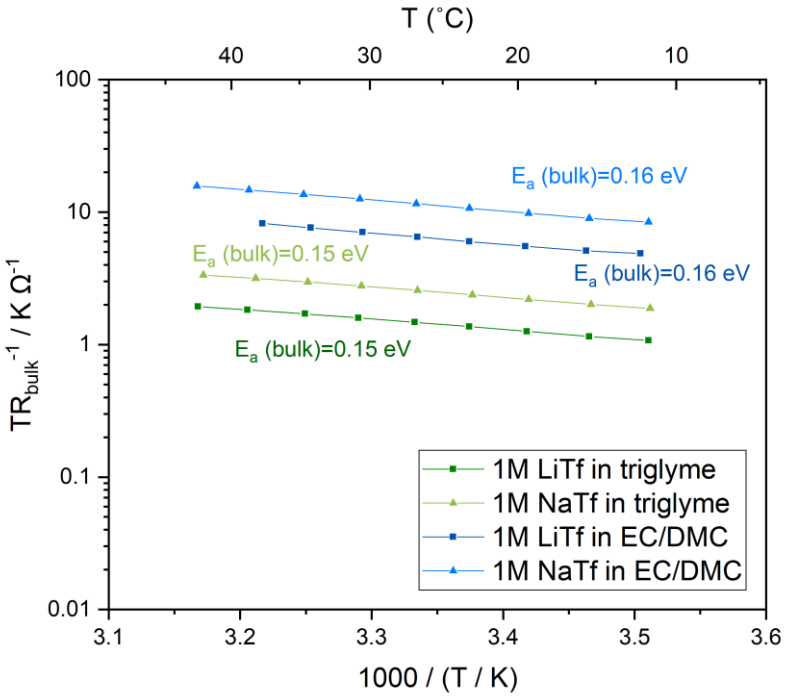

Figure 16. Temperature dependence of bulk electrolyte resistances and activation energies in Li/Na glyme- and carbonate-based electrolytes.

The same measurements were performed with carbonate-based liquid electrolytes (1M LiTf in EC/DMC and 1M NaTf in EC/DMC, Figure 17). SEI on Li formed by the contact with carbonate-based liquid electrolyte exhibits a similar ion transport behavior compared to the one formed by glyme-based electrolyte in terms of E_a(SEI) values and their changes over time. E_a(SEI) values are initially 0.55 eV and finally reach 0.80 eV, indicating densification of the SEI over time. In the Na case, the E_a(SEI) values also show increasing behavior over time (0.30 eV to 0.59 eV), but the values are lower compared to the one of Li. To summarize the results from the impedance experiments, the E_a(SEI) increases over time in all cases of Li/Na with glyme- and carbonate-based electrolytes, most likely owing to the fact that the porous SEIs at the initial storage allow for the liquid electrolyte infiltration in the SEIs. This results in a chemical reaction between the liquid electrolyte and alkali metal, subsequently forming denser SEI. Additionally, SEIs on Na are

suspected to be more porous compared to the one on Li, as their E_a(SEI) values are lower not only at the initial storage but also after 600 hours. The porosity of the Na SEI will be further discussed in the following chapters.

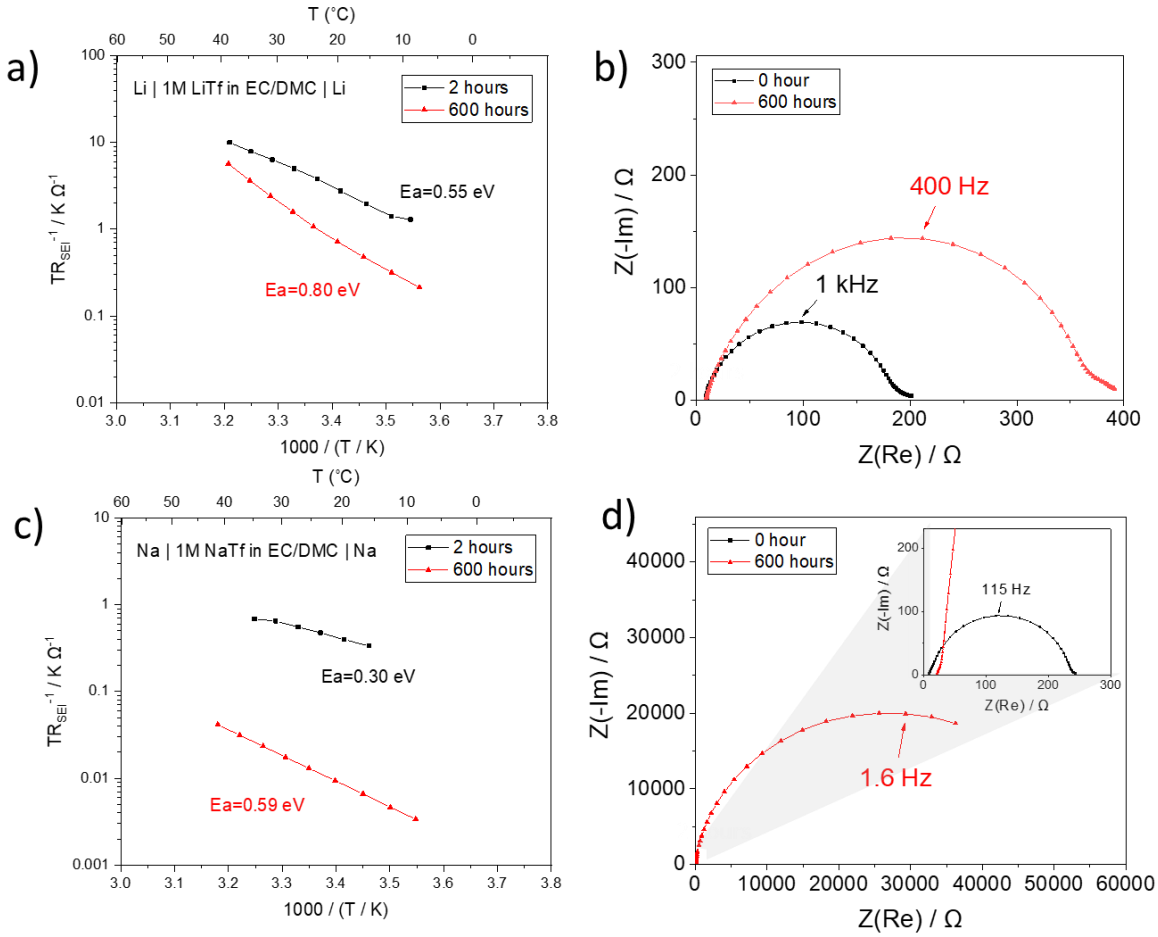

Figure 17. Impedance analyses of symmetric Li/Na cells containing carbonate-based electrolytes. (a, c) Arrhenius plot with respect to the SEI resistance where E_a of ion transport in SEI was derived from. E_a was measured after 2 hours and 600 hours of storage under open-circuit. (b, d) Impedance spectra corresponding to (a, c) measured at room temperature.

3.2.3. Morphology of SEI on Li/Na: FIB-SEM results

The porosity of the SEIs on Na is confirmed by the morphology observation with FIB-SEM. Figure 18 and Figure 19 show the cross-section images of the SEIs on Li/Na after contacting with glyme- and carbonate-based electrolytes for 2 hours and 600 hours under open-circuit potential, respectively, which are the same samples shown in the Figure 15 and Figure 17. Note that the cutting process with focused-ion beam was challenging due to the high reactivity and low melting points of Li and Na (180.5 ˚C and 97.8 ˚C for Li and Na, respectively). The Ga^+ ion beam power was optimized for each sample in order to obtain the best possible cut.

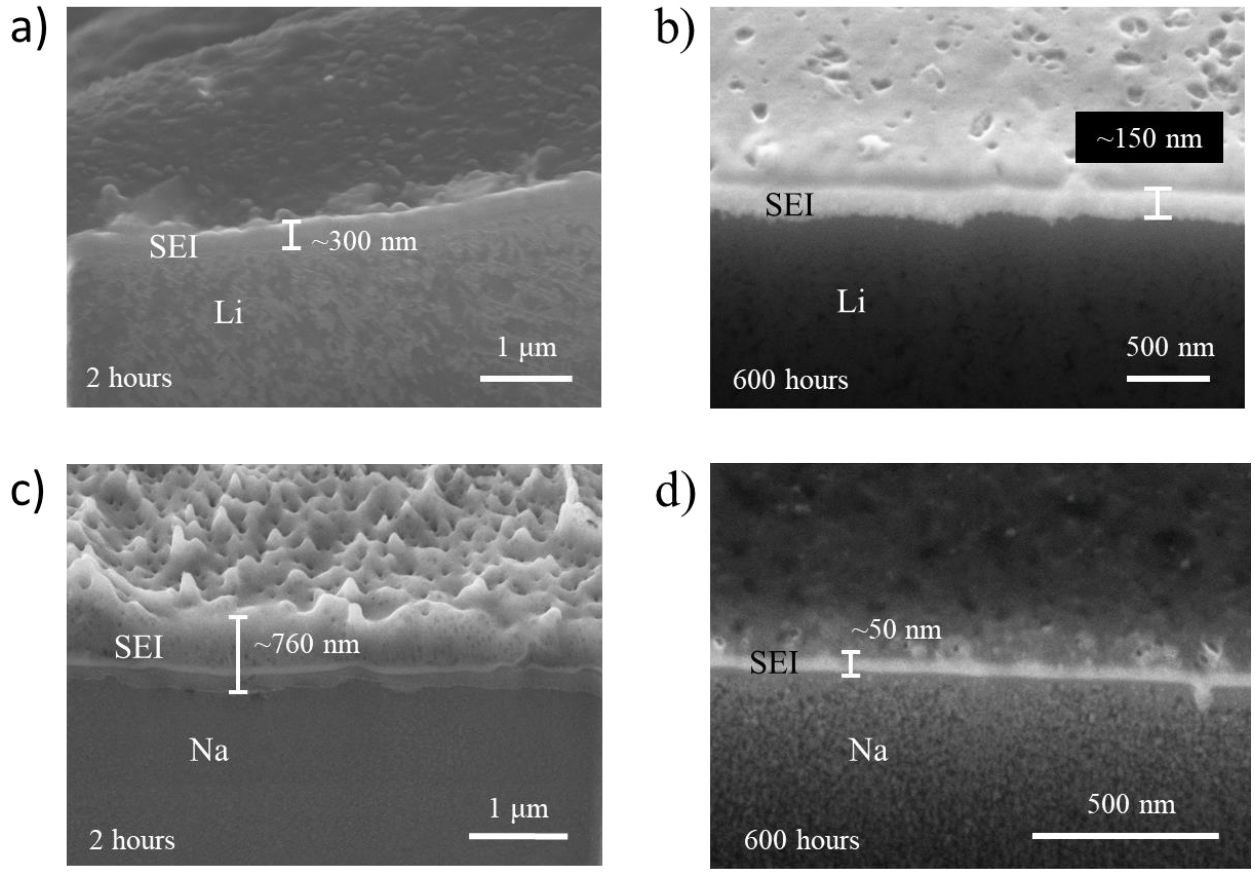

Figure 18. FIB-SEM Cross-section images of SEIs on (a, b) Li and (c, d) Na after contacting with glyme-based liquid electrolytes (1M LiTf/NaTf in triglyme) for (a, c) 2 hours and (b, d) 600 hours under open-circuit potential.

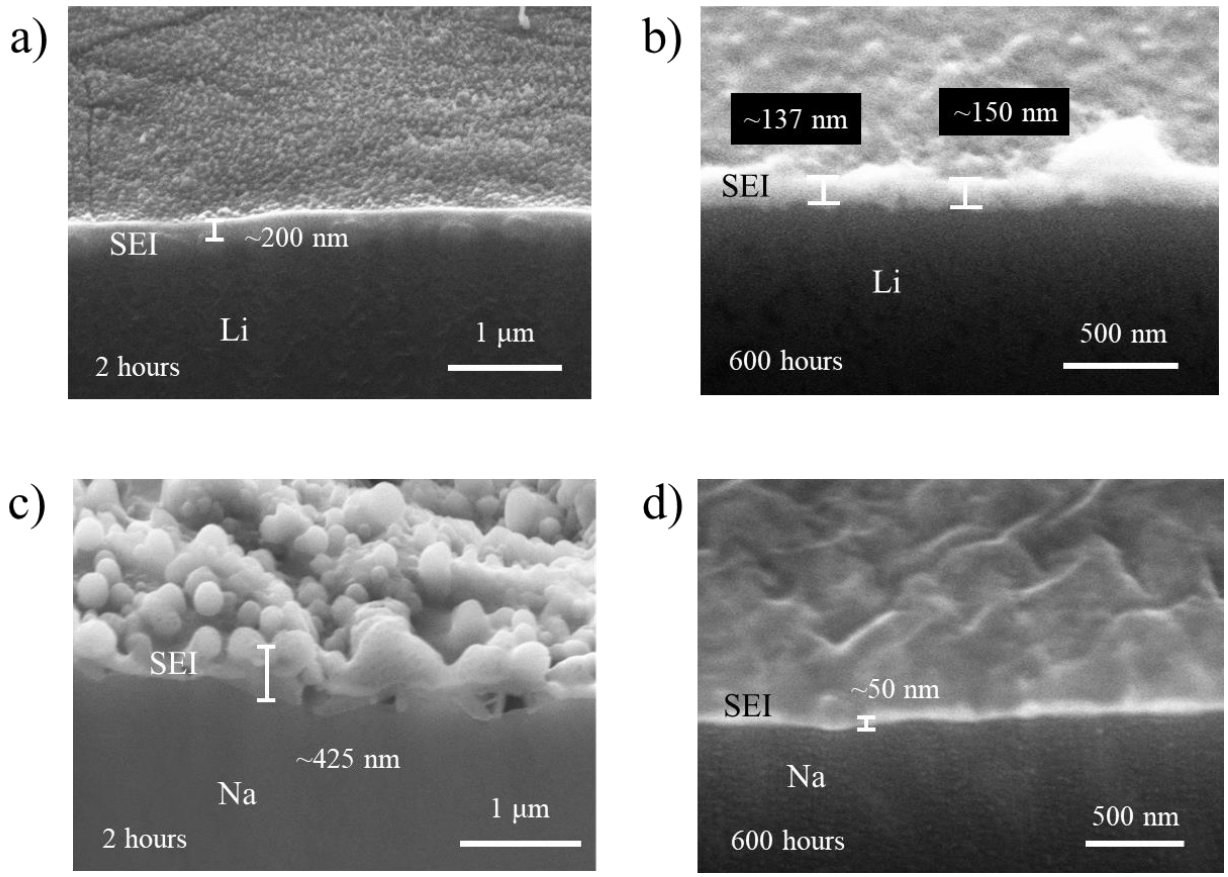

Figure 19. FIB-SEM Cross-section images of SEIs on (a, b) Li and (c, d) Na after contacting with carbonate-based liquid electrolytes (1M LiTf/NaTf in EC/DMC) for (a, c) 2 hours and (b, d) 600 hours under open-circuit potential.

SEI thicknesses are observed to be in the range of from tens of nm to 1 μm. The most noticeable difference between Li and Na is that the SEIs on Na appear to be more porous compared to the one of Li at the initial storage (Figure 18c and Figure 19c). Also, it is clearly seen that SEIs on Na become denser over time (Figure 18c → d, Figure 19c → d) while for the Li case, the densification cannot be confirmed by the cross-section images. These morphological observations are consistent with the measured low E_a(SEI) of Na which increases over the storing time. Although FIB-SEM has resolution limitation for observing nanopores, the densification can be confirmed again taking into account the SEI conductivities with the observed SEI thicknesses. Assuming that the surface area does not change over storage, as the observed roughness does not

seem to cause great changes in the surface area, the effective ionic conductivity of SEI (σ_{SEI}) can be derived with the following equation.

$$\sigma_{SEI} = \frac{d}{R_{SEI}A} \tag{3.1}$$

where d is the thickness measured by FIB-SEM, R_{SEI} is the SEI resistance measured by EIS, and A is the surface area of the electrodes. The values of d and σ_{SEI} in four different cases (Li/Na symmetric cells with glyme- and carbonate-based electrolytes) are listed in Table 4.

Table 4. Summary of the SEI thicknesses and effective SEI conductivities of four different systems. Li-glyme refers to the symmetric cell of Li|1M LiTf in triglyme|Li and Li-carbonate represents for the symmetric cell with Li|1M LiTf in EC/DMC|Li, and the same applies to Na.

System		**SEI thickness measured by FIB-SEM (d) / nm**	**Effective SEI conductivity (σ_{SEI}) / S cm^{-1}**
Li-glyme	2 hours	~300	3.08×10^{-7}
	600 hours	~150	1.06×10^{-7}
Li-carbonate	2 hours	~200	2.87×10^{-7}
	600 hours	~150	1.04×10^{-7}
Na-glyme	2 hours	~760	5.91×10^{-5}
	600 hours	~50	4.10×10^{-9}
Na-carbonate	2 hours	~425	4.67×10^{-7}
	600 hours	~50	2.41×10^{-10}

In all cases, the decrease of σ_{SEI} in time is observed, which is again a confirmation of the SEI densification. In the Li case, the changes of σ_{SEI} values are not significant, as the values are still in the same order of magnitude. On the contrary, the Na cases undergo substantial changes in σ_{SEI}, corresponding to the approximately 3~4 orders of magnitude decrease (10^{-5} → 10^{-9} S cm^{-1} for Na-glyme and 10^{-7} → 10^{-10} S cm^{-1} for Na-carbonate). The degree of densification (the degree of the change in the proportion of the liquid/solid materials constituting the SEI) is higher for the Na SEI in comparison to the Li SEI, which may have been caused by the mechanical pressure built up in the electrochemical cells.

3.2.4. Chemical composition of the SEIs over depth: XPS and ToF-SIMS results

The chemical compositions of the SEIs are investigated with XPS and ToF-SIMS. Figure 20 and Figure 21 show the XPS results of the Li SEIs formed by the contact with glyme-based liquid electrolyte. The outer-most surface is oxidized (Li^+) and composed of residual salts (-CF_3), organic Li compounds ($ROCO_2Li$), Li_2CO_3 and sulfide compounds (C-S, SO_4^{2-}). As the Ar^+ etching progresses, Li becomes reduced (Li^+ → Li^0). Li_2CO_3, LiF, sulfide compounds (C-S, SO_4^{2-}, SO_3^{2-}, Li polysulifdes), organic Li compounds ($ROCO_2Li$) and Li_2O are present throughout the whole layer. Since Li_2CO_3, LiF and Li_2O have already been observed for pure Li (see chapter 3.1), the XPS peaks are most likely from the SEI formed by the chemical reactions as well as from the native films of Li.

No difference in chemical composition is observed in the SEIs aged for 2 hours and 600 hours. SEIs on Li formed by the contact with carbonate-based electrolyte have similar chemical compositions as shown in Figure 22 and Figure 23. Note that the peaks are identified based on the binding energy values from the literature. [112, 113, 131] However, it is important to mention that

the etching time is not directly proportional to the SEI depth, and thus the same etching time for different samples does not necessarily indicate the same depth. This is due to the sample roughness and porosity. In such case, the sample surface is not uniformly etched when the Ar^+ beam is injected in a specific spatial direction.

Additionally, ToF-SIMS measurements were carried out to examine the relative salt concentration over depth. If the SEI is porous, electrolytes will infiltrate the pores and upon drying the electrode for XPS and ToF-SIMS sample preparations, only the solvent in the pores will evaporate, leaving the salts precipitated in the pores. Thereby, the existence of the salt in depth of the SEI becomes an indication of the porous SEI. Figure 24 shows ToF-SIMS depth profiles for four different systems (Li-glyme, Li-carbonate, Na-glyme and Na-carbonate). In the case of Li, the $CF_3SO_3^-$ intensity decreases significantly over sputtering time (~1% at the beginning and ~0.001% after 800 hours of sputtering, normalized intensity). On the contrary, Na systems show much higher intensities of $CF_3SO_3^-$ (~1% throughout the entire sputtering time), which implies the existence of the salt in the SEI bulk. The results support the claim that SEIs on Na are more porous compared to the ones on Li. However, it should be noted that the ToF-SIMS data should be analyzed only qualitatively, not quantitatively. Here, the sputtering time is again not proportional to the sample depth due to the same roughness issue, and the intensity is also not directly proportional to the concentration of $CF_3SO_3^-$, since the intensity is a complex function of the element type and the surrounding materials.

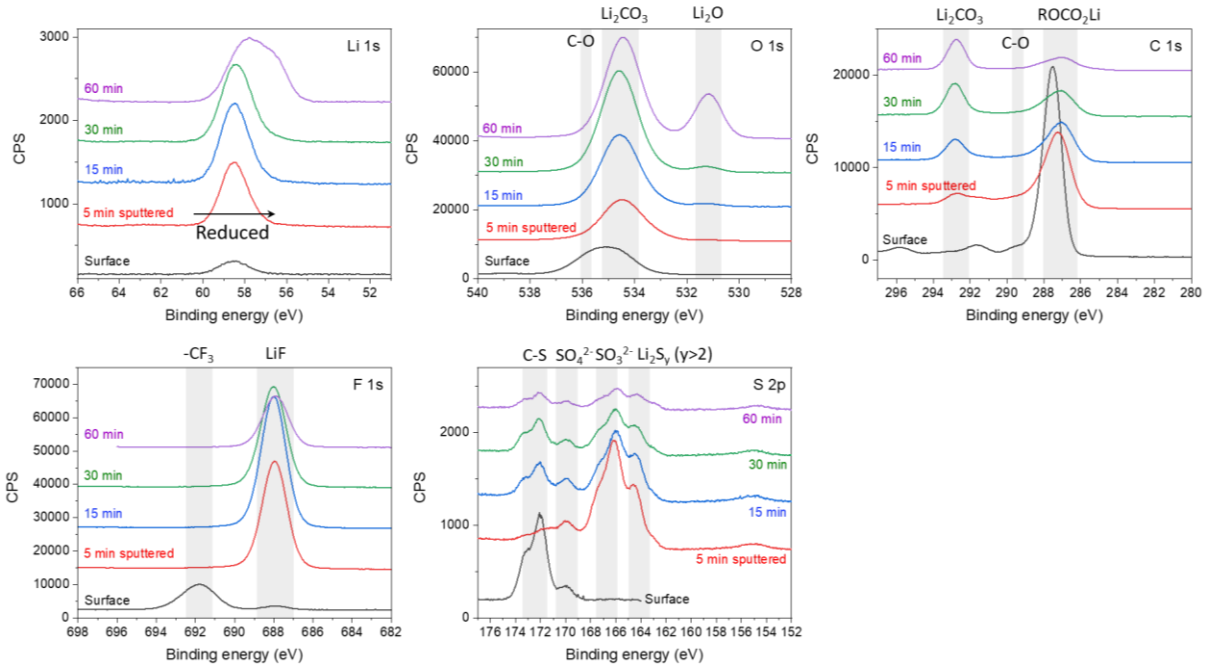

Figure 20. XPS spectra of SEI on Li formed by the contact with glyme-based liquid electrolyte (1M LiTf in triglyme) for 2 hours. The surface was measured at first and the following measurements were done after 5, 15, 30, 60 minutes of etching with Ar^+ beam. The chemical compounds corresponding to the peaks are stated.

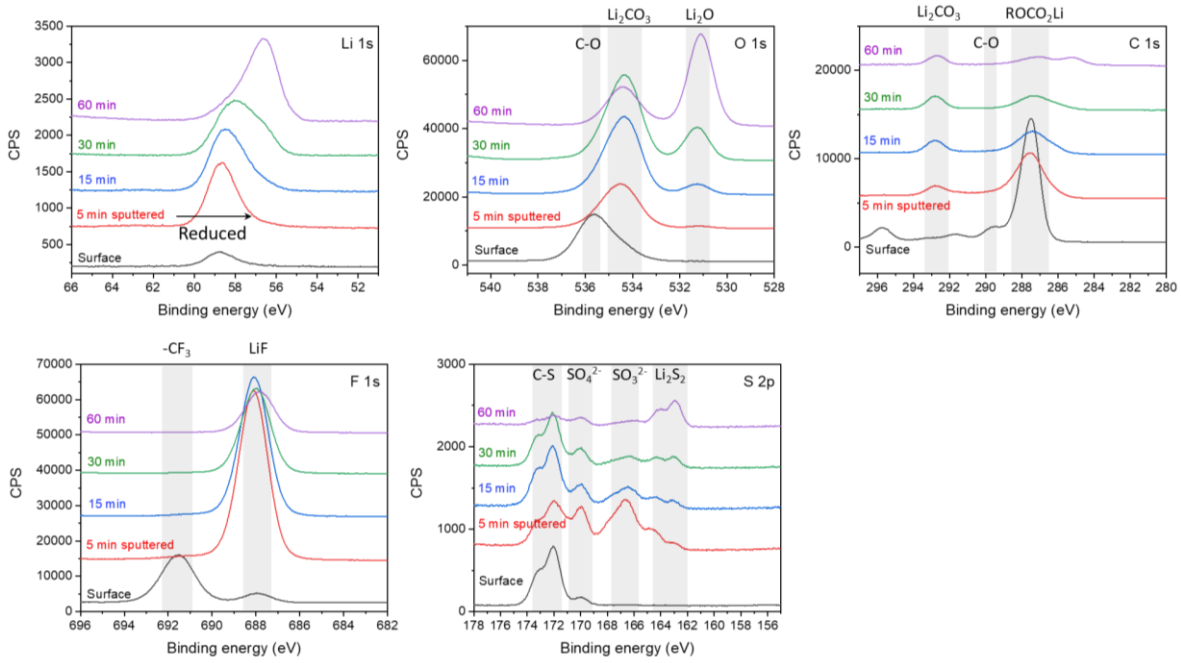

Figure 21. XPS spectra of SEI on Li formed by the contact with glyme-based liquid electrolyte (1M LiTf in triglyme) for 600 hours

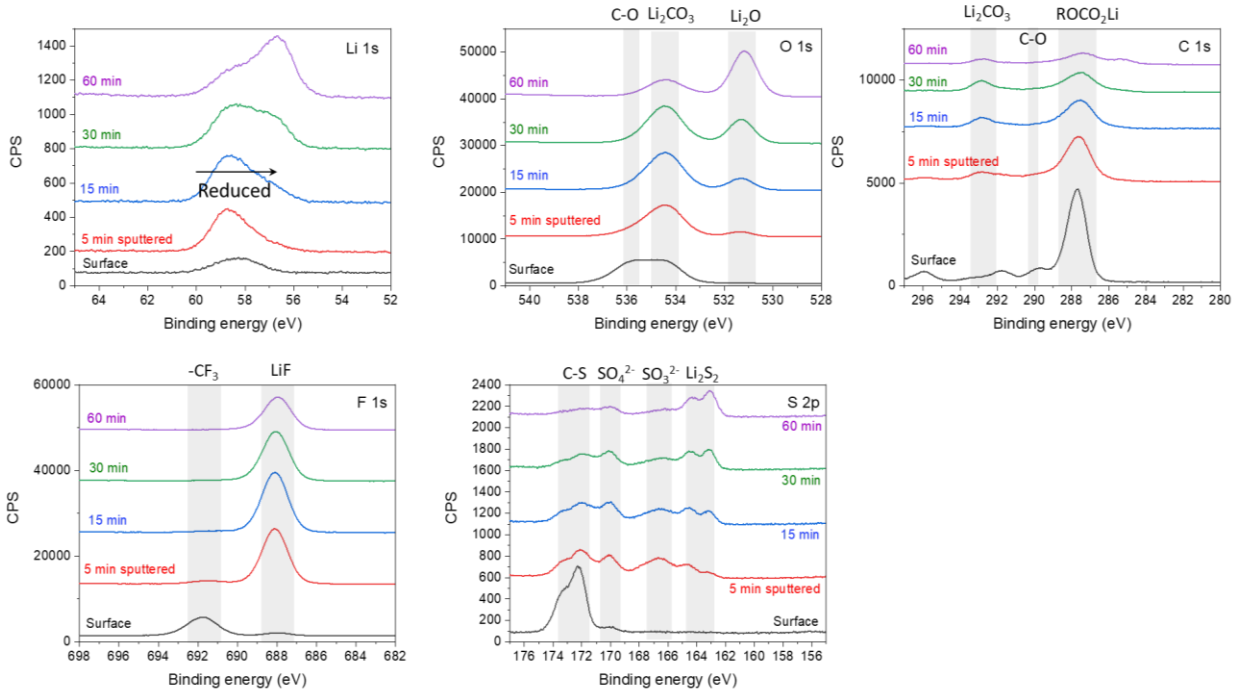

Figure 22. XPS spectra of SEI on Li formed by the contact with carbonate-based liquid electrolyte (1M LiTf in EC/DMC) for 2 hours

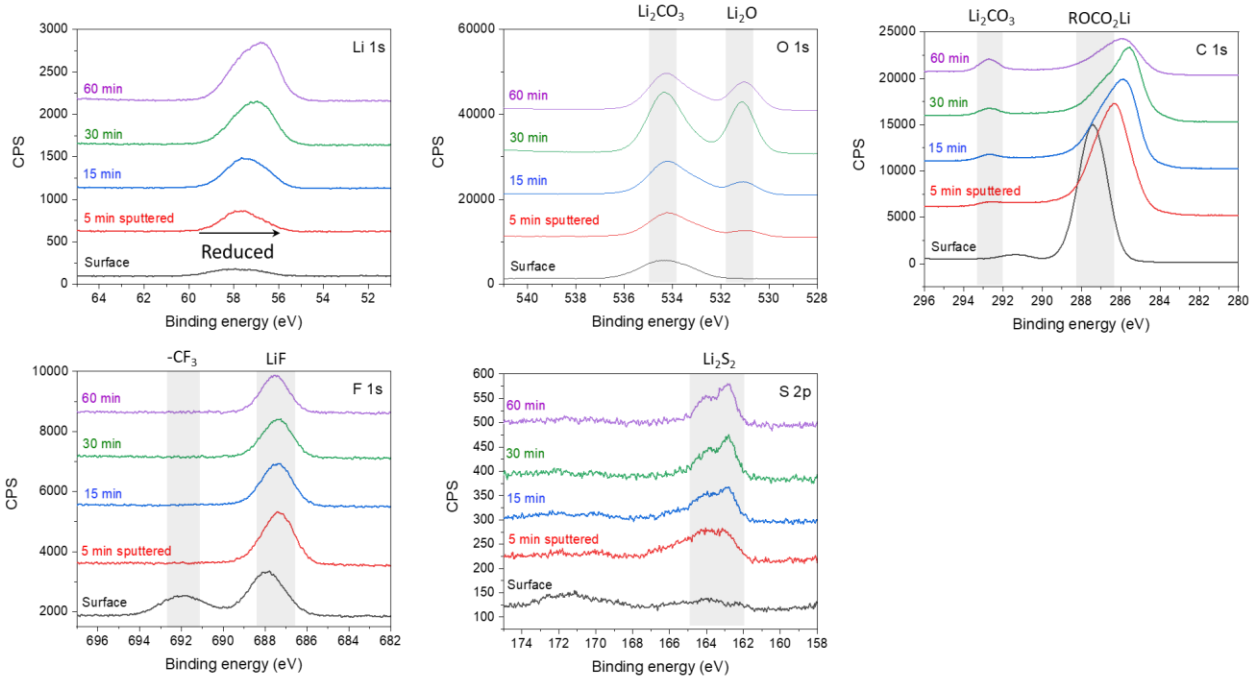

Figure 23. XPS spectra of SEI on Li formed by the contact with carbonate-based liquid electrolyte (1M LiTf in EC/DMC) for 600 hours.

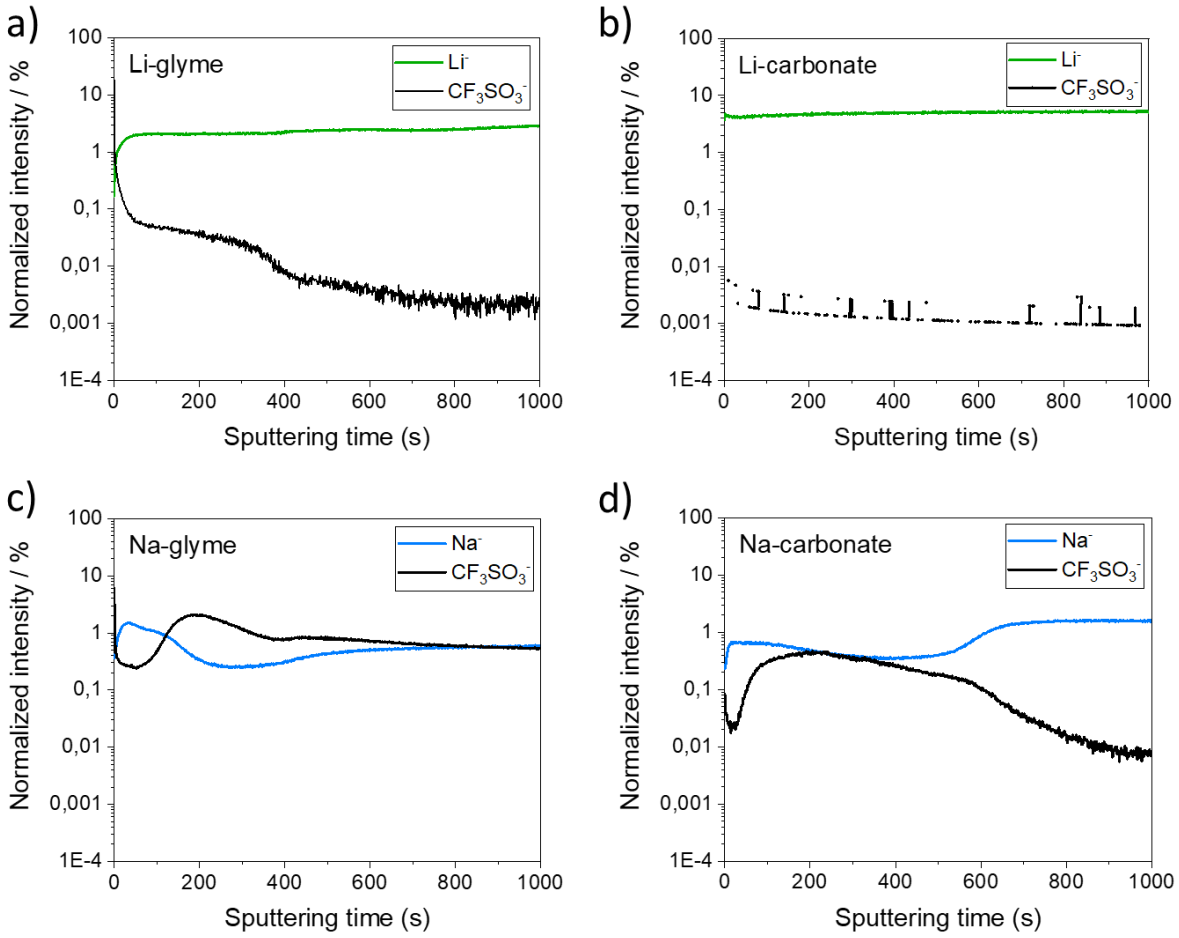

Figure 24. ToF-SIMS depth profiles of SEIs on Li/Na formed by the contact with liquid glyme- and carbonate-based electrolytes for 600 hours. (a) Li contacted with 1M LiTf in triglyme, (b) Li contacted with 1M LiTf in EC/DMC, (c) Na contacted with 1M NaTf in triglyme and (d) Na contacted with 1M NaTf in EC/DMC. The ion intensities were normalized to the total ion count for each sputtering time data point.

3.2.5. Origin of the porosity of Na SEIs

Activation energies of ion transport in the SEIs, cross-section images measured by FIB-SEM and ToF-SIMS measurements show that the SEIs on Na are more porous compared to the ones on Li. The fundamental origin of the porosity is not completely clear yet, but we attribute it to the molar volume difference between the formed SEI compounds and metallic Na. As introduced in

part 1.2.1, the ratio of these two molar volumes is termed Pilling-Bedworth ratio (R_{PB}). [69] As an example, the chemical reaction between Li and S is expressed as

$$2Li\ (s) + 1/8S_8\ (s) \longrightarrow Li_2S\ (s). \quad (3.2)$$

In this case, R_{PB} is

$$R_{PB} = \frac{V_{Li_2S}}{2V_{Li}} \quad (3.3)$$

where V_{Li} and V_{Li_2S} are the molar volumes of Li and Li_2S. The R_{PB} values for Li/Na inorganic compounds are listed in Table 5.

Table 5. List of R_{PB} of Li SEI compounds *vs.* Na SEI compounds

Li SEI compounds		**Na SEI compounds**	
Compound	$\boldsymbol{R_{PB}}$	**Compound**	$\boldsymbol{R_{PB}}$
LiF	0.76	NaF	0.69
Li_2O	0.57	Na_2O	0.58
Li_2O_2	0.76	Na_2O_2	0.59
Li_2CO_3	1.35	Na_2CO_3	0.88
LiOH	1.26	NaOH	0.79
LiH	0.75	NaH	0.72
Li_2S	1.06	Na_2S	0.89
		Na_2S_2	1.16
		Na_2S_4	1.79
		Na_2S_5	2.17

The noticeable difference between Li and Na is that R_{PB} values of Na SEI compounds are smaller than 1, except for the Na polysulfides. Since polysulfides are a series of many SEI compounds stemming from the salt decomposition (as the salt contains S), the proportion of the Na polysulfides is expected to be very low. The fact that the molar volumes of most inorganic Na SEI compound

are smaller than the molar volumes of reacted metallic Na may be a reason behind the SEI porosity. However, this cannot be the complete explanation for the porosity as the molar volumes of organic SEI compounds should be taken into account, and the SEI could also be densified by the external mechanical stress applied in the electrochemical cells. [132] The detailed investigation of the molar volumes of organic SEI compounds and the mechanical properties is required in the future.

3.2.6. Cation transference number and salt diffusion coefficient of the liquid electrolytes

In the previous parts, it has been concluded that liquid electrolytes significantly contribute to the ion transport in SEIs owing to the SEI porosity. In this part, the ion transport behavior in the liquid electrolytes used for this study is examined in detail. One of critical electrolyte parameters for battery application is the effective transference number of cations (Li^+ or Na^+) (t_{eff}). The cation transference number is defined as the ratio of the electric current stemming from the cations in the electrolyte to the total electric current. If t_{eff} is smaller than 1, a concentration gradient in the liquid electrolyte forms when a constant current is applied. [133] The salt diffusion coefficient (D_{salt}) is directly proportional to the ionic conductivity according to the Nernst-Einstein equation. Furthermore, both t_{eff} and D_{salt} are related to Sand's time (*i.e.* characteristic time at which the salt concentration on the surface becomes zero at the electrode), which is the time needed for a dendrite to be formed. Note that Sand's time presumes a chemically and mechanically uniform electrode. [134] Sand's time (t_{sand}) is expressed as [135]

$$t_{sand} = \pi D_{salt} \left(\frac{z_c C_0 F}{2J(1 - t_{eff})} \right)^2 \tag{3.4}$$

where C_0 is the bulk electrolyte concentration, F is the Faraday constant and J is the current density. Thereby, t_{eff} and D_{salt} are two crucial factors for describing the ion transport in the

electrolyte which are responsible for the concentration polarization, ionic conductivity and dendrite formation. These two parameters are determined by combining EIS and galvanostatic polarization (see part 2.2.2 for detailed information about the working principles). Table 6 provides the summary of cation transference numbers and salt diffusion coefficients. The polarization profiles are given in Figure 25. Compared to Li, t_{eff} of Na in glyme-based electrolyte is considerably higher, possibly correlated to the less-solvated Na^+ compared to Li^+, owing to the size effect. [136] Determining a transference number of 1M NaTf in EC/DMC was challenging due to the high reactivity of Na with the electrolyte, making it difficult to reach a steady-state. In addition, the R_{SEI} quickly changes within the period of changing the electrochemical devices (galvanostatic polarization→EIS) necessary for the measurements. For the Na-glyme case, small R_{SEI} allows the impedance signal from diffusion process in the bulk liquid electrolyte to be visible, so cation transference number can be derived from the EIS (t_{EIS}) with low frequency (~1 mHz) using the Sørensen-Jacobsen method (Figure 26). A small disparity between the t_{eff} value derived from the galvanostatic polarization and the one from the Sørensen-Jacobsen method is observed (0.42 *vs.* 0.36). Both methods assume an identical geometry of the electrodes before and after the polarization, but the geometry could change over the current density applied. [137] This different experimental condition might have led to the different transference number values.

Table 6. Summary of the effective cation transference numbers (t_{eff}) and salt diffusion coefficients derived from the galvanostatic polarization methods. t_{EIS} refers to the transference number measured by the method using only EIS suggested by Sørensen and Jacobsen. [124]

Electrolytes	t_{eff} **(polarization)**	D_{salt} **/ cm^2 s^{-1}**
1M LiTf in triglyme	0.24	1.0×10^{-7}
1M LiTf in EC/DMC	0.12	2.8×10^{-6}
1M NaTf in triglyme	0.42 (t_{EIS}=0.36)	1.7×10^{-6}
1M NaTf in EC/DMC	*N/A*	5.8×10^{-8}

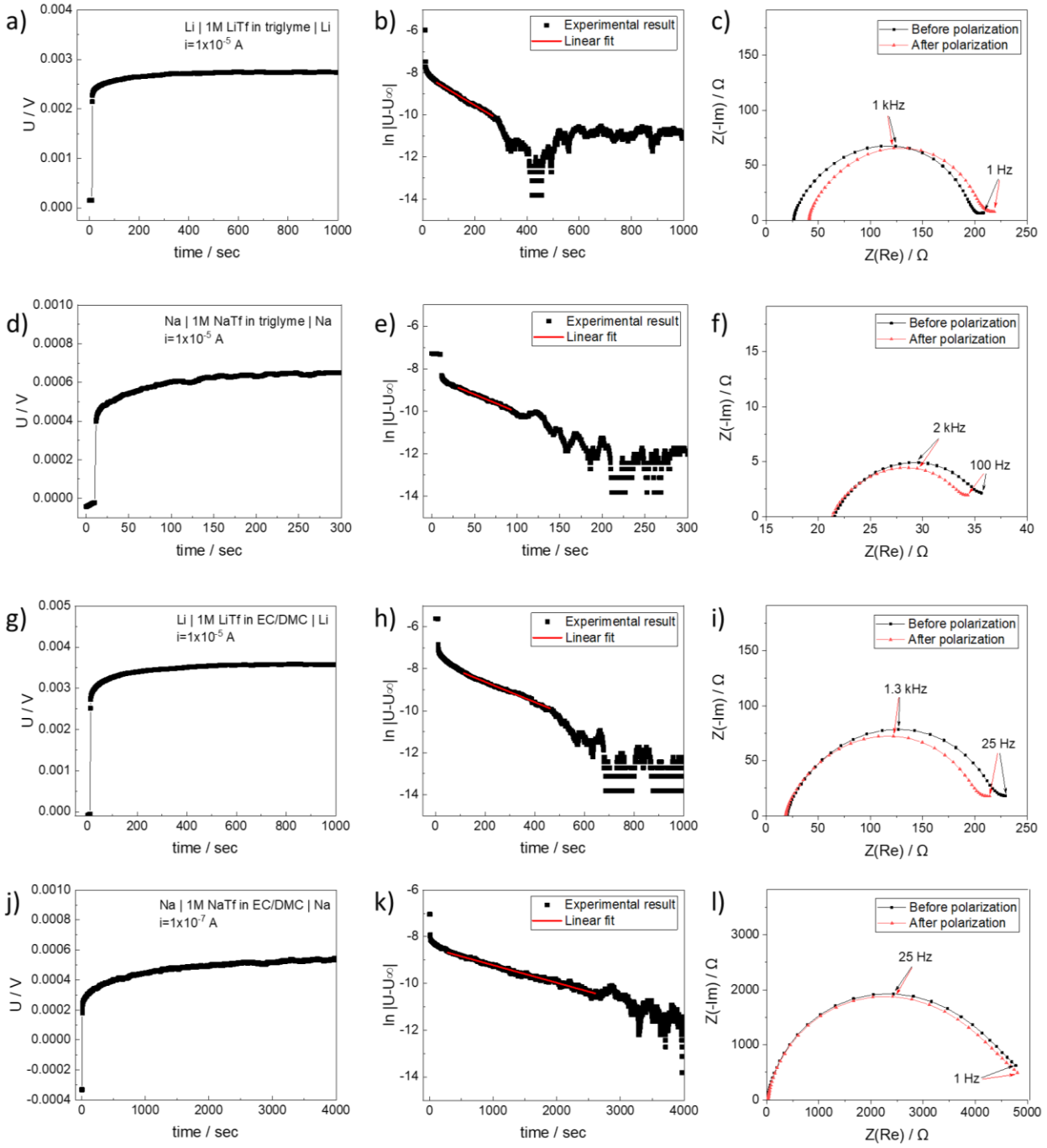

Figure 25. Galvanostatic polarization profiles to determined the cation transference number (t_{eff}) and salt diffusion coefficient (D_{salt}). (a-c) 1M LiTf in triglyme, (d-f) 1M NaTf in triglyme, (g-i) 1M LiTf in EC/DMC, and (j-l) 1M NaTf in EC/DMC. For the time *vs.* $\ln|U-U_\infty|$ profiles, red line shows the linear fit with which the equation (2.10) is applied to derive salt diffusion coefficients.

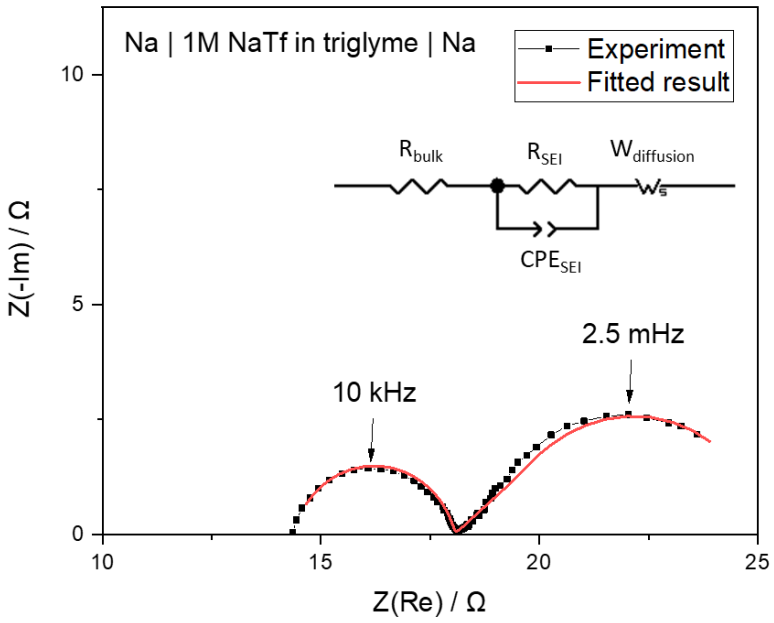

Figure 26. Impedance spectrum of Na-glyme system measured in the frequency range of 10^{6}~10^{-3} Hz. The inset shows equivalent circuit model for fitting the spectrum and the fitted result is marked as red color.

3.2.7. Stripping-plating results of symmetric Li/Na cells

Cyclic stripping-plating experiments were performed by applying constant current density (0.1 mA cm^{-2}), as such electrode performance is of great importance for the battery application. Figure 27 shows the time *vs.* voltage profiles of stripping-plating behaviors in four different Li/Na symmetric cells with glyme- and carbonate-based electrolytes. In general, the cells aged for 600 hours (red) show higher overpotential compared to the one without aging (black), and even cell failures due to the high overpotential are observed (Figure 27a, b and d). Since the only difference between those two (0 hour *vs.* 600 hours of aging) is the density of the SEIs, the stripping-plating results suggest that the densified SEIs are not beneficial for the cell operation, possibly due to the detrimental mechanical properties of the dense SEI. [9] Alkali metal electrodes undergo volume

expansion during the deposition process, and the electrodeposition occurs in a spatially non-uniform way, which causes the local stress. A porous SEI provides room to relieve the stress, while a dense SEI does not. Figure 28 shows the surface of the Li/Na electrodes after stripping-plating in Figure 27. The SEM images provide the clue for explaining the stripping-plating behaviors. In case of Li contacted with glyme-based electrolyte (Figure 28a), cracks in the SEI are clearly observable in the Li stored for 600 hours followed by stripping-plating, indicating that the SEI most likely has broken mechanically during the electrochemical cycling process. A similar behavior was observed in the case of Na with carbonate-based electrolyte (Figure 28d). For the Na-glyme case, an unstable stripping-plating behavior was detected (Figure 27b) but the surface is observed to be smooth (Figure 28b). The reason remains unclear, but it is suspected that the dissolution of Na SEI compounds in the electrolyte plays a significant role. [138, 139]

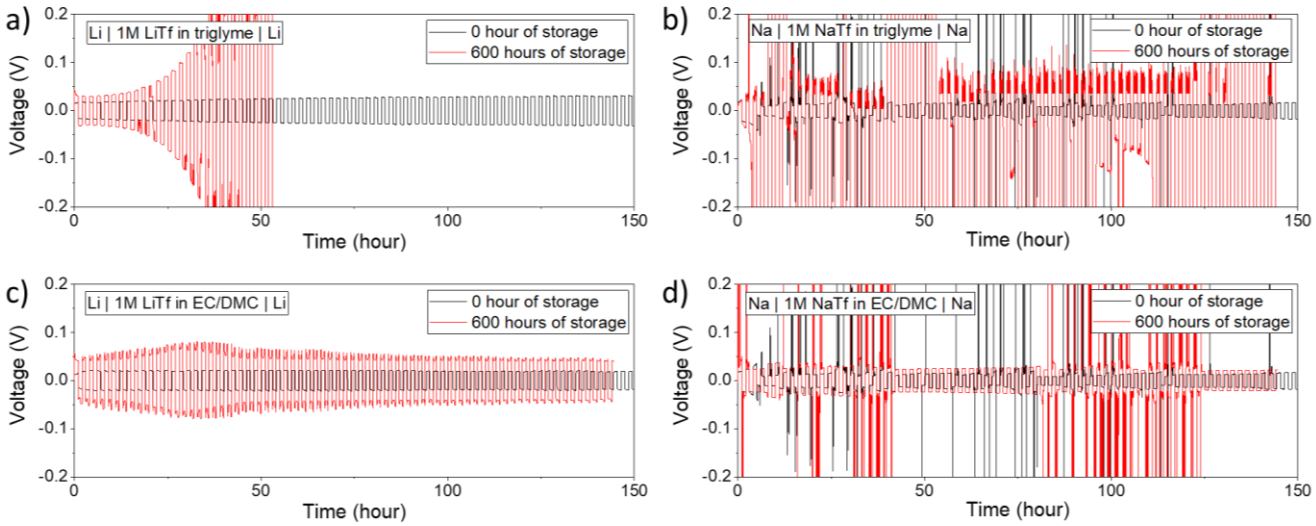

Figure 27. Stripping-plating behaviors of symmetric Li/Na cells with glyme- and carbonate-based electrolytes. The cells were measured right after assembly (black) and after 600 hours of storage under open-circuit. The applied current is 0.1 mA cm^{-1}.

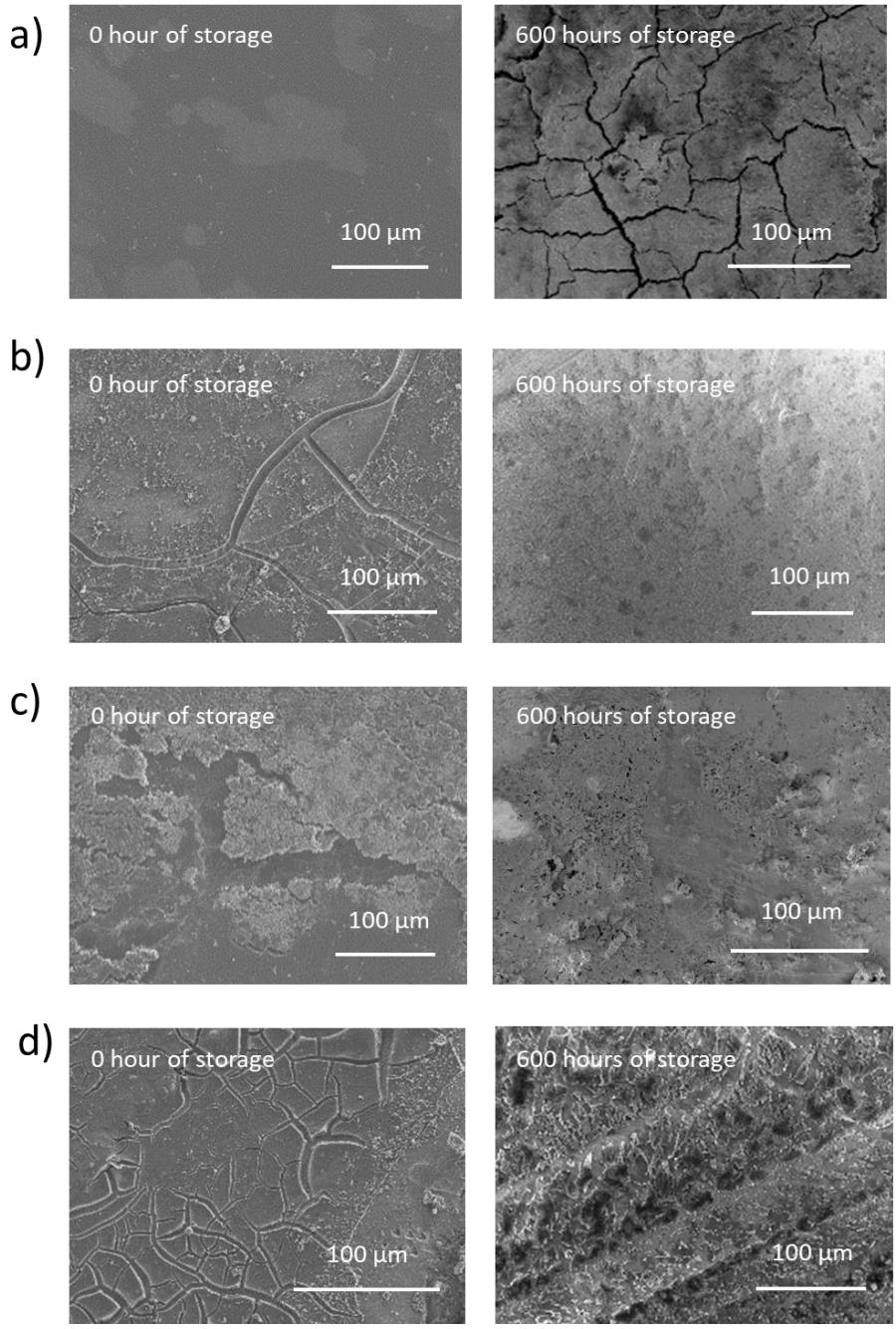

Figure 28. Top-view SEM images of the Li/Na electrodes after stripping-plating with glyme-and carbonate-based electrolytes right after cell assembly (left) and after 600 hours of storage under open-circuit (right). (a) Li with 1M LiTf in triglyme, (b) Na with 1M NaTf in triglyme, (c) Li with 1M LiTf in EC/DMC and (d) Na with 1M NaTf in EC/DMC.

3.3. Equivalent circuit models for the ion transport in the porous SEI

Understanding impedance response requires a suitable equivalent circuit model which reflects the physical/chemical properties of the system. Studies providing such equivalent circuit models for SEIs, especially for porous SEIs, are very rare owing to their complexity. [140-142] Figure 29 is the schematic diagram of the physical SEI structure consisting of dense bulk SEI and a channel (in reality a pore) infiltrated by liquid electrolyte. Since the liquid electrolytes are not thermodynamically stable against Li/Na, it is expected at least a thin solid film on the surface of the alkali metals (noted as solid in channel in Figure 29) is present. The solid in channel could be the reaction product or native films which already had existed on the alkali metal surface, or it can also be established by the charge transfer across the double layer. In the following, we will not distinguish between these phenomena and describe them by a single series impedance. This film provides a serial resistance to the liquid in the channel, and such channels are in parallel to the

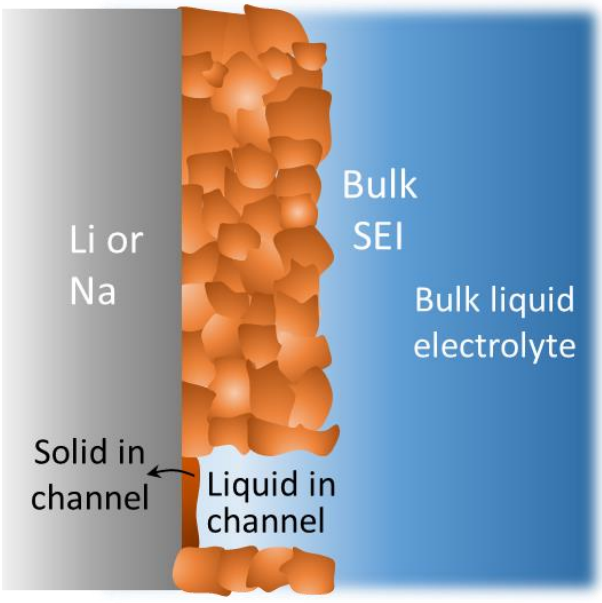

Figure 29. Schematic diagram of the physical structure of the SEIs on Li/Na. The orange bricks represent the different chemical compounds composing the SEI. Note that a number of complex pores rather than a single channel exist in the real system.

surrounding dense bulk SEI. At any rate, the major transport pathway determines the activation energy of the overall resistance. The analysis of the activation energy has the advantage that it is independent of the SEI geometry. Table 7 summarizes the E_a of transport through the SEIs and SEI capacitances derived by impedance measurements. The significance of the liquid in a channel follows from the fact that ionic conductivities of the liquid electrolytes (~10^{-3} S cm^{-1}) are at least 7 orders of magnitude higher than the ones of solid SEI compounds (<10^{-10} S cm^{-1}, see Table 1 and Table 2). Thereby, the major ion transport pathways are most likely be the channel where the thin solid layer and the liquid are connected in series. The blocking influence of the solid in a channel will become dominant only if its thickness is perceptible.

Table 7. Summary of the activation energies of the ion transport through SEI (E_a (SEI)) and SEI capacitances (C_m) obtained in the symmetric Li/Na cells with glyme- and carbonate-based electrolytes stored under open-circuit condition for 2 hours. C_m was calculated from $C_m = \frac{1}{2\pi f R_{SEI}}$, where f is the peak frequency where the $|Z_{Im}|$ value becomes maximum for the semicircle corresponding to the SEI.

System	E_a **(SEI) / eV**	C_m **/ F**
Li | 1M LiTf in triglyme | Li	0.52	8.33×10^{-7}
Li | 1M LiTf in EC/DMC | Li	0.55	8.79×10^{-7}
Na | 1M NaTf in triglyme | Na	0.15	5.52×10^{-6}
Na | 1M NaTf in EC/DMC | Na	0.30	1.25×10^{-6}

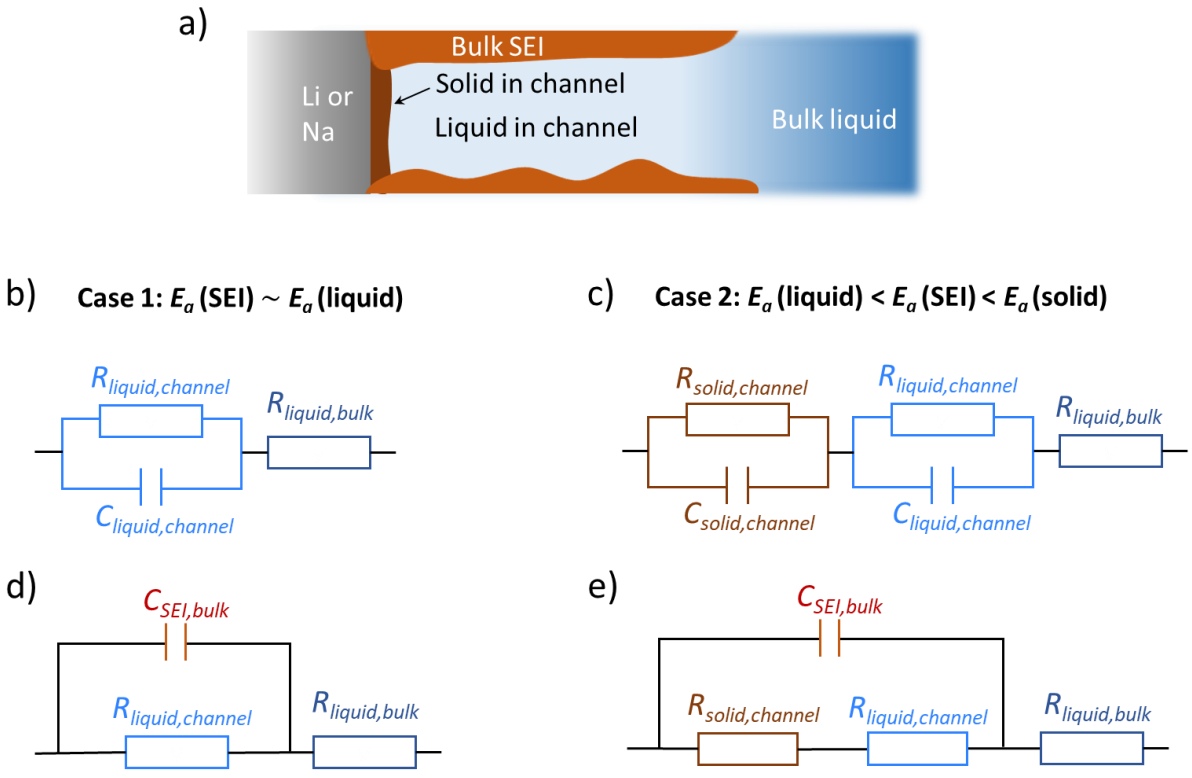

Figure 30. (a) Schematic diagram of the major ion transport pathway (liquid channel) of the SEI. (b, c) Equivalent circuit models of the SEI's ion transport in the liquid channel. (b) for the case of Na-glyme system where the E_a (SEI) is identical to the E_a of transport in bulk liquid electrolyte, (c) for other cases (Li-glyme, Li-carbonate and Na-glyme) in which the E_a is in between the ones of liquid electrolytes and solid SEI compounds. (d, e) for the situation where the capacitances from the bulk SEI are taken into account and the ones from solid/liquid in channel are neglected.

Figure 30a depicts the liquid channel of the SEIs, in which the major ion transport occurs. The resistances and capacitances of the each component are noted as $R_{SEI,bulk}$, $C_{SEI,bulk}$ (for bulk SEI), $R_{solid,channel}$, $C_{solid,channel}$ (for the solids in channel), and $R_{liquid,channel}$, $C_{liquid,channel}$ (for the liquids in channel). Solids and liquids in the channel are connected in series and they are linked with the bulk SEI in parallel. Figure 30b and c show the equivalent circuit models corresponding to the ion transport in the liquid channel. Depending on the E_a(SEI) values, the models are categorized into two cases: Case 1 (Figure 30b, d) is the situation in which E_a(SEI) is close to the E_a of ion transport in the liquid electrolytes and Case 2 (Figure 30c, e) represents the case where E_a(SEI) in between the ones of liquid electrolytes and solid SEI compounds. Case 1 includes the Na-glyme system and

Case 2 covers Li-glyme, Li-carbonate and Na-carbonate systems for the initial storage. For Case 1, $R_{solid,channel}$ and $C_{solid,channel}$ may be neglected according to the impedance spectra simulation by the ZView software as shown in Figure 31. The RC parallel circuits of thin SEI and liquid in the channel are simplified into $R_1||C_1$ and $R_2||C_2$ (|| represents the parallel connection). Based on the fact that the dominant ion transport mechanism in the SEI of Na-glyme system occurs in the liquid electrolyte, it was assumed that $R_1 << R_2$ is valid. The C_1 and C_2 values are unknown, thus three different cases ($C_1 >> C_2$, $C_1 \sim C_2$ and $C_1 << C_2$) are examined. All simulations in Figure 31 suggests that no matter how large the capacitance values are, the impedance spectra, as well as effective capacitance,e are always dominated by the R_2 and C_2 parallel circuit. Thereby, R_1 and C_1 are neglected.

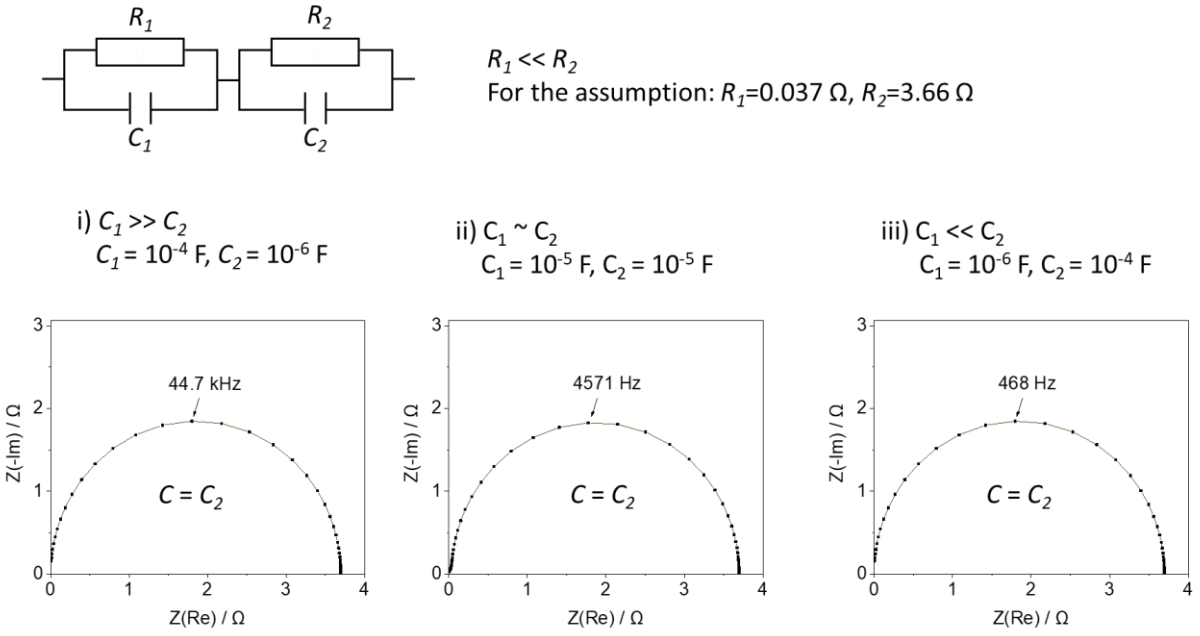

Figure 31. Justification for neglecting the $R_{solid,channel}$ and $C_{solid,channel}$ for the Case 1 (E_a(SEI)~E_a(liquid)) in Figure 31b. Three impedance spectra for two RC parallel circuits connected in series are simulated. Since R_{SEI} for Na-glyme system is measured to be 3.67 Ω, R_1=0.037 Ω and R_2=3.66 Ω was assumed.

Now the validity of the equivalent circuit models in Figure 30b and c are examined. Ionic conductivities of the liquid electrolyte in the channel ($\sigma_{liquid,channel}$) are estimated based on the following equations.

$$R_{liquid,channel}C_{liquid,channel} = \frac{\varepsilon_0\varepsilon_{liquid,channel}}{\sigma_{liquid,channel}} = \frac{1}{2\pi f_{peak}} \quad (3.5)$$

where ε_0 is the vacuum permittivity, $\varepsilon_{liquid,channel}$ is the dielectric constant of the liquid electrolyte in the channel and f_{peak} is the peak frequency where the $|Z_{Im}|$ of the semicircle corresponding to the $R_{liquid,channel}$ and $C_{liquid,channel}$ has a maximum value. According to equation (3.5),

$$\sigma_{liquid,channel} = 2\pi\varepsilon_0\varepsilon_{liquid,channel}f_{peak} \quad (3.6)$$

Given by the measured EIS frequency range in Figure 33, the $\sigma_{liquid,channel}$ values are calculated to be smaller than 1.7×10^{-6} S cm^{-1}. Note that $\varepsilon_{liquid,channel}$<30 was assumed, based on the dielectric constant values of the liquid organic electrolytes in the literature. [143, 144] The obtained $\sigma_{liquid,channel}$ values are at least 3 orders of magnitude smaller than the ionic conductivities of bulk liquid electrolytes (~10^{-3} S cm^{-1}), which is improbable, meaning that the equivalent circuit models need to be modified.

The so far neglected RC elements corresponding to the bulk solid SEI ($R_{SEI,bulk}$ and $C_{SEI,bulk}$) connected in parallel with the liquid pathways are now considered. If a parallel resistance ($R_{SEI,bulk}$) is added, $R_{liquid,channel}$ has to increase as the total SEI resistance is fixed. Then, $\sigma_{liquid,channel}$ values would be even lower according to the equation (3.5) Also, addition of $R_{SEI,bulk}$ would make the E_a(SEI) even more solid-like. Now, the parallel capacitance ($C_{SEI,bulk}$) is considered (shown in Figure 30d and e). In this case, $C_{liquid,channel}$ has to decrease, in order to adjust the values of the total SEI capacitance, resulting in an increase of $\sigma_{liquid,channel}$. Taking the capacitance of the bulk SEI

into account is anyway reasonable in view of the small area fraction of the channels and the similar dielectric constants of the solid/liquid phases. [143, 145] It is important to have this before, in order not to make the argument circular. Therefore, the parallel SEI bulk capacitance must be included in the equivalent circuit models. The $C_{SEI,bulk}$ should be 2~3 orders of magnitude higher than the $C_{liquid,channel}$, in order to obtain the reasonable $\sigma_{liquid,channel}$ values. In addition to the higher area fraction of bulk SEI, the high capacitance of bulk SEI could also be due to resistive grain boundaries therein. To conclude, for porous SEI, the overall SEI resistance is dominated by the channel ($R_{channel} = R_{solid,channel} + R_{liquid,channel}$) while the SEI capacitance is dominated by the bulk solid SEI (which exists in parallel with the liquid channels). Therefore, the relaxation time (τ) may be expressed as

$$\tau \cong R_{channel} \cdot C_{SEI,bulk}. \tag{3.7}$$

For the Case 2 where E_a (SEI) is in between the ones of liquid electrolyte and solid SEI compounds, the thickness of the thin SEI layer ($d_{solid,channel}$) can be derived as a function of E_a(solid,channel) and $\sigma_{solid,channel}$, based on the activation energies. Firstly, R_{SEI} can be described as

$$R_{SEI} = R_{solid,channel} + R_{liquid,channel}. \tag{3.8}$$

Since $E_a \approx -R\frac{\partial ln\sigma}{\partial(1/T)}$ (where R is the gas constant, T is the temperature) and $\partial ln\sum y_i = \sum(\frac{y_i}{\sum y_i}\partial ln y_i)$ [146], equation (3.8) transforms into

$$E_a(SEI) = \frac{R_{solid,channel}}{R_{solid,channel} + R_{liquid,channel}} E_a(solid, channel) + \frac{R_{liquid,channel}}{R_{solid,channel} + R_{liquid,channel}} E_a(liquid, channel) \tag{3.9}$$

where E_a(solid,channel) and E_a(liquid,channel) correspond to the activation energies of ionic transport through thin SEI layer and liquid in the channels, respectively. Finally, Eq. (3.9) can be rearranged in respect of the thin SEI thickness as

$$d_{solid,channel} = \frac{\sigma_{solid,channel} d_{SEI} (E_a(SEI) - E_a(liquid,channel))}{(E_a(solid,channel) - E_a(SEI))(\sigma_{liquid,channel} - \sigma_{solid,channel})}. \quad (3.10)$$

The d_{SEI} values can be taken from the FIB-SEM cross-section images in Figure 18 and Figure 19. The values of $\sigma_{liquid,channel}$ and E_a(liquid,channel) may be taken from temperature-dependent EIS measurements in Figure 16. Now the unknown two parameters in the equation for $d_{solid,channel}$ in (3.10) remain ionic conductivity and activation energy of ion transport through thin solid SEI ($\sigma_{solid,channel}$ and E_a(solid,channel), respectively). First, these values are estimated to be in the physically probable range, based on the σ_{ion} and E_a values of the Li/Na inorganic SEI compounds (Table 1 and Table 2, 10^{-11} S cm^{-1} < $\sigma_{solid,channel}$ < 10^{-5} S cm^{-1} and 0.3 eV < E_a(solid,channel) < 1.1 eV). Figure 32 shows the obtained 3-dimensional plots of the relationship between $d_{solid,channel}$, $\sigma_{solid,channel}$ and E_a(solid,channel). In order for the $d_{solid,channel}$ to be in the realistic range (several nanometers to tens of nanometers), the $\sigma_{solid,channel}$ needs to be higher than 10^{-7} S cm^{-1} and E_a(solid,channel) is required to be lower than 0.7 eV (shaded as light blue-green-yellow area in Figure 32). This implies that the thin SEI layer has to be at least 3~4 orders or magnitude more conductive, and to have lower activation energy compared to the bulk SEI layer. This could be probable in nano-sized materials with space-charge effects being relevant, which may be true to a different chemical nature of the solid in a channel. [147] High-dimensional

defects such as grain boundary, dislocation or partially amorphous regions may play significant roles as transport pathways [148].

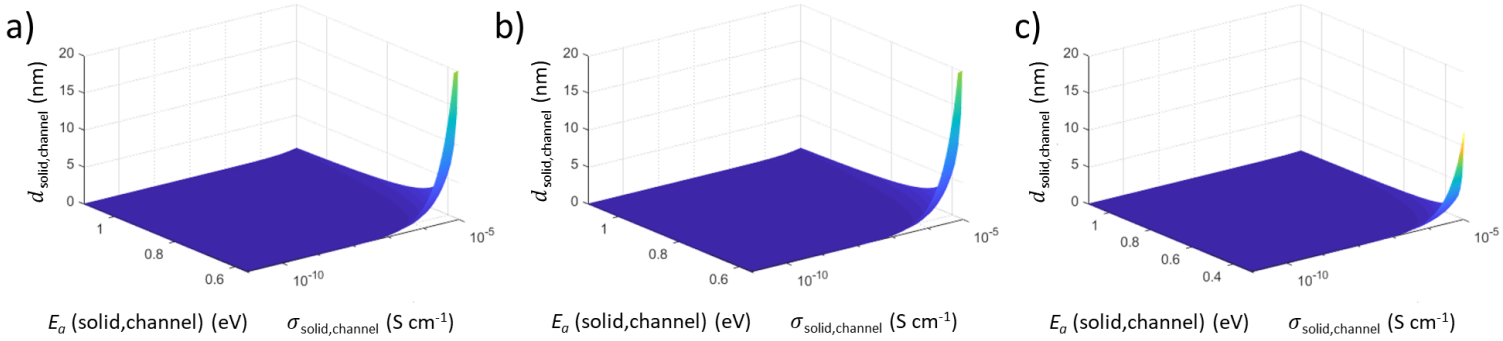

Figure 32. Dependence of the thin SEI layer thickness ($d_{solid,channel}$) on the activation energy of ion transport in thin SEI (E_a (solid,channel)) and ionic conductivity of thin SEI ($\sigma_{solid,channel}$) for (a) Li-glyme, (b) Li-carbonate and (c) Na-carbonate. The relationship between three parameters is given in the Equation (3.10).

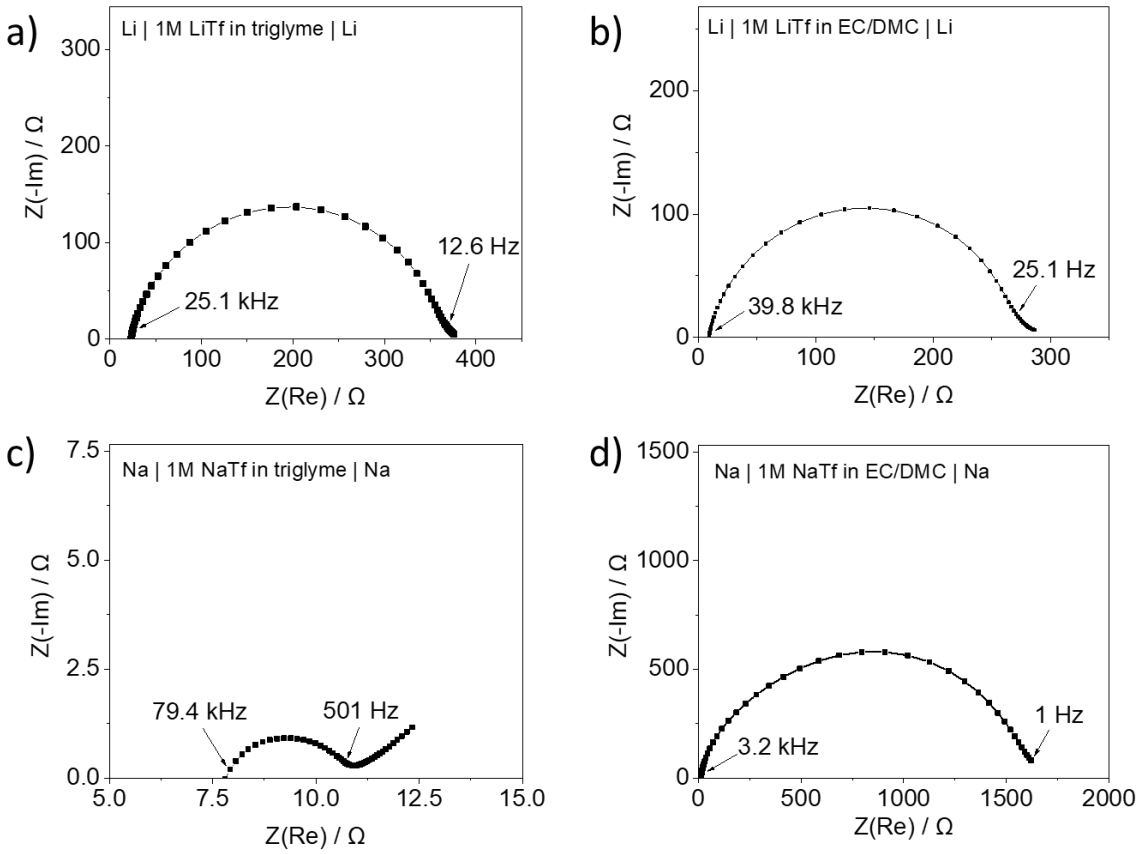

Figure 33. Impedance spectra obtained from the symmetric Li and Na cells with glyme- and carbonate-based electrolytes stored for 2 hours under open circuit condition.

3.4. Long-term SEI growth behavior under open-circuit potential

Based on the ion transport mechanism discussed previously, the growth behavior of the SEIs on Li/Na with glyme- and carbonate-based electrolytes is observed under open-circuit for 600 hours. Figure 34 shows the SEI resistances (R_{SEI}), SEI capacitances (C_{SEI}) and relaxation times ($\tau = R_{SEI} \cdot C_{SEI}$) change over time for four different systems. Note that the SEI capacitances were derived from the single semicircle corresponding to the SEI in the impedance spectra by

$$C_{SEI} = \frac{1}{2\pi R_{SEI} f_{peak}}. \quad (3.11)$$

Significant differences between Li and Na are observable in their SEI growth behaviors. In the case of Li, changes of R_{SEI}, C_{SEI} and τ over aging are relatively mild (Figure 34a~f, at least the values maintain to be in the same orders), which implies that the SEI grows in a coherent way when the solid-state diffusion dominates the growth. On the contrary, SEIs on Na undergo drastic changes of R_{SEI}, C_{SEI} and τ (Figure 34g~k). This distinguishable SEI growth behavior on Na is most probably attributable to its porosity. The porous SEI allows the infiltration of the liquid electrolyte into the channels that allows for the Na contact to liquid electrolyte, inducing subsequent chemical reactions. Such chemical reactions lead to the growth of SEI with the increase of both R_{SEI} and E_a(SEI) over time, as shown in Figure 34g and i.

The SEI growth behavior in Na-glyme system appears to be unique compared to other systems, as the abrupt increase of R_{SEI} is observed after approximately 280 hours of storage (Figure 34g). Additional Na-glyme electrochemical cells (six in total) assembled in a same experimental condition were measured to examine the reproducibility of this extraordinary R_{SEI} increase behavior, and the results in Figure 35 show that such abrupt increase of R_{SEI} happens in all six Na symmetric cells. The origin of this rapid R_{SEI} increase is not clear yet, since at this moment it is

experimentally difficult to perform an *in situ* or *ex situ* characterization of such phenomenon. The probable scenario is either that the liquid channels (in reality pores) become blocked by solid SEI compounds caused by the external pressure built up in the electrochemical cells, or the lateral SEI growth. The intermittent R_{SEI} drop after 280 hours of storage (Figure 34g) might be attributable to the SEI dissolution into the liquid electrolyte, which was already shown by the literature dealing with Na metal battery with carbonate-based liquid electrolytes. [139, 149, 150] Another possibility is the mechanical instability originating from the continuous pore formation owing to the non-ideal values of R_{PB} (<1) for the Na inorganic compounds (explained in 3.2.5). In the same way as the low R_{PB} values causes channel formation of the macroscopic SEI, the solid in a channel is expected to break up and form tiny pores or channels. If so, in principle this leads to a formation of a self-similar SEI structure, meaning that the porous SEI structure is created continuously on a smaller scale. The schematic diagram of such SEI-growth in Na-glyme system is depicted in Figure 36. The self-similar behavior is corroborated by the irregular behavior shown in Figure 34g, where the time intervals between the SEI resistance breakdowns become continuously smaller. SEI on Na is initially porous, where the ion transport mainly occurs through the liquid channels (A in Figure 36), followed by the densification or pore blocking, resulting in the increase of the resistance (B). The SEI formation reaction continues in the liquid channels with mechanical instabilities (C), and this process repeats in a self-similar manner (D).

The observation of R_{SEI} growth in a Na-glyme system is noteworthy, since the previous reports claim that Na forms relatively stable and ionically conductive SEIs in combination with glyme-based electrolytes compared to the carbonate-based electrolytes. [151-153] Contrary to this argument, here the presented results reveal that the low R_{SEI} in Na-glyme system does not stem from intrinsic SEI properties, but rather from the liquid electrolyte in the channels of the SEIs. The

transport through liquid channels appears to be linked with the small SEI resistance but finally induces SEI growth and densification. In contrast to the R_{SEI} growth behavior in Na-glyme system, the C_{SEI} does not change as much as the R_{SEI} does (Figure 34e). This most likely indicates that the capacitance is majorly contributed by the bulk SEI capacitance ($C_{SEI,bulk}$) and is in agreement with the equivalent circuit model suggested in the previous chapter. The SEI growth behavior in Na-carbonate system is comparatively more monotonic (Figure 34i). The origin of these different behaviors of Na SEI growth in glyme-based electrolyte *vs.* carbonate-based electrolyte needs to be studied in the future. Obviously, this has to do with the different polymeric/organic SEI products from the solvent decomposition, as similar salts were used in these systems.

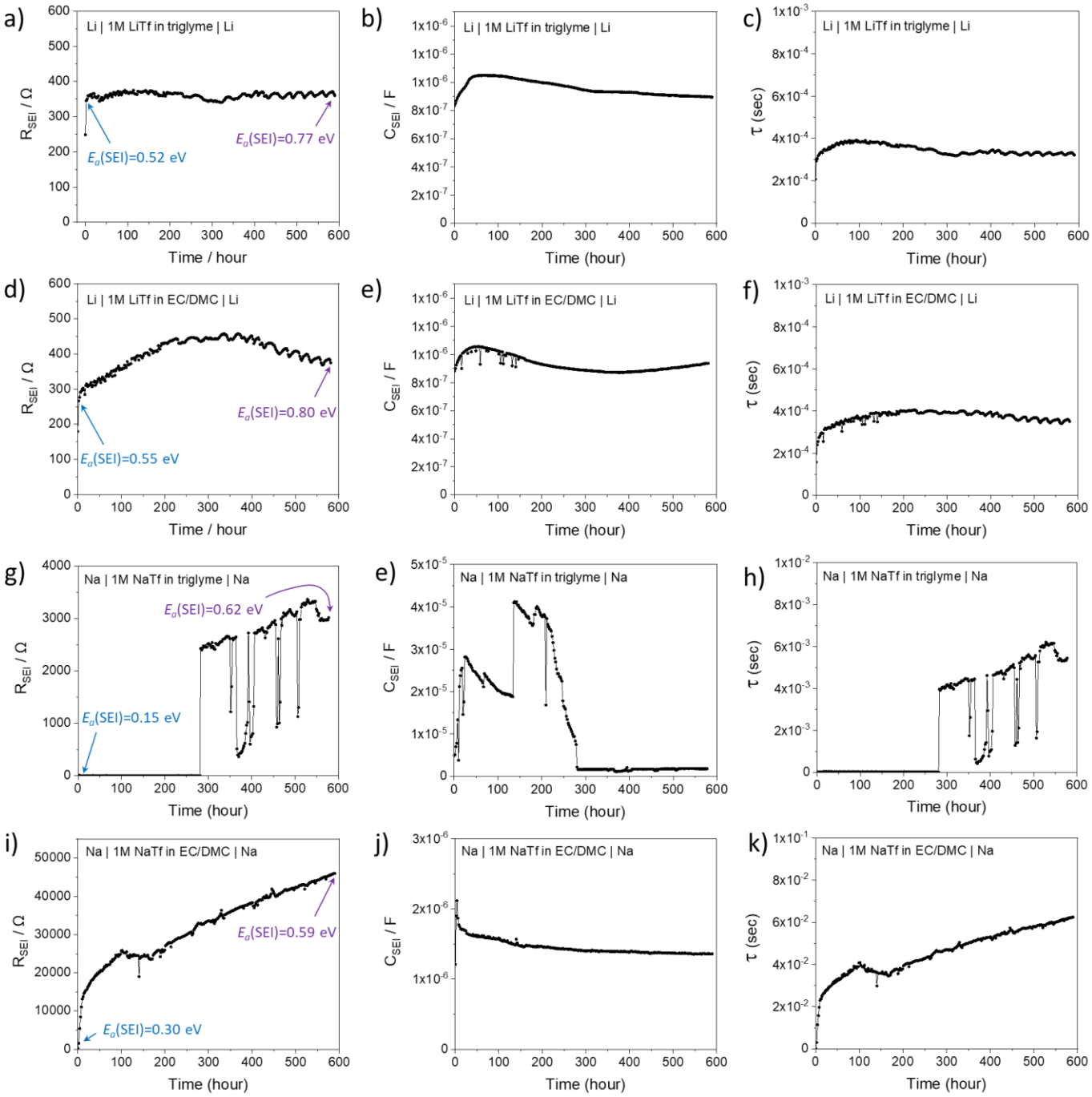

Figure 34. SEI resistances (R_{SEI}), SEI capacitances (C_{SEI}), and relaxation times ($\tau = R_{SEI} \cdot C_{SEI}$) changes over time in (a-c) Li-glyme, (d-f) Li-carbonate, (g-h) Na-glyme, and (i-k) Na-carbonate systems stored under open-circuit condition. The activation energies of ion transport in SEI (E_a (SEI)) measured at the initial storage and after the 600 hours of storage are marked with blue and purple, respectively.

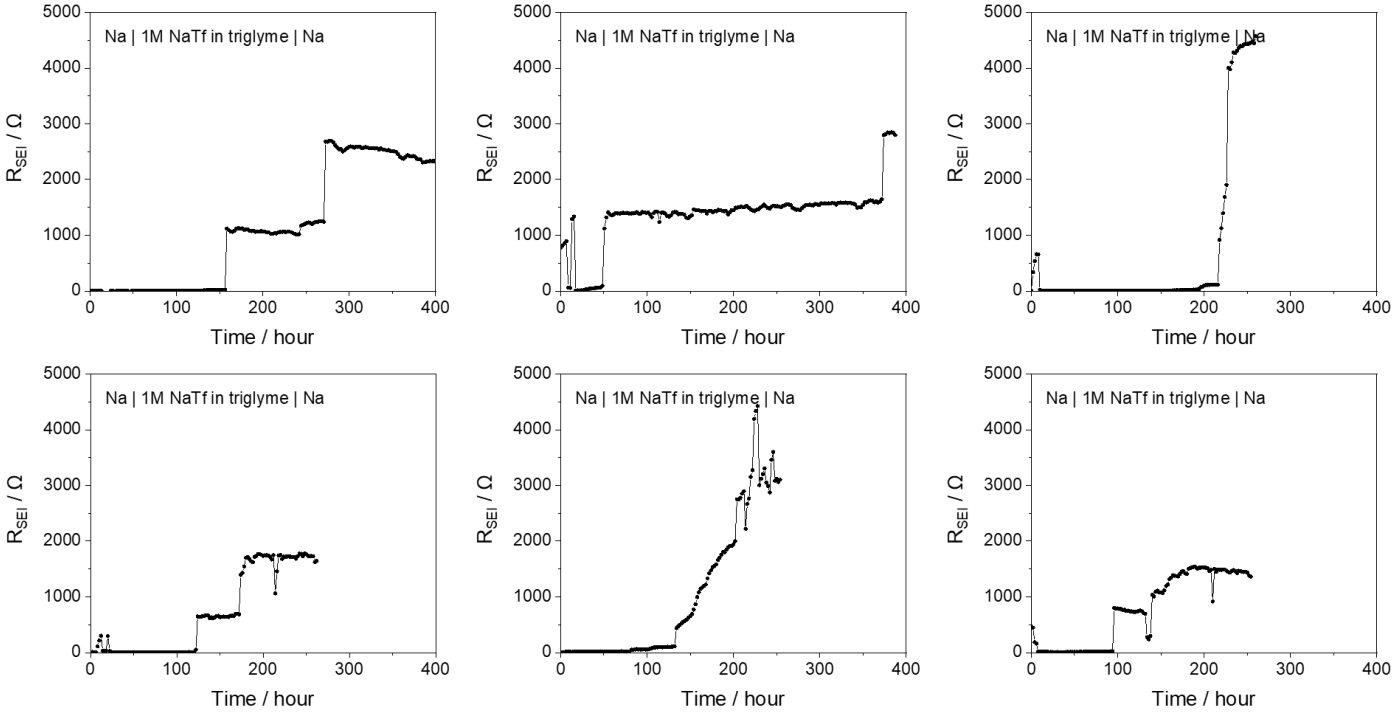

Figure 35. R_{SEI} changes over time under open-circuit in six Na-glyme systems (all six cells were assembled under the same experimental condition as in Figure 34g) for reproducibility check.

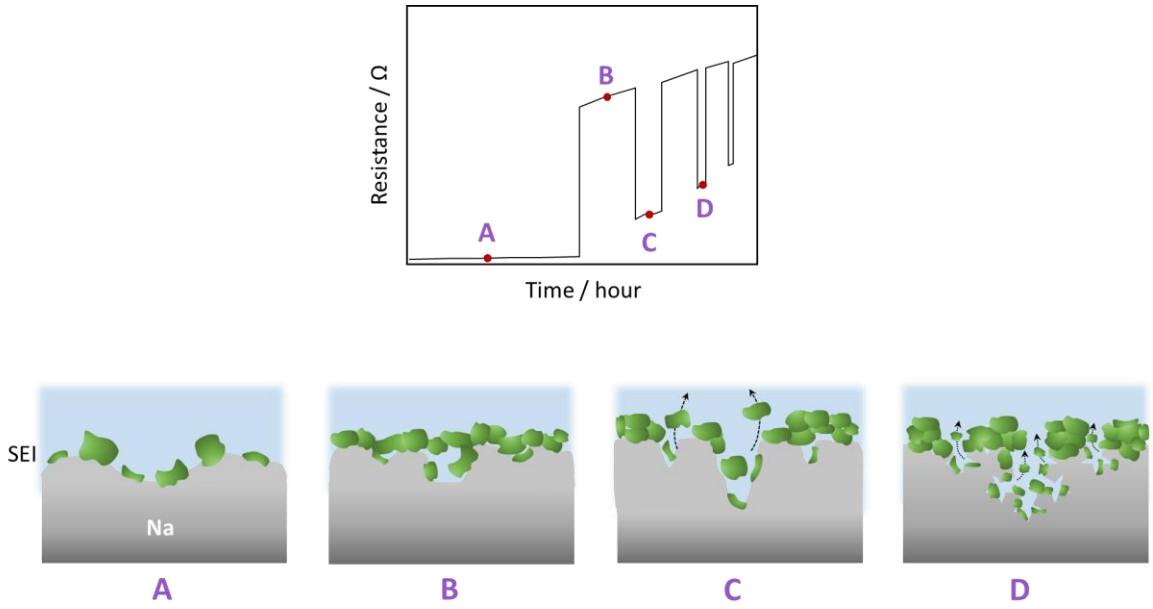

Figure 36. Schematic diagram of the time-dependent SEI resistance growth behavior shown in Figure 34g (above) and the corresponding sketches of SEI's morphological evolutions (below).

3.5. Conclusion

This chapter deals with the native films on Li/Na as well as the SEIs on Li/Na formed by the contact with glyme- and carbonate-based electrolytes.

First, the FIB-SEM and XPS investigations on the commercial Li and the MBE-grown-Li reveals that the pure Li is covered with native films composed of oxides, fluorides and carbonates. The detailed examination on the native films on Na is challenging owing to its high chemical reactivity, but similar chemical composition as observed for Li is expected.

Second, the E_a(SEI) measurements with EIS show that ion transport in the SEI on Na is dominated by the transport in liquid electrolyte in the pores, when both the pure glyme solvent and salt-included glyme- and carbonate-based liquid electrolyte are used. Higher values of E_a(SEI) for Li SEIs suggest that SEIs on Li are denser, which is also supported by FIB-SEM images and ToF-SIMS measurements. The porosity of the SEI on Na is most likely attributable to the R_{PB} values of the inorganic Na SEI compounds which are smaller than one. In the course of aging of the Li/Na electrochemical cells under open-circuit, the SEIs become densified, as confirmed with the increased values of E_a(SEI). Stripping-plating behaviors of symmetric cells with the liquid electrolytes are compared in Li *vs.* Na and the cells without aging *vs.* after aging for 600 hours, and it is concluded that the dense SEIs are not beneficial for the galvanostatic cycling.

Lastly, a suitable equivalent circuit model for porous SEI is suggested based on the measured E_a(SEI) values and the measured frequency ranges. The model implies that for porous SEI, liquid channels connected to the thin solid SEI layer are the major transport pathway, while the SEI capacitance is dominated by the bulk SEI, in which the channels are embedded. The pores allow

the infiltration of the liquid electrolyte, which finally induces irregular continuous growth of the SEIs. This is noticeable in all Na cases, where the continuous SEI growth is observed.

4. Artificially-formed SEIs on Li/Na

4.1. Sulfide-based SEIs formed by solid-vapor chemical reaction

The results of this section is published in [154].

4.1.1. Morphological and chemical characterization of sulfide-based SEIs on Li/Na

The synthetic method for sulfide-based SEI (Li_xS_y and Na_xS_y) is explained in detail in part 2.1.2. The following equations (along with literature data of the formation free enthalpy) are the expected chemical reactions between the alkali metals and the S vapor.

$$2\ Li\ (s) + \frac{1}{8} S_8\ (g) \rightarrow Li_2S\ (s) \qquad \Delta_f G^\circ = -466\ KJ\ mol^{-1}\ [155] \qquad (4.1)$$

$$2\ Na\ (s) + \frac{1}{8} S_8\ (g) \rightarrow Na_2S\ (s) \qquad \Delta_f G^\circ = -398\ KJ\ mol^{-1}\ [156] \qquad (4.2)$$

It should be noted that Li_2S is the only thermodynamically stable solid phase in the Li-S system [157],while in Na case other Na polysulfides such as Na_2S_2, Na_2S_4 and Na_2S_5 can be formed [158].

Figure 37 shows the morphological/chemical characterization results of the Li_xS_y and Na_xS_y synthesized under specific condition (T_{Li}=140 ˚C, T_S=25 ˚C for 2 hours for Li and T_{Na}=T_S=80 ˚C for 2 hours for Na, where T is a synthesis temperature). First, cross-section images measured by FIB-SEM (Figure 37a and d) show different morphology between Li and Na. Li_xS_y appears to be more continuous and uniform in comparison to Na_xS_y, which is observed to be rough and porous. Note that the existence of the S in the synthesized layer is confirmed with energy dispersive X-ray (EDX) characterization which is shown in Figure 40. The underlying reason for the morphological difference is most likely owing to the R_{PB} of Li_2S (1.06) and Na_2S (0.89). The thickness of the sulfide film can be controlled by changing the synthesis temperature as shown in Figure 38 and

Figure 39. The general trend of the film thickness dependence on the temperature is that the film becomes thicker as the synthesis temperature ($T_{Li\ (or\ Na)}$ and T_S) increases. However, it should be noted that the film thicknesses are not always identical in every part of the sample, most likely owing to the native films on the surface of Li and Na, which hinders the chemical reaction with S vapor. The artificial SEI films (Li_xS_y and Na_xS_y) having thicknesses of ~490 nm and ~150 nm for Li and Na, respectively, are investigated with a variety of chemical characterization tools and the results are shown in Figure 37. XRD results (Figure 37b and e) clearly show the crystalline phase of Na_2S on Na, but for Li, only the metallic phase (substrate) is detected. The investigation with XPS in Figure 37c suggests that the Li_2S phase is formed on the surface of Li, along with other sulfur-related phases such as sulfate (SO_4^{2-}), sulfite (SO_3^{2-}) and polysulfide (Li_2S_y, y>1), while in the bulk part only the Li_2S is present. The peak positions and the corresponding references for identifying the phases are listed in Table 8. Polysulfide species are known to be thermodynamically unstable as solids [157], so they must be present as metastable phases, similarly as in the previously reported sputter-deposited thin films [159]. Based on the XRD and XPS results of Li_xS_y, it is believed that the Li_2S phase is either amorphous or present as crystalline phase but in amounts too small to be detected with XRD. Considering the fact that the intensity of the diffracted X-ray beam is a function of the atomic number, Li compounds in general have smaller XRD intensity compared to Na compounds, which might result in no significant signals in XRD in Figure 37b. In Na case, ToF-SIMS was performed on the Na_xS_y film and the results are shown in Figure 37f. As the sputtering progresses (meaning that as it goes into depth), the concentration of Na decreases while the one of S increases, implying the concentration gradient forms within the Na_xS_y film throughout the depth. The common observation in Li_xS_y and Na_xS_y films is that the surface is more oxidized (in terms of S) in comparison to the bulk part, which is analogous to the oxidation of metals (e.g.

oxides on Fe). [160, 161] A more detailed investigation with cryo-TEM would be helpful to clarify the porosity, crystal structure and compositional distribution of the films.

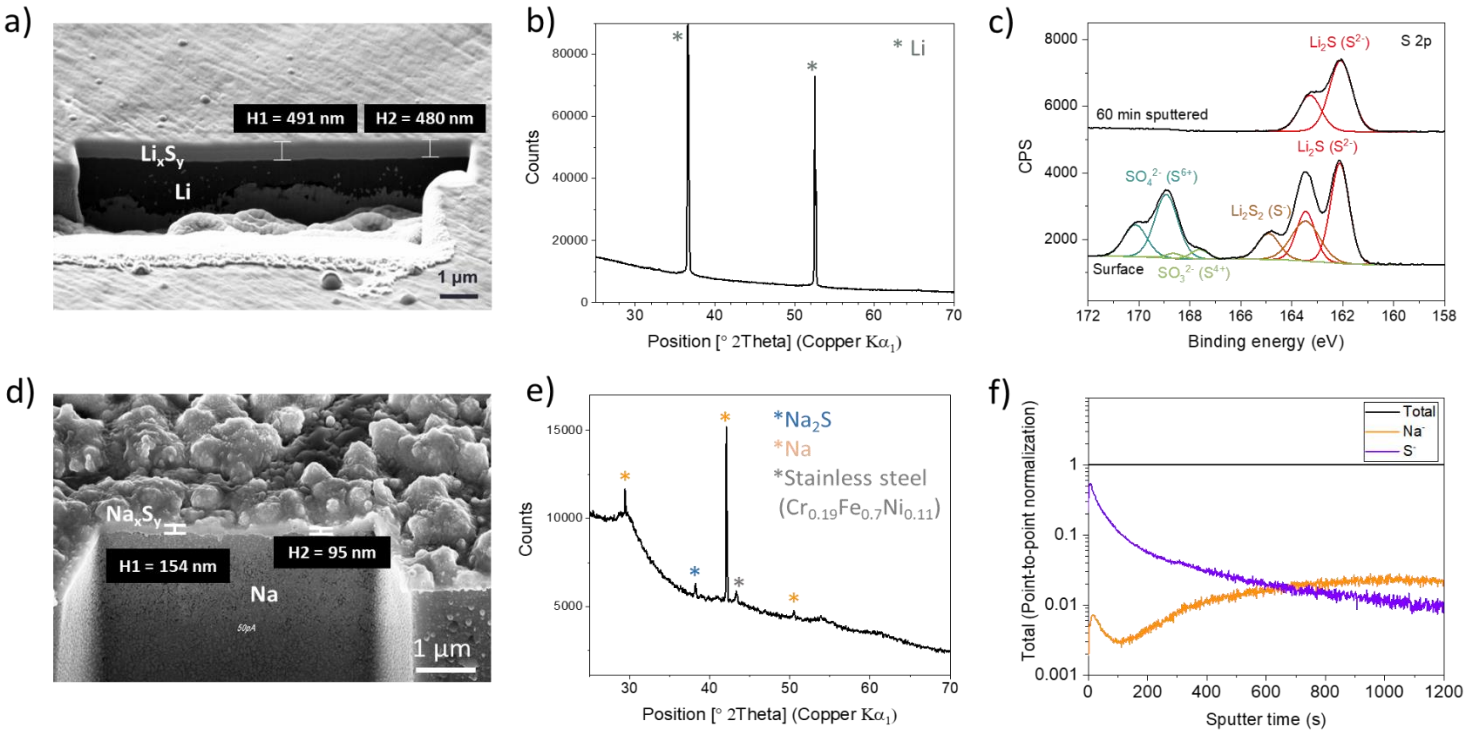

Figure 37. Morphological and chemical characterization results of sulfide-based artificial SEIs on Li (a-c) and Na (d-f). (a, d) Cross-section images from FIB-SEM, (b, e) XRD patterns, (c) XPS spectra (black) collected on the surface of the Li_xS_y (below) and after Ar^+ sputtering for 60 minutes. The red, brown, green and blue spectra correspond to Li_2S, Li_2S_2, SO_3^{2-} and SO_4^{2-}, respectively, and they were fitted to the spectra as described in the experimental section. (f) ToF-SIMS depth profile on Na_xS_y. Li_xS_y was synthesized at T_{Li}=140 ˚C, T_S=25 ˚C for 2 hours and Na_xS_y was synthesized at T_{Na}=T_S=80 ˚C for 2 hours.

Table 8. Binding energies and full width at half maximum (FWHM) values of different sulfide species of XPS. References for the identification of the species are listed.

Species	Binding energy (eV)	FWHM (eV)	References
Li_2S (S^{2-})	162.1	0.86	[111]
Li_2S_2 (S^{-})	163.5	1.31	[113]
SO_3^{2-} (S^{4+})	167.6	0.80	[156]
SO_4^{2-} (S^{6+})	168.9	1.07	[162]

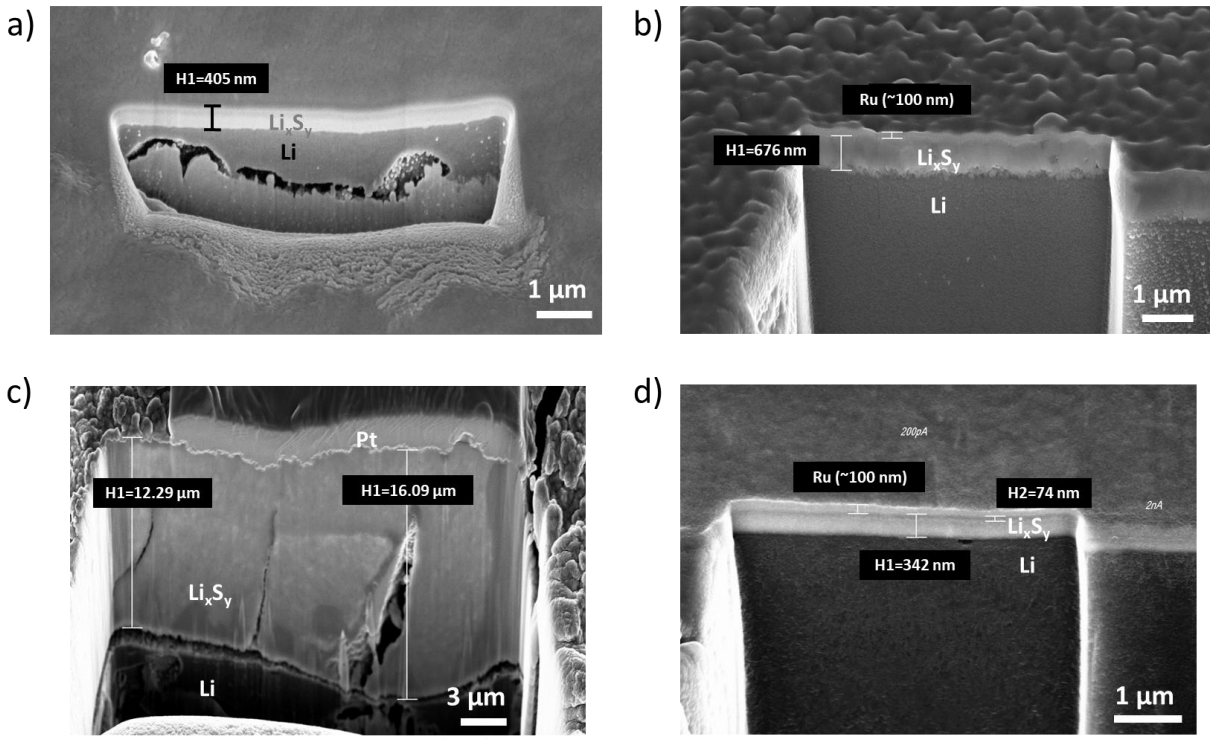

Figure 38. FIB-SEM cross-section images of Li_xS_y on Li synthesized under different temperatures. (a) T_{Li}=T_S=60 ˚C, (b) T_{Li}=T_S=100 ˚C, (c) T_{Li}=T_S=120 ˚C, (d) T_{Li}=120 ˚C, T_S=25 ˚C. The synthesis proceeded for 2 hours. In (b-d), films were coated with Pt or Ru prior to the measurements, to avoid the potential risk of the exposure to the air. Note that cracks (or pores) in (a) and (c) are formed during milling with focused ion beam.

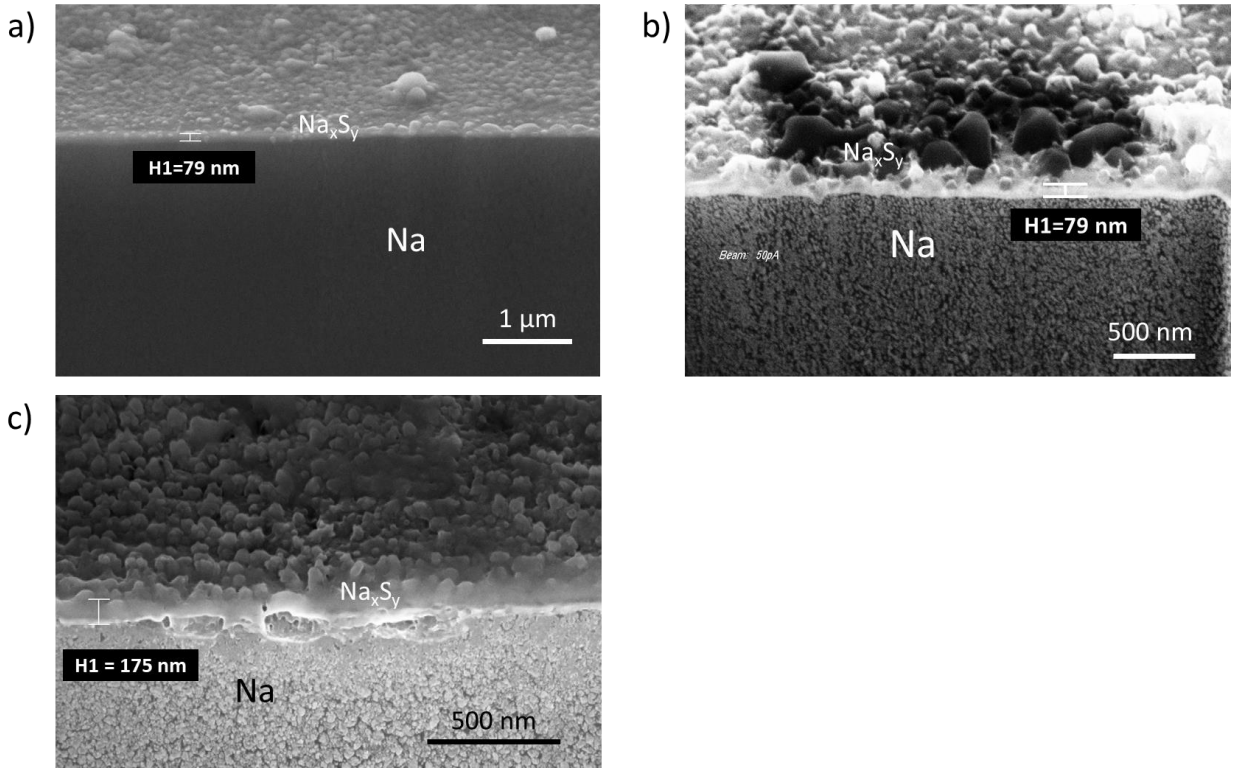

Figure 39. FIB-SEM cross-section images of Na_xS_y on Na synthesized under different temperatures. (a) T_{Na}=60 ˚C, T_S=25 ˚C (b) T_{Na}=T_S=60 ˚C, (c) T_{Na}=T_S=70 ˚C. The synthesis proceeded for 2 hours.

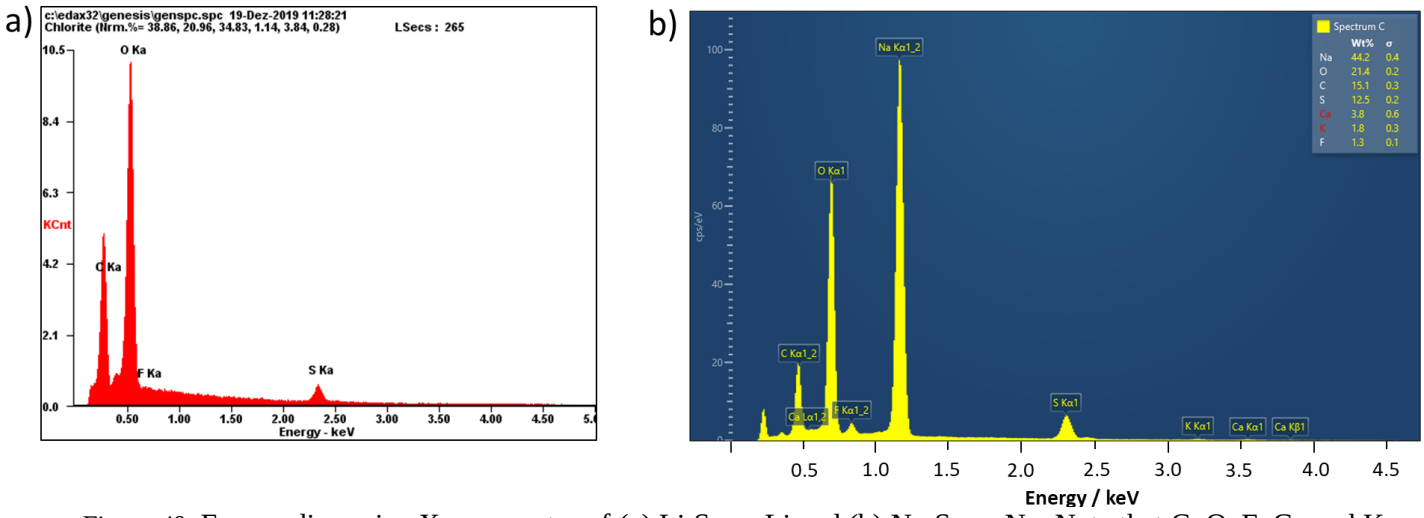

Figure 40. Energy dispersive X-ray spectra of (a) Li_xS_y on Li and (b) Na_xS_y on Na. Note that C, O, F, Ca and K are the common contaminants.

4.1.2. SEI growth behavior in contact with liquid/solid electrolytes under open-circuit condition

The role of the synthesized sulfide-based films (Li_xS_y and Na_xS_y) as artificial SEIs was first tested with EIS in symmetric Li and Na cells with organic liquid electrolytes. Figure 41 shows the electrochemical symmetric cell configuration and the impedance spectra of the cells measured right after the cell assembly and after 24 hours of storage under open-circuit condition. The glyme-based liquid electrolytes are used since they are the commonly employed electrolytes for Li-S and Na-S batteries [163, 164], and triflate salts are chosen as they are reported to be responsible for the SEI resistances, especially for Na [151, 152]. The impedance spectra shows that the SEI resistances decrease over time both for Li and Na, most likely indicating the dissolution of the polysulfide species into the organic liquid electrolyte which have already been observed in Li-S and Na-S batteries. [165, 166] The decrease of SEI resistance with liquid electrolyte in time was also observed for Li_2S synthesized on Li as an artificial SEI. [167] The decrease of SEI resistance appears to be much more significant for Na (650 Ω to 5 Ω), rather than Li (11,000 Ω to 8,500 Ω). This is probably due to that the molar proportion of Na polysulfides in Na_xS_y film is higher than the one of Li polysulfides in Li_xS_y, or because of the simply smaller amount of Na polysulfides compared to Li polysulfides. Another realistic scenario is that the liquid electrolyte infiltrated into the pores (or cracks) of Li_xS_y /Na_xS_y films reacts with the fresh Li/Na metals, forming another SEI, leading to mechanical detachment of the already-existing artificial SEI. If the latter is true, the higher degree of the decrease of SEI resistance in case of Na would indicate that Na_xS_y is more porous than Li_xS_y. This might be realistic, based on the cross-section images measured by FIB-SEM in Figure 37a and d. The highly-concentrated liquid electrolytes (5M LiTFSI in DOL/DME

and 5M NaFSI in DME) were employed to minimize the film dissolution issue and the results are shown in Figure 42. However, the increase of the SEI resistances in all cases implies that the highly-concentrated liquid electrolytes are reactive with Li and Na, rendering a fair comparison between Li_xS_y and Na_xS_y still difficult.

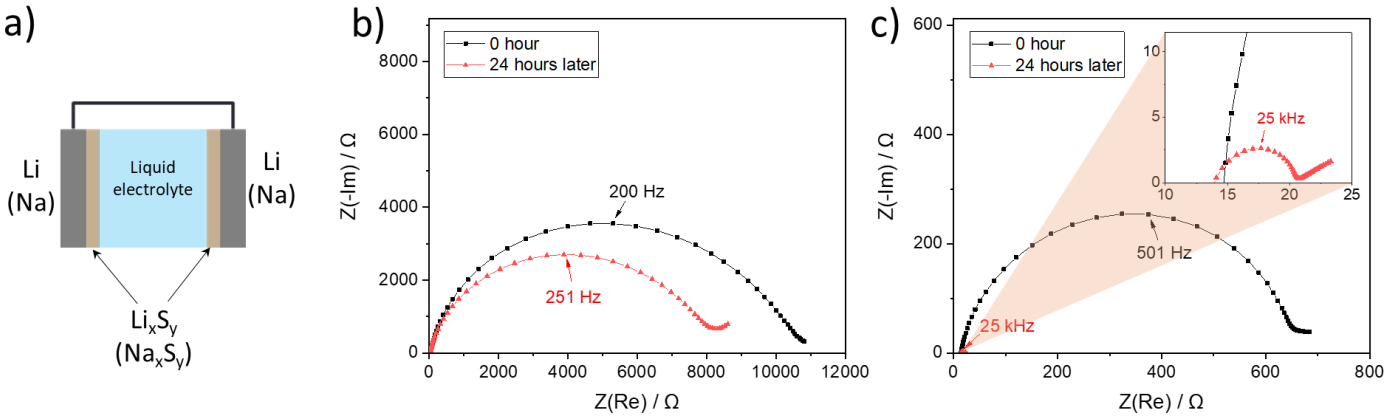

Figure 41. (a) Schematics of the electrochemical measurement cell configuration. (b) Electrochemical impedance result of Li|Li_xS_y|liquid electrolyte|Li_xS_y|Li. (c) Impedance result of Na|Na_xS_y|liquid electrolyte|Na_xS_y|Na. The inset shows the impedance spectrum of the same cell after 24 hours of storage under open-circuit condition.

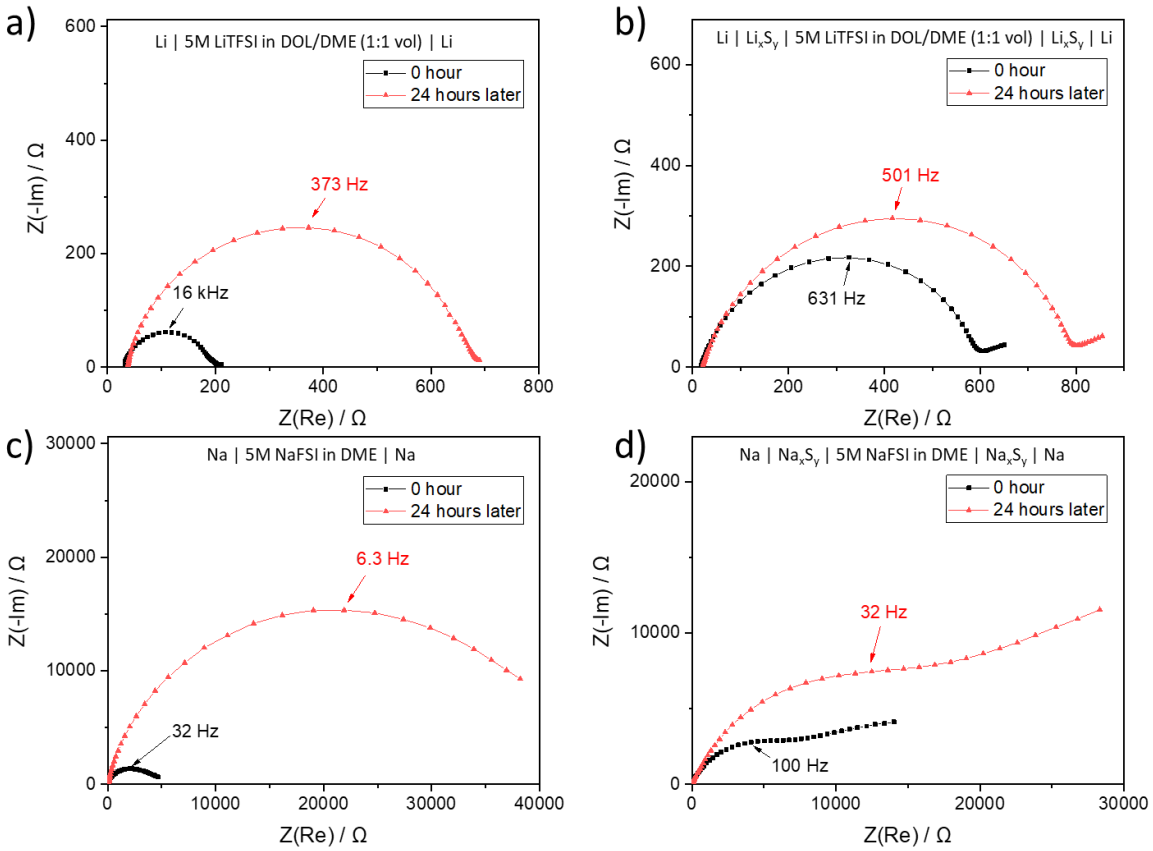

Figure 42. EIS results of (a, b) symmetric Li and (c, d) symmetric Na cells with concentrated organic liquid electrolytes (5M LiTFSI in DOL/DME (1:1 vol) and 5M NaFSI in DME, LiTFSI: Lithium bis(trifluoromethanesulfonyl)imide, DOL: 1,2-dioxolane, DME: dimethoxyethane, NaFSI: Sodium bis(fluorosulfonyl)imide). All electrochemical cells were measured right after the cell assembly (black) and after 24 hours of storage under open-circuit.

In order to avoid the dissolution of polysulfides into the liquid electrolyte, sulfide-based solid electrolytes (Li_3PS_4 and Na_3PS_4) were introduced. Figure 43 shows XRD patterns of the powders and impedance spectra of the pellets of the synthesized solid electrolytes to confirm their crystal structures and ionic conductivities. Li_3PS_4 and Na_3PS_4 have orthorhombic and cubic structures, respectively. Their ionic conductivities are calculated from

$$\sigma = \frac{L}{RA} \tag{4.3}$$

where σ is the ionic conductivity, L is the pellet thickness, R is the resistance of the bulk electrolyte measured by EIS and A is the area of the flat surface of the pellet sample. The pellet was coated with Ru with a thickness of 400 nm on the both sides in the glovebox. The ionic conductivities of the β-Li_3PS_4 and cubic-Na_3PS_4 are measured to be 1.47×10^{-4} S cm^{-1} and 1.55×10^{-6} S cm^{-1}, respectively. The solid electrolytes are assembled in the electrochemical cells with Li/Na electrodes and the impedance was measured over time for 400 hours under the open-circuit conditions (Figure 44 and Figure 45). In case of Li, three distinctive semicircles are observed (Figure 44a and d) while only two semicircles are visible in the Na case (Figure 45a and d). The first semicircles appearing at the highest frequency (>20 kHz) correspond to the ionic transport in the bulk solid electrolytes as confirmed from the previous EIS measurements with the blocking Ru electrode in Figure 43b and d. The second semicircles at the medium frequency (10~20 kHz for Li and 0.01 ~3 kHz for Na) are from the interfaces between the alkali metals and solid electrolytes, as their values continuously change over time. The interfacial change is most likely attributable to the continuous chemical reactions between the alkali metals and the solid electrolytes as follows. [168, 169]

$$8Li + Li_3PS_4 \rightarrow Li_3P + 4Li_2S \qquad \Delta_r G^\circ < 0 \tag{4.4}$$

$$8Na + Na_3PS_4 \rightarrow Na_3P + 4Na_2S \qquad \Delta_r G^\circ < 0 \quad (4.5)$$

The origin of the smallest semicircle for the Li case at lowest frequency (<10 Hz) is not proven yet, but it is believed to originate from either imperfect solid contacts or concentration polarization within the mix-conducting phase. Figure 46 shows the equivalent circuit models for fitting the impedance spectra in the Figure 44 and Figure 45. The interfacial resistances ($R_{interface}$) and interfacial capacitances ($C_{interface}$) derived by fitting with the equivalent circuit models and their evolutions over time are shown in Figure 44 and Figure 45. In the case of Li, the $R_{interface}$ trend of the two Li systems with and without Li_xS_y is opposite; $R_{interface}$ decreases over time in the cell without Li_xS_y, while it increases in the cell with Li_xS_y. The decrease of $R_{interface}$ is unexpected since the reaction products are predominantly resistive (molar ratio of Li_3P and Li_2S=1:4, $\sigma(Li_2S)\sim10^{-11}$ S cm^{-1} [22], $\sigma(Li_3P)\sim10^{-4}$ S cm^{-1} [170]). This may attributable to the i) Li creep through the SEI, or ii) rearrangement of the phases such a way to that the contact to each other is improved. Both might have been caused by the mechanical pressure built up in the electrochemical cell or by capillary pressure. [171] The former seems to be likely since the reaction products have smaller molar volumes compared to the reactants ($R_{PB} = \frac{V_{Li3P}+4V_{Li2S}}{8V_{Li}+V_{Li3PS4}} = 0.72$), meaning that the formed SEI is porous which then provides the space for Li penetration. The latter is also realistic considering the fact that Li_3P is suspected to have partial electronic conductivity [172], which would drive the chemical diffusion of Li, resulting in the continuous chemical reaction. Another Li symmetric cell with Li_xS_y shows $R_{interface}$ increase over time. This may have been caused by the i) formation of resistive phases (Li_2S and LiOH) from the chemical reaction between protruded Li and polysulfides/residual water on the surface of Li_xS_y, or ii) further SEI formation reaction. In any case, the increase of $R_{interface}$ clearly suggests that the artificial SEI is not completely protective. E_a(interface) provides hints of major ionic transport pathways, and the values are 0.54~0.58 eV.

Considering the activation energy values of electrical transport in Li_3P (0.44 eV [170]) and Li_2S (0.90 eV [22]), it is most probable that the electrical conduction is contributed by both phases. The interfacial capacitance values could provide a clue about the morphology of the interfaces. The $C_{interface}$ of the Li cell with Li_xS_y is on the order of 10^{-9} F (Figure 44f), which is in good agreement with the calculated capacitance when the thickness of Li_xS_y is taken from the FIB-SEM cross-section image (Figure 37a) and dielectric constant is assumed to be 10. [22] The cell with bare Li without Li_xS_y exhibits $C_{interface}$ values of ~10^{-8} F, implying that the formed SEI in this case is much thinner than the one with Li_xS_y. This can be supported by the previous literature where a very thin SEI with FIB-SEM has been observed at the interface between Li and Li_3PS_4. [173]

In the Na cases severe changes of $R_{interface}$ are observed compared to Li cases as shown in Figure 45. The general trends of $R_{interface}$ changes in Na symmetric cells are similar in both cases (i.e. with and without Na_xS_y), which also suggests that the Na_xS_y is not a protective layer. The increase of $R_{interface}$ (Na|Na_3PS_4) has already been observed in the literature [171, 174], which is most likely attributable to the fact that i) R_{PB} smaller than 1 ($R_{PB} = \frac{V_{Na3P}+4V_{Na2S}}{8V_{Na}+V_{Na3PS4}} = 0.76$) allows Na creep into the pores, leading to another chemical reaction, or ii) Na_3P is a partially electron-conducting materials. [174-176] Here, the possibility of metal creep is considered in both Li and Na cases, but whether the metal creep results in the $R_{interface}$ increase or decrease needs to be carefully investigated in the future by taking into account the mechanical properties and reactivity of Li/Na. The interfacial capacitance evolution behavior is different for Na with and without Na_xS_y films. $C_{interface}$ in a symmetric Na without Na_xS_y is on the order of 10^{-10} F and remains constant over time. On the contrary, in the case with Na_xS_y, $C_{interface}$ gradually increases to ~10^{-8} F and converges. The increase of capacitance implies that either the contact area increased or the thickness decreased. The interfacial thickness decrease is very unlikely, as the chemical reaction

proceeds continuously. The area increase could have achieved by filling the pores in Na_xS_y by the reaction products, which contributes to the capacitance in a parallel way. The activation energy values are different in those two cases (with and without Na_xS_y); the one with Na_xS_y has higher E_a (0.87 eV) compared to the one without Na_xS_y (0.65 eV). This may be attributable to the fact that the i) Na polysulfide species have inherently higher E_a compared to Na_2S, or ii) porous Na_xS_y layer makes the electrical conduction more difficult compared to the SEI formed on bare Na.

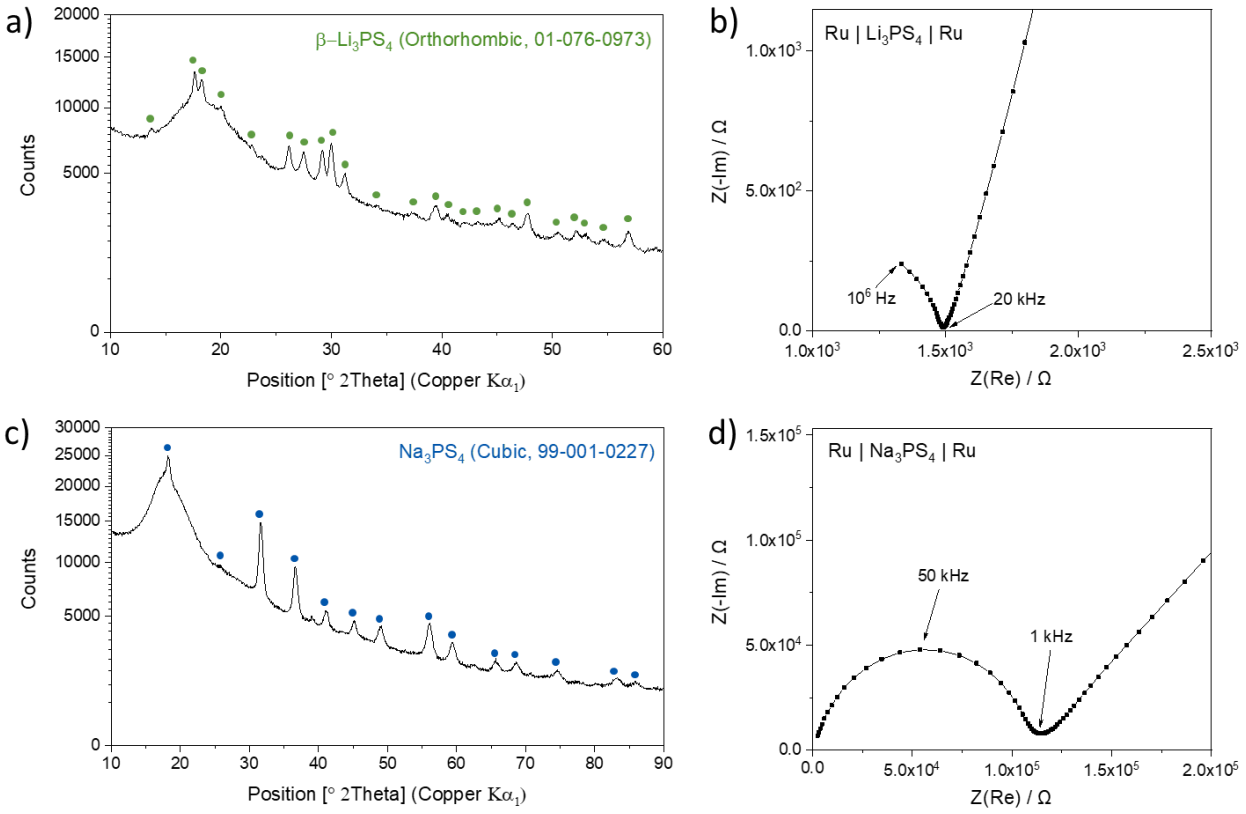

Figure 43. (a, c) X-ray diffraction patterns and (b, d) impedance results of synthesized β-Li_3PS_4 and cubic-Na_3PS_4. For the ion conductivity measurements, Ru was sputtered on both sides of the dense solid electrolyte pellets. All procedure of synthesis, sputtering and measurements were performed under Ar.

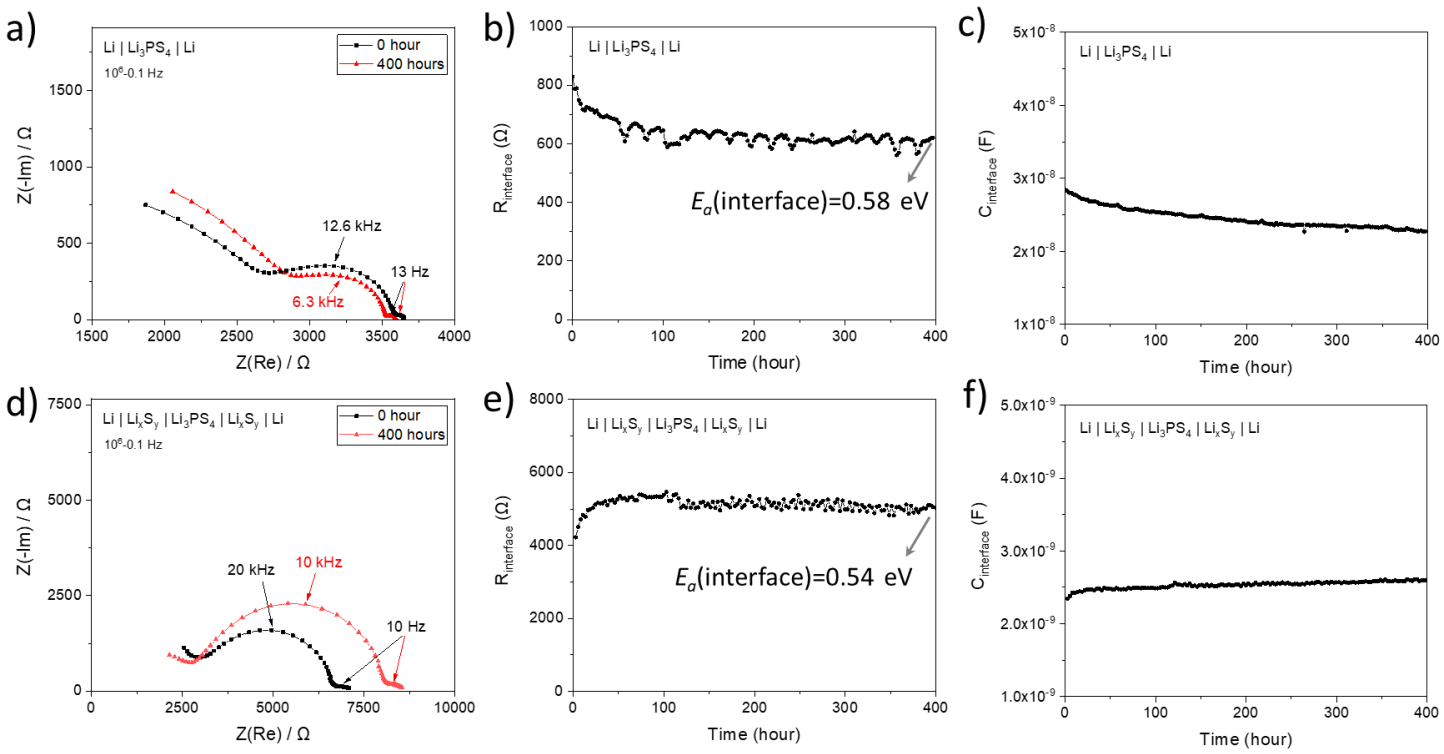

Figure 44. (a, d) Impedance spectra of Li|Li_3PS_4|Li and Li|Li_xS_y|Li_3PS_4|Li_xS_y|Li over aging under open-circuit condition. (b, e) $R_{interface}$ and (c, f) $C_{interface}$ evolution over time corresponding to (a, d).

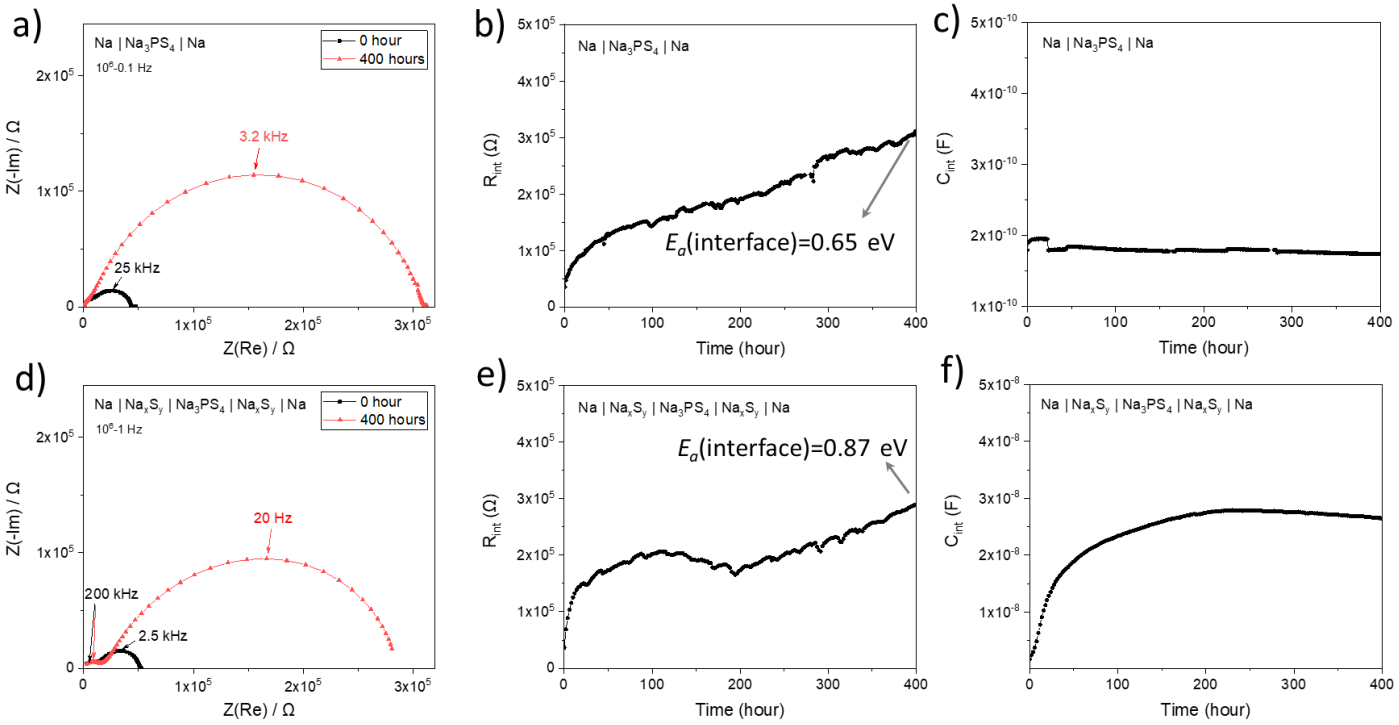

Figure 45. (a, d) Impedance spectra of Na|Na_3PS_4|Na and Na|Na_xS_y|Na_3PS_4|Na_xS_y|Na over aging under open-circuit condition. (b, e) $R_{interface}$ and (c, f) $C_{interface}$ evolution over time corresponding to (a, d).

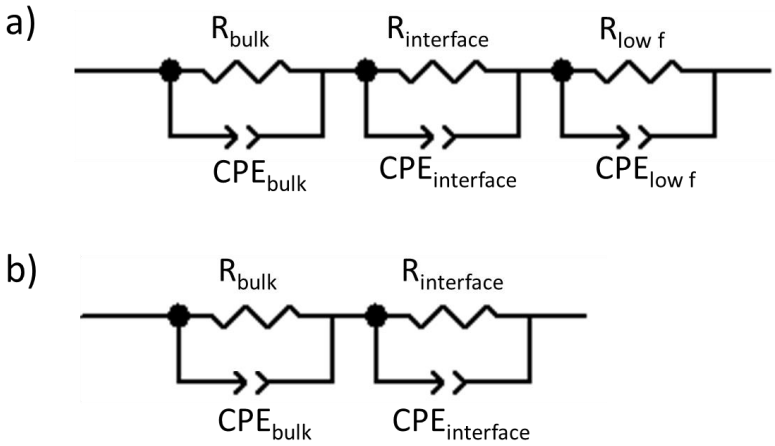

Figure 46. Equivalent circuit models for fitting impedance spectra of (a) Li symmetric cells with Li_3PS_4 (in Figure 44) and (b) Na symmetric cells with Na_3PS_4(in Figure 45). CPE: constant phase element. R_{bulk} and CPE_{bulk} correspond to bulk solid electrolyte appearing at high frequency (>20 kHz), and $R_{interface}$ and $CPE_{interface}$ correspond to interface (SEI). $R_{low\ f}$ and $CPE_{low\ f}$ are resistance and constant phase element appearing at low frequency (< 10 Hz) in Li symmetric cells with Li_3PS_4.

4.1.3. Performance in all-solid-state batteries: Stripping-plating results

The practical feasibility of the synthesized artificial SEIs (Li_xS_y and Na_xS_y) for the battery application is assessed by galvanostatic stripping-plating where the constant current (0.01 mA cm^{-2}) is applied. Four different systems are compared: two Li symmetric cells with and without Li_xS_y and two Na symmetric cells with and without Na_xS_y. The results are shown in Figure 47. For Li case, Li_xS_y induces higher overpotential compared to the bare Li, which is consistent with the impedance measurements in Figure 44. Such overpotential appears to be higher at the very first stage of stripping-plating (~0.05 V), and decreases afterwards to ~0.04 V, implying that the nucleation energy barrier is increased. A remarkable fact is that both Li cells with and without Li_xS_y exhibit stable galvanostatic cycling without significant increase of overpotential upon cycling, and this indicates that both the spontaneously formed SEI and artificial SEI act as protective layers in a chemo-mechanical sense for a given current density (0.01 mA cm^{-2}). In case of Na, two Na cells show similar galvanostatic cycling behavior in terms of the overpotential and its increase degree upon the cycling, which is also in agreement with the impedance analysis in Figure 45. Additionally, the similar SEI growth behavior in two systems implies that the artificial SEI does not play any role on the acceleration or hindrance of the SEI growth. The closer look at the stripping-plating behavior shows the gradual increase of overpotential in each cycle, implying that the Na diffusion is a rate-limiting step, rather than Na nucleation. [177-179]

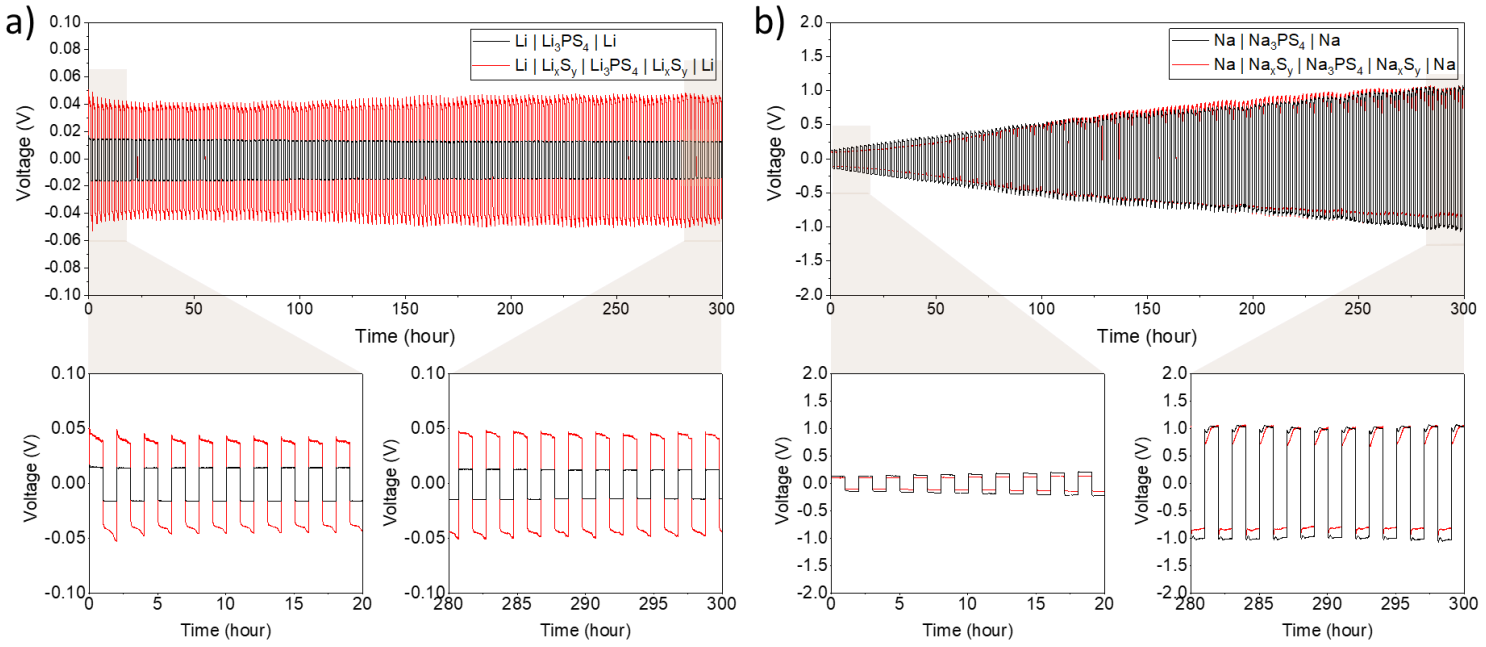

Figure 47. Stripping-plating behavior of (a) symmetric Li cells and (b) symmetric Na cells with (red) and without (black) artificial sulfide-based SEIs (i.e. Li_xS_y and Na_xS_y). The applied current is 0.01 mA cm^{-2}. Below each graph, the stripping-plating behavior of the first 20 hours and the last 20 hours are displayed.

4.2. Al_2O_3 SEIs formed by atomic layer deposition

4.2.1. Electrochemical impedance spectroscopy of symmetric Al_2O_3-Li/Na cells with liquid electrolytes

Synthetic procedure of Al_2O_3 is described in detail in the experimental section. It has already been reported that Al_2O_3 was synthesized with atomic layer deposition on Li [98] and Na [180], but neither the SEI resistance evolution over time nor the ion transport in the Al_2O_3 has not been investigated in detail.

Al_2O_3 was synthesized on Li and Na with different nominal thicknesses (1, 2.5, 5 and 10 nm) and symmetric Li/Na cells were assembled with glyme-based liquid electrolytes (1M LiTf in triglyme and 1M NaTf in triglyme). The electrochemical cells were measured with EIS under open-circuit potential and then the activation energy of transport in the SEI (E_a(SEI)) was measured by varying the temperature. Figure 48 shows the SEI resistance change over 12 hours where the increase of SEI resistances are observed in all cases of Li symmetric cells with different Al_2O_3 thicknesses. In case of 1 nm-thick-Al_2O_3, the SEI growth behavior may be driven by electron tunneling [181], but this is less likely to happen in thicker Al_2O_3 films. Furthermore, the SEI resistance values are in the order of several thousand Ω, even though Al_2O_3 is known to be blocking for both electrons and ions. [182, 183] These facts strongly suggest that either Al_2O_3 does not completely cover the Li surface (i.e. is porous), or the Al_2O_3 layer is partially broken in the course of the cell assembly. Figure 49 shows the E_a(SEI) values measured after 12 hours of cell storage under open-circuit potential, and the values are in the range of 0.8~0.9 eV. This indicates that the SEIs formed in the cracks (or pores) of the Al_2O_3 is densified more quickly compared to the one formed by the contact between bare Li and the liquid electrolyte (Figure 15). This is most likely

due to the fact that a space for SEI formation is constrained by the surrounding Al_2O_3 layer. Thus, the equivalent circuit model for the porous SEI in part 3.3 is not applicable to this system. The general trend among the different Al_2O_3 thicknesses is that the SEI resistance becomes bigger when Al_2O_3 gets thicker. This implies that the more pores (or cracks) are formed as the Al_2O_3 becomes thinner.

The same procedure (Al_2O_3 synthesis and EIS measurements) was performed on Na and the results are shown in Figure 50 and Figure 51. However, since the Na metal itself is much more reactive than Li, Na oxides and hydroxides form before inserting the Na metals into the ALD reaction chamber for the Al_2O_3 synthesis. Given by the previous observation that the Na oxides and hydroxides are porous (Figure 9), it is likely that the Al_2O_3 layer is not deposited on the whole surface (including pores) of Na. This results in the continuous chemical reaction between the non-covered parts of Na and the liquid electrolytes, leading to the increase of SEI resistances (Figure 50) and E_a(SEI) values being between liquid electrolytes and solid SEI compounds (Figure 51). Therefore, Al_2O_3 on Na is not investigated further.

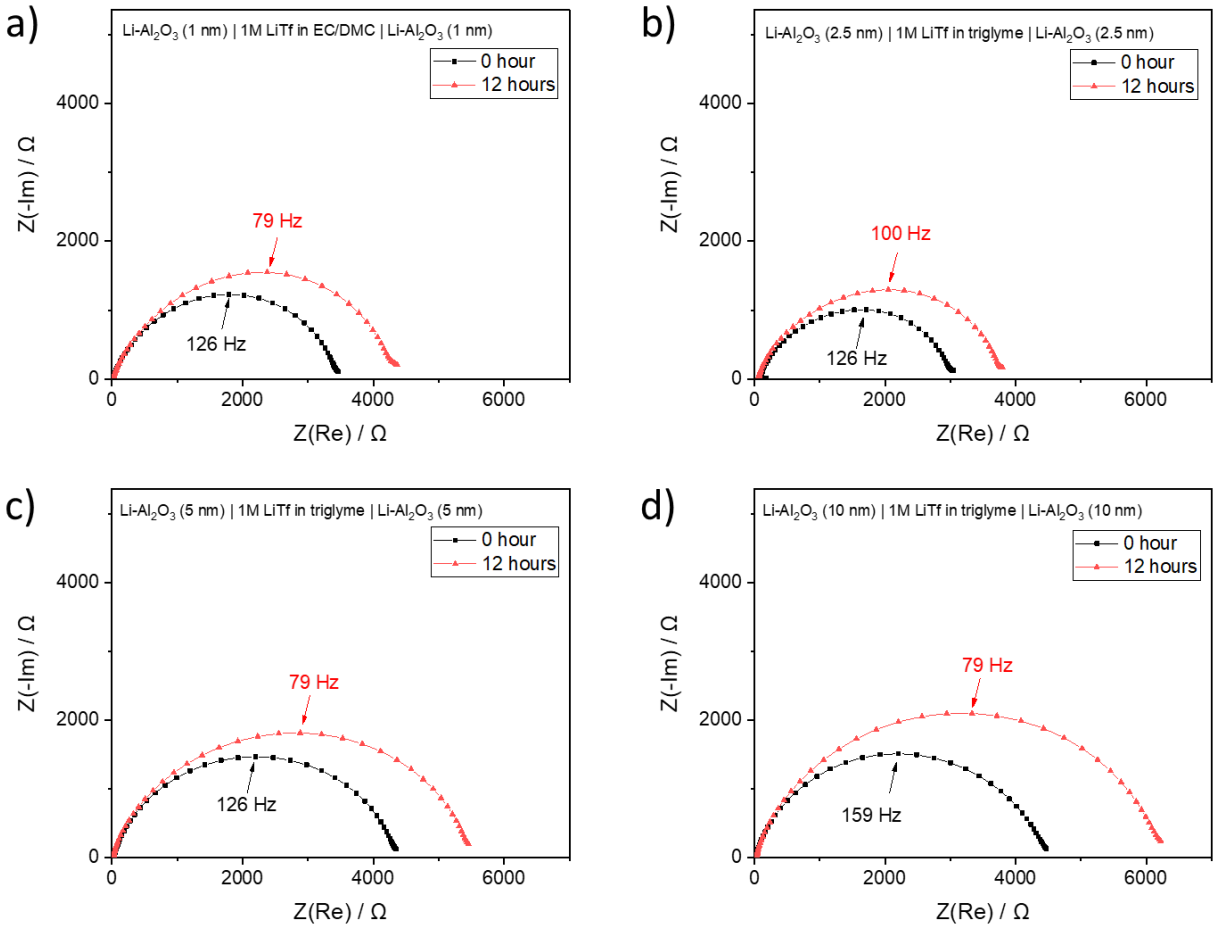

Figure 48. Impedance spectra of symmetric Li cells containing glyme-based liquid electrolyte (1M LiTf in triglyme) with (a) 1 nm, (b) 2.5 nm, (c) 5 nm and (d) 10 nm of Al_2O_3.

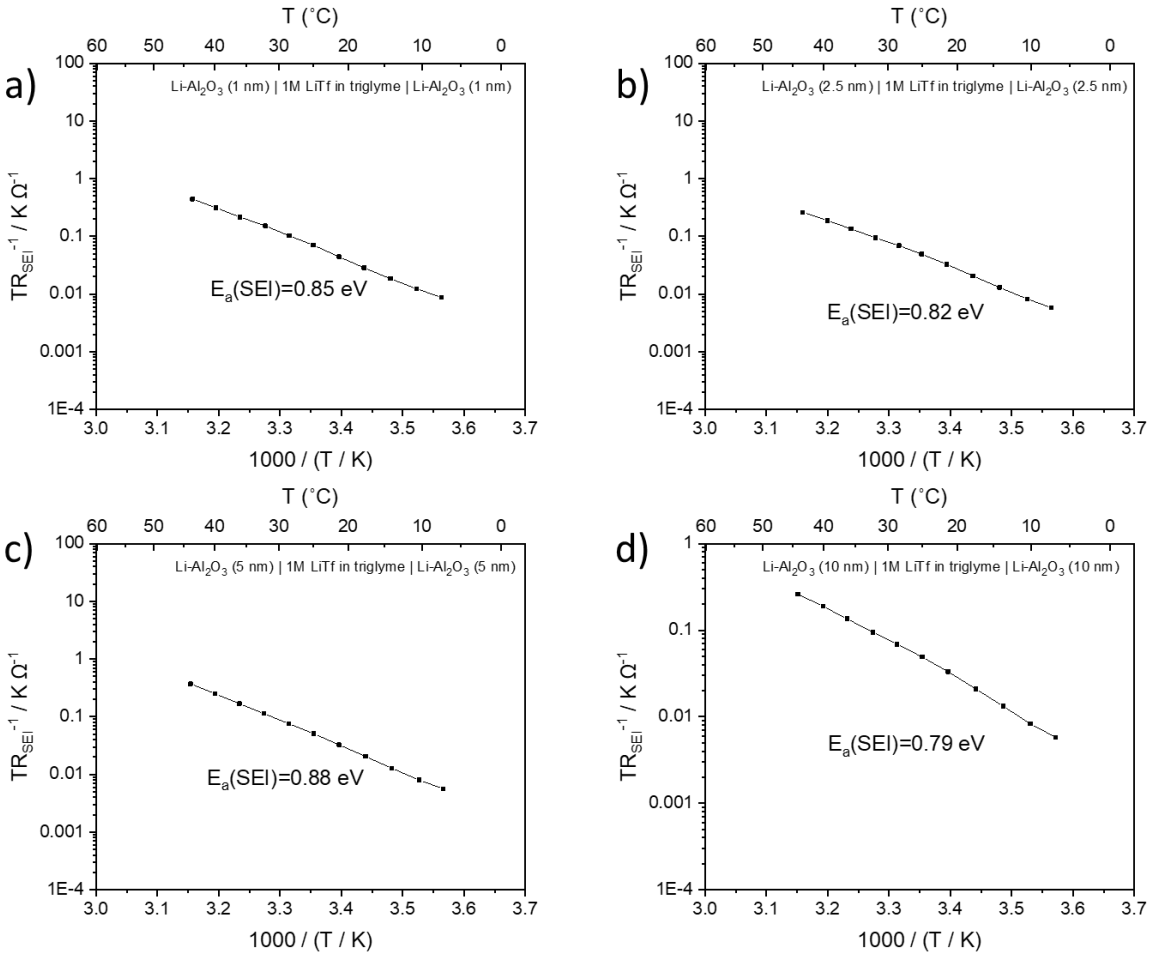

Figure 49. Arrhenius plots of Li symmetric cells containing glyme-based liquid electrolyte (1M LiTf in triglyme) with (a) 1 nm, (b) 2.5 nm, (c) 5 nm and (d) 10 nm of Al_2O_3. Activation energy of transport in SEI is stated.

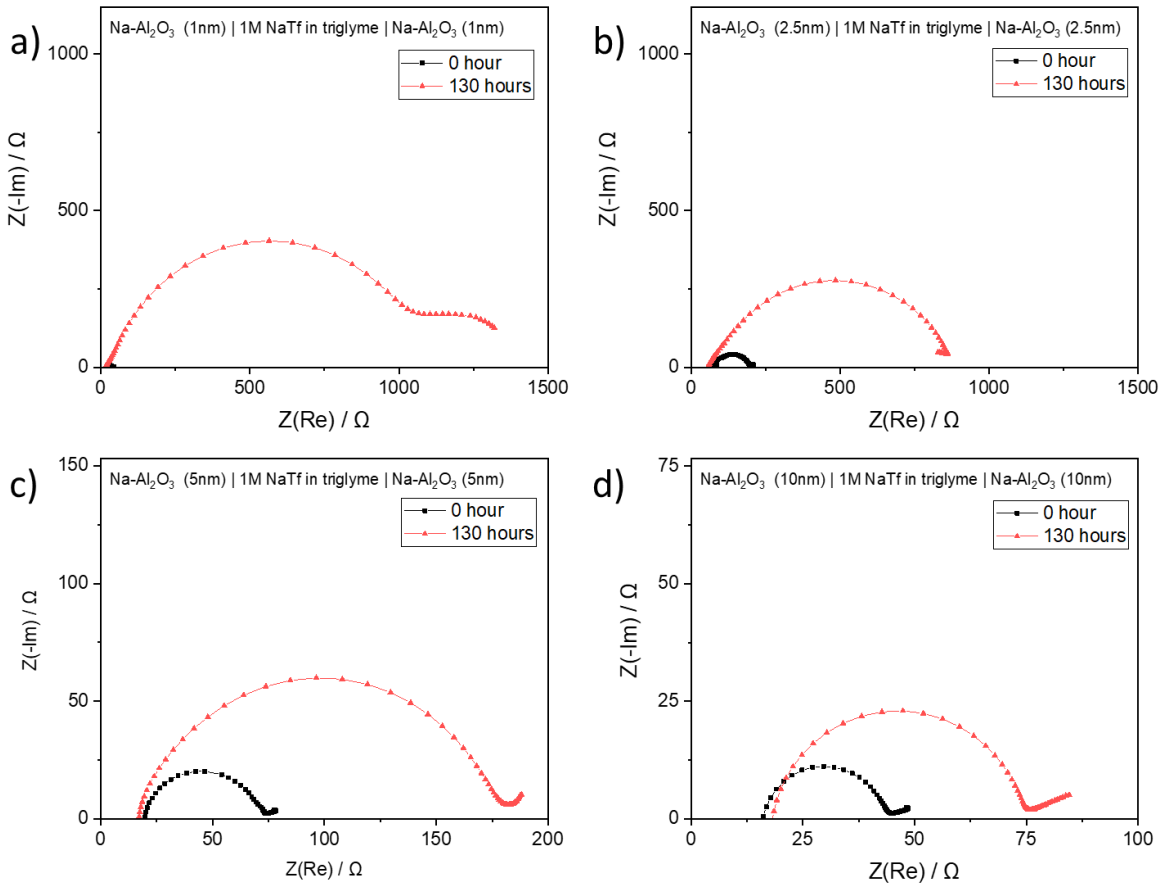

Figure 50. Impedance spectra of symmetric Na cells containing glyme-based liquid electrolyte (1M NaTf in triglyme) with (a) 1 nm, (b) 2.5 nm, (c) 5 nm and (d) 10 nm of Al_2O_3.

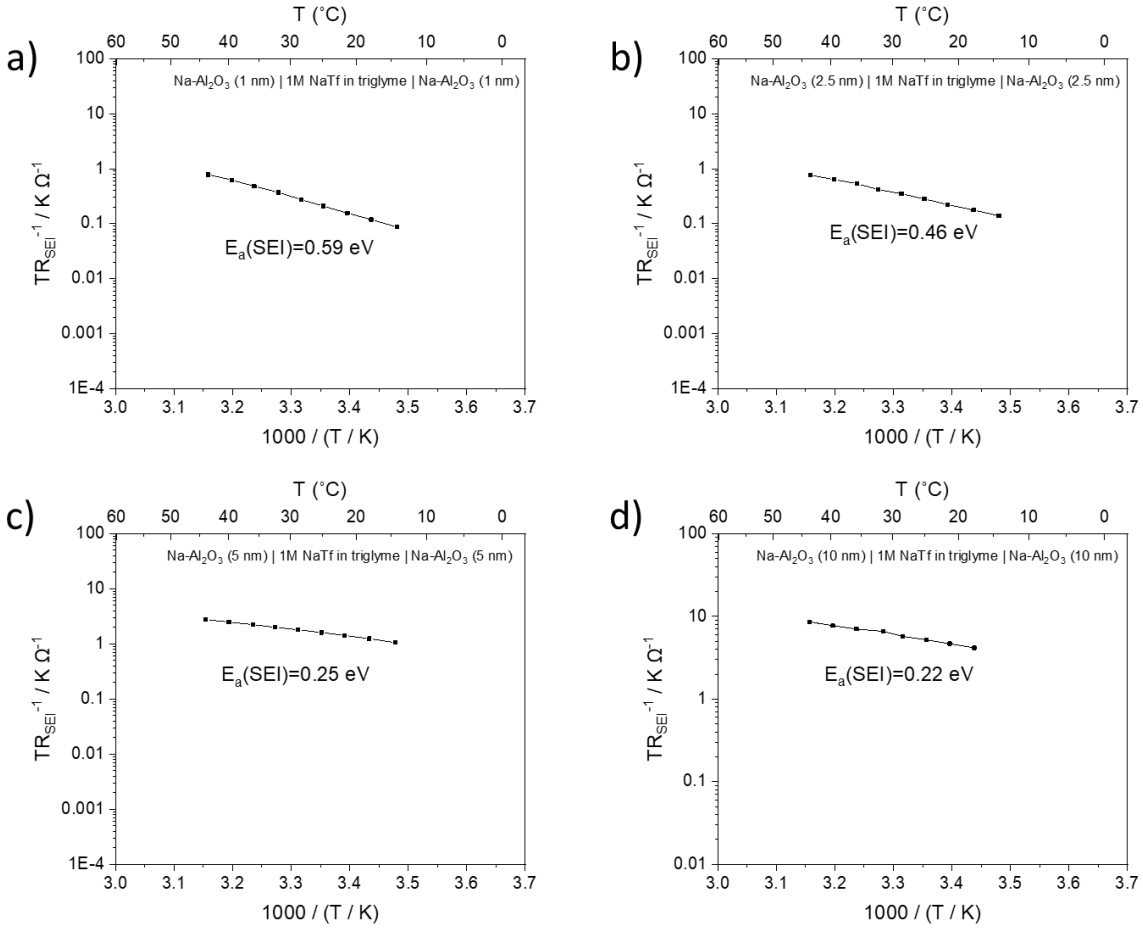

Figure 51. Arrhenius plots of Na symmetric cells containing glyme-based liquid electrolyte (1M NaTf in triglyme) with (a) 1 nm, (b) 2.5 nm, (c) 5 nm and (d) 10 nm of Al_2O_3. Activation energy of transport in SEI is stated.

4.2.2. Morphological and chemical characterization of Al_2O_3 on Li

Figure 52 shows cross-section images of Al_2O_3-deposited-Li before and after contacting liquid electrolyte (1M LiTf in triglyme). The film thicknesses appear to increase after contacting the Al_2O_3-deposited-Li with liquid electrolyte. Also, EDX mapping results in Figure 53 and Figure 54 show that the signals from O, F, C and S become stronger when it was contacted to liquid electrolyte, implying the chemical reaction occurred between Li and the liquid electrolyte. These signals appear to be stronger in grain boundaries, meaning that the grain boundary region is not completely covered by Al_2O_3 layer.

Figure 55 and Figure 56 show XPS results on 10 nm-Al_2O_3-coated Li before and after contacting the liquid electrolyte. In the case of bare 10 nm-Al_2O_3-coated Li, the surface of the Al_2O_3 is covered with small amounts of Li carbonates and compounds with O-C=O bonding. As the sample is sputtered, the Li peaks (both oxidized and metallic Li) appear along with small amount of oxides, carbonates and carbon contaminants (C-C, C-H). The origin of the peaks at approximately 72 eV and 75 eV (Al 2p) are not fully clear yet, but they may originate from the metallic Al or ternary phase of Al-O-Li. [184] If the latter is true, the pores (or cracks) of Al_2O_3 would have been caused by the formation of the new phase. XPS results of 10 nm-Al_2O_3-coated Li after contacting the liquid electrolyte in Figure 56 shows the presence of Al-O bonding and other peaks are similar with the ones observed in the SEI on Li formed by the contact with the same liquid electrolyte used here (Figure 20 and Figure 21). The morphological/chemical characterization strongly support the claim that Al_2O_3 layer is porous (or has cracks), which allows the liquid infiltration into the layer, forming additional SEIs in the pores.

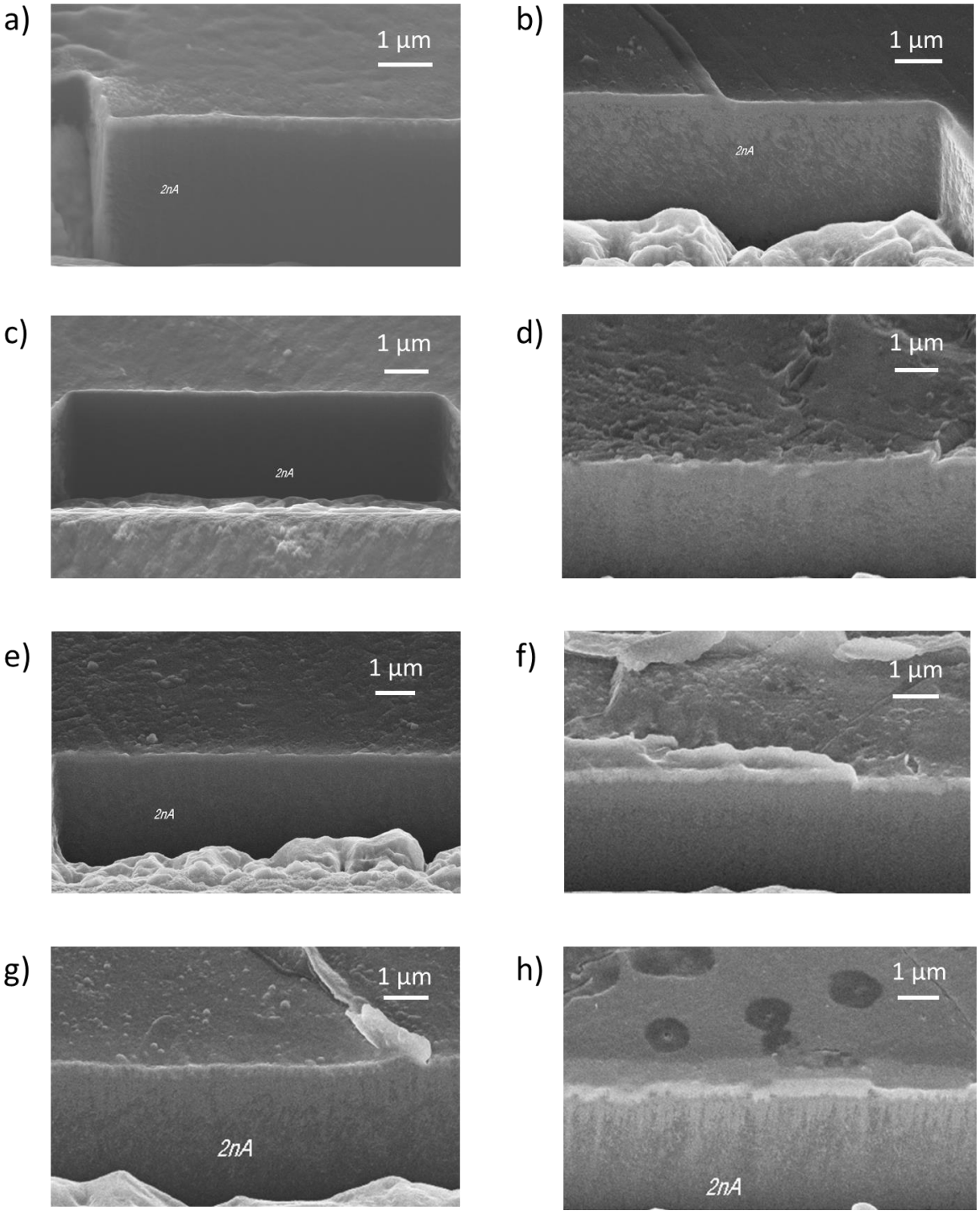

Figure 52. FIB-SEM cross-section images of Li with Al_2O_3 on top (a, c, e, g) before contacting liquid electrolyte (1M LiTf in triglyme) and (b, d, f, h) after contacting liquid electrolyte for 12 hours. (a, b) 1nm (c, d) 2.5 nm, (e, f) 5 nm and (g, h) 10 nm of Al_2O_3.

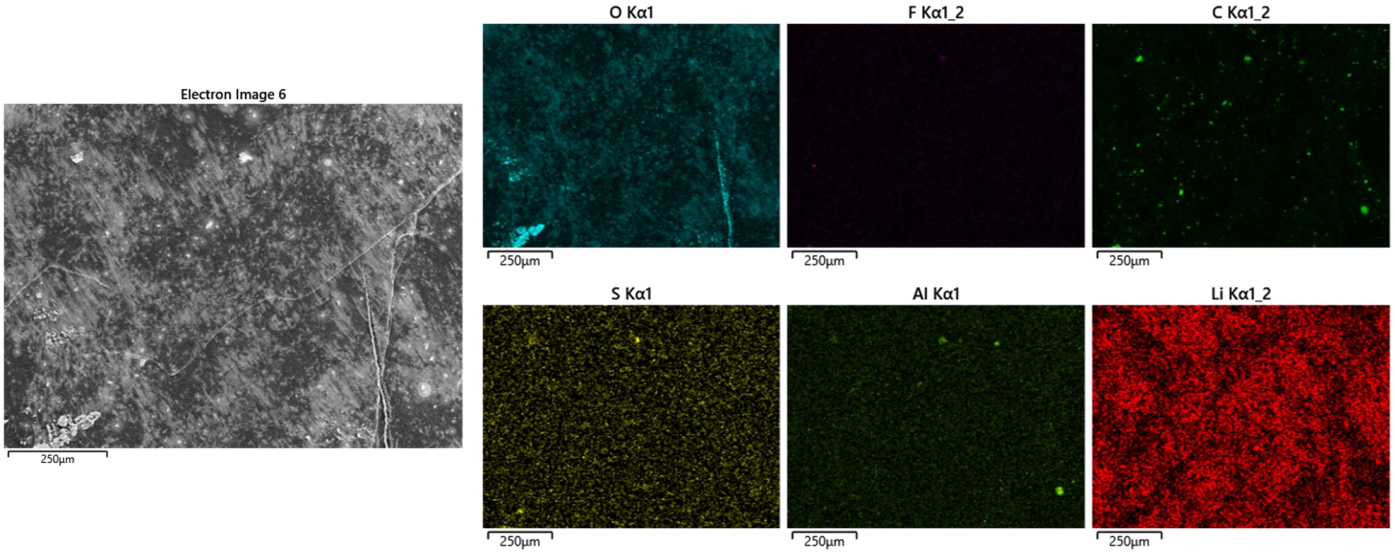

Figure 53. EDX mapping results of Li with 10 nm-Al_2O_3 before contacting to the liquid electrolyte.

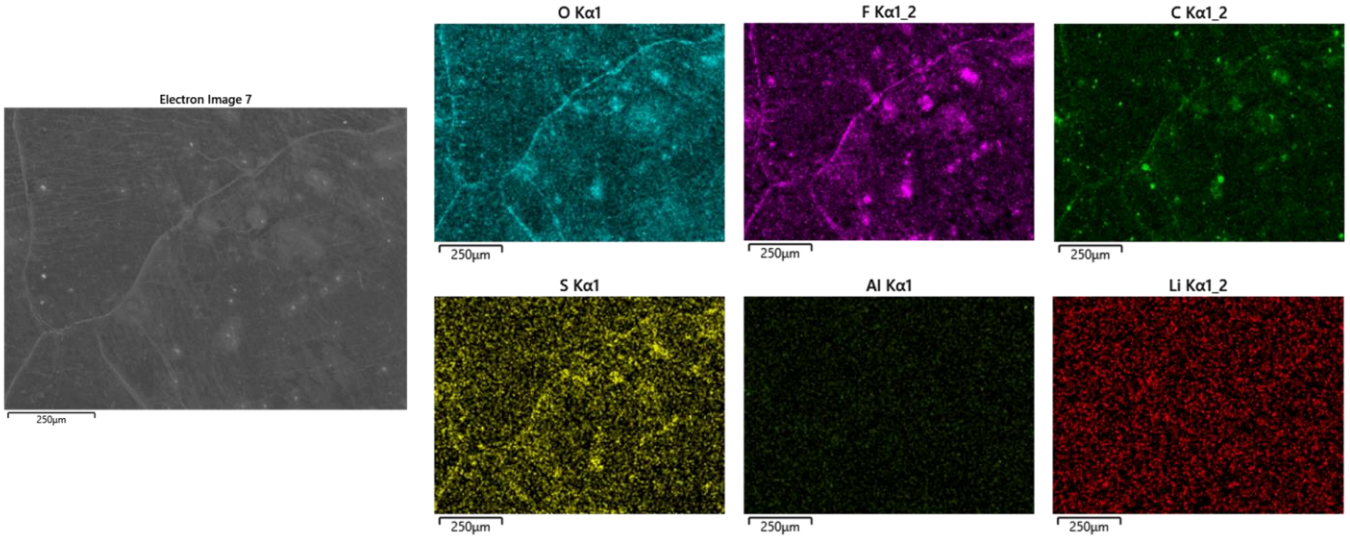

Figure 54. EDX mapping results of Li with 10 nm-Al_2O_3 after contacting to the liquid electrolyte for 12 hours.

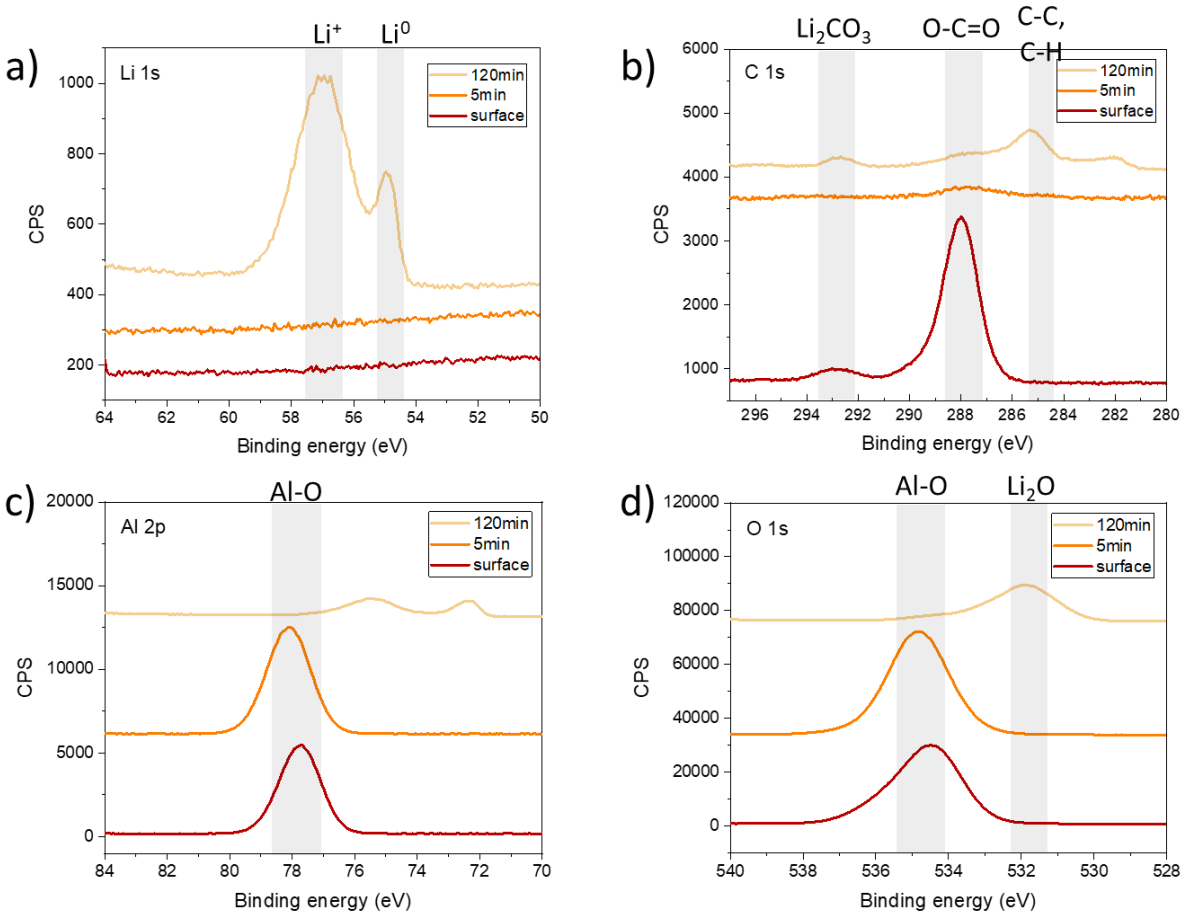

Figure 55. XPS results of 10 nm-Al_2O_3-coated Li.

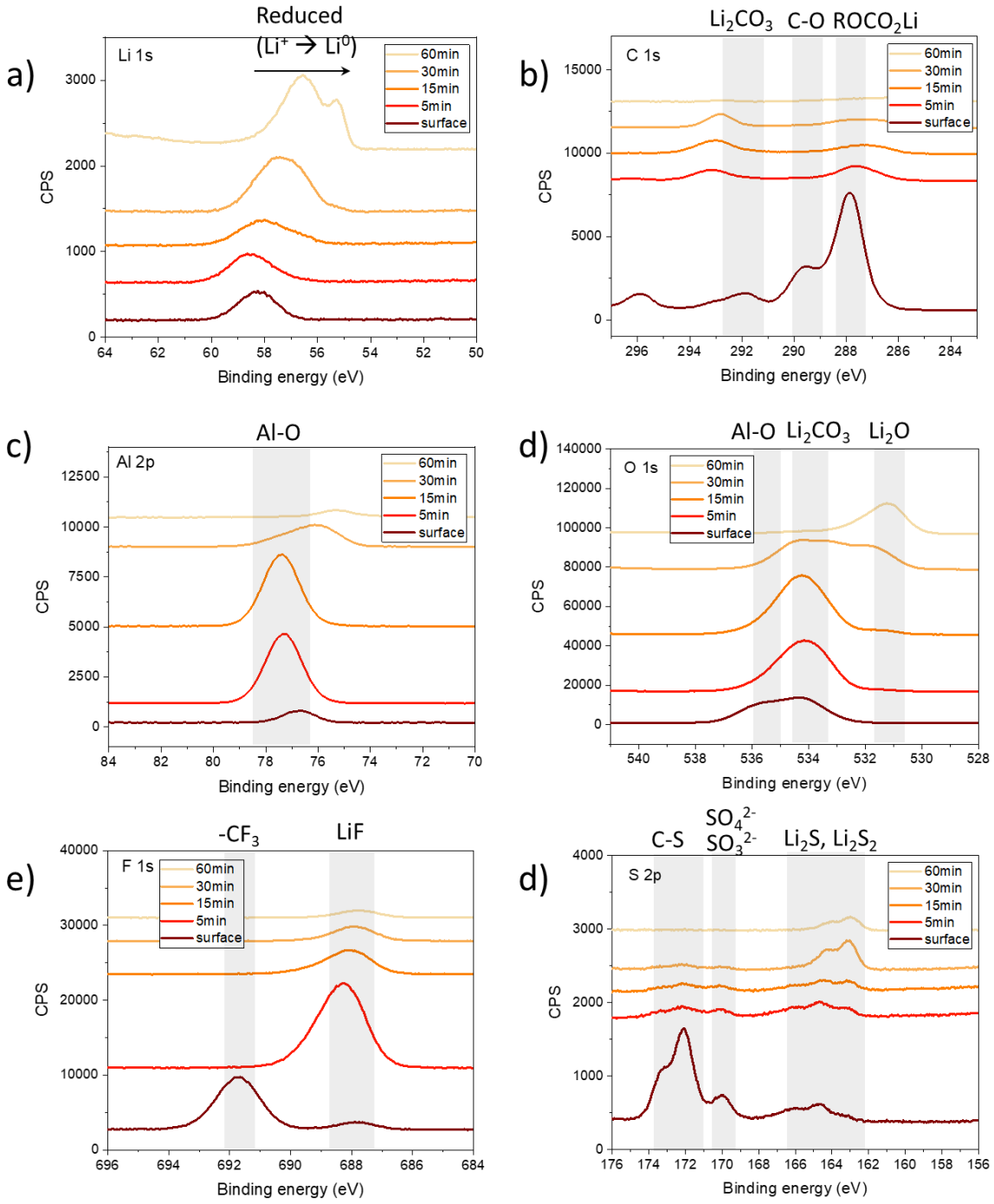

Figure 56. XPS results of 10 nm-Al_2O_3-coated Li contacted with 1M LiTf in triglyme for 12 hours under open-circuit potential.

4.3. Conclusion

In this chapter, SEIs formed artificially on Li and Na before the electrochemical cell assembly are investigated with electrochemical measurements and morphological/chemical characterization tools. Two types of artificial SEIs are tested, namely the sulfide-based SEIs and Al_2O_3.

First, sulfide-based SEIs are synthesized on the surface of Li and Na by chemical reaction between Li/Na and S vapor. The artificial sulfide-based SEIs are found to be composed of Li_2S/Na_2S in the bulk and polysulfides/sulfites/sulfates near the surface, indicating the concentration gradient formed over the depth. Na_xS_y is observed to be more porous and rough compared to Li_xS_y, which is most likely attributable to the difference of Pilling-Bedworth ratios in two Li/Na sulfide phases ($R_{PB}(Li_2S)$ = 1.06, $R_{PB}(Na_2S)$ = 0.89, $R_{PB}(Na_2S_2)$ = 1.16, $R_{PB}(Na_2S_4)$ = 1.79, and $R_{PB}(Na_2S_5)$ = 2.17). The electrochemical measurements with liquid electrolytes show dissolution of sulfide-based SEIs, thus sulfide solid electrolytes (Li_3PS_4 and Na_3PS_4) are synthesized and tested with Li and Na as all-solid-state electrochemical cells. The results suggest that sulfide-based SEIs do not provide advantages in terms of the stability over time and overpotential during stripping-plating, which is most likely owing to the porosity of the sulfide-based artificial SEIs.

Second, Al_2O_3 are deposited on the surface of Li and Na with atomic layer deposition. Al_2O_3 itself is blocking for both ion and electron, but the electrochemical measurement show that Al_2O_3 is also porous which induces liquid electrolyte infiltration into the pores and forming additional SEIs in the pores. The morphological and chemical characterization proves the formation of additional SEIs, supporting the fact that Al_2O_3 is porous. A successful application of Al_2O_3 as an artificial SEI would imply a variety of SEI phases formed in the pores.

5. Summary, conclusion and outlook

The present thesis deals with the ionic transport and growth behavior of the Li and Na SEIs, the ones which are spontaneously formed by the chemical reaction between alkali metals and the other ones that are artificially formed before assembling the electrochemical cells, with the liquid and solid electrolytes. The investigation of SEIs on Li and Na are challenging due to their fragility and reactivity. Thus, the ion transport in the SEIs is carefully studied by measuring activation energies at temperature below the room temperature. Impedance modeling is conducted in parallel based on the activation energies in order to have more insights into the transport and growth mechanism of SEIs. The morphological/chemical characterization was carried out with vacuum transfer tools to avoid sample exposure to the ambient air, and the results are interpreted along with the electrochemical results.

In the first part, Li and Na symmetric cells with glyme- and carbonate-based liquid electrolytes are assembled to examine the spontaneously-formed SEIs on Li and Na. Activation energies of ion transport in the SEI suggest that the SEIs are partially porous and become densified over storage under open-circuit potential. The SEIs on Na are proved to be more porous compared to the ones on Li, which is most likely attributable to the fact that the Na SEI compounds have lower molar volumes than Na. Additionally, equivalent circuit model is provided based on the activation energies and the measured frequency range of the EIS, where the resistance is majorly contributed by the liquid channel (in reality pores) and the capacitance mostly stems from the bulk part of the SEIs.

The second part introduces two different types of artificial SEIs: sulfide-based SEIs made by chemical vapor reaction and Al_2O_3 synthesized by the atomic layer deposition. These systems can

be the two different model systems of the SEI, since Li_2S and Na_2S are ionic conductors and electronic insulators, and Al_2O_3 is blocking for both ions and electrons. Sulfide-based SEIs are shown to be composed of not only Li_2S and Na_2S, but also polysulfides and other sulfur-related compounds such as sulfates and sulfites. Electrochemical tests on symmetric Li/Na cells with artificial SEIs in combination with liquid/solid electrolytes show that the artificial SEIs are not beneficial in terms of stability over time and SEI resistance. This is ascribed to the pores of the SEIs, which act as channels for liquid electrolyte infiltration, a space for Li/Na metal creep, or just completely blocking part for ion/electron conduction. Al_2O_3-coated-Li is assessed by assembling symmetric cells with the liquid electrolytes, and the electrochemical/morphological/chemical results confirm the porosity of the Al_2O_3 layer. The liquid electrolyte infiltrates into the pores and SEIs are formed in the pores, but in this case SEIs become densified more quickly compared to the SEIs formed on the bare Li.

To summarize, the porosity of the SEIs is discussed not only for the ones spontaneously formed but also for the ones artificially prepared. In all cases, pores in the SEIs play critical roles in the ionic transport as well as in the SEI growth behavior, especially with liquid electrolytes that can infiltrate into the pores. The SEI pores were not discussed frequently in the literature, but in the present thesis, the porosity is emphasized for investigating the ion transport and growth of the SEIs. The pores are considered to be nano-sized as they are not clearly observable with SEM, so further examination with cryo-TEM would achieve the better understanding about the morphology, chemical composition and crystallinity of the SEIs.

List of symbols and abbreviations

ALD	Atomic layer deposition
CPE	Constant phase element
DC	Direct current
DMC	Dimethyl carbonate
EC	Ethylene carbonate
EDX	Energy-dispersive X-ray
EIS	Electrochemical impedance spectroscopy
FIB-SEM	Focused ion beam-scanning electron microscopy
FT-IR	Fourier-transform infrared spectroscopy
ICP-OES	Inductively coupled plasma optical emission spectroscopy
LiTf	Lithium triflouromethanesulfonate
LUMO	Lowest unoccupied molecular orbital
MBE	Molecular beam epitaxy
NaTf	Sodium triflouromethanesulfonate
NMR	Nuclear magnetic resonance
SEI	Solid-electrolyte interphase
ToF-SIMS	Time-of-flight secondary ion mass spectroscopy
Triglyme	Triethylene glycol dimethyl ether
XPS	X-ray photoelectron spectroscopy
XRD	X-ray diffraction

f_{peak}	Frequency where $\lvert Z_{Im}\rvert$ becomes maximum in a semicircle
$\Delta_{\mathrm{R}}\mathrm{G}$	Gibbs free energy change over the reaction
R_{SEI}	SEI resistance
k_B	Boltzmann constant
C	Capacitance
c	Concentration of ions
E_a	Activation energy
F	Faraday constant
I	Current
J	Particle flux density
R_{bulk}	Resistance of bulk electrolyte
R_{PB}	Pilling-Bedworth ratio
t	Transference number
A	Surface area
D	Diffusion coefficient
L	Diffusion length
N	Number of moles
U	Voltage
V	Molar volume
Z	Impedance
d	Thickness
u	Mobility of ions
z	Charge number
ε	Dielectric constant (permittivity)
μ	Chemical potential
σ	Ionic conductivity
τ	Relaxation time

Acknowledgements

My motivation for joining Max Planck Institute was that I wished to perform my research in a fundamental way to train logical thinking, rigorous data analysis and problem solving. During my PhD years, I believe that I have achieved what I have sought. However, this would not have been so successful without the help of many people.

First and foremost, I feel a profound gratitude to my PhD advisor, Prof. Joachim Maier for a wonderful academic guidance and supports. Whenever I had a discussion with my advisor, I had always been impressed about his insights into the nature of the materials. Also, the atmosphere of our department is always very friendly and delightful, so that I was able to be emotionally stabilized and to focus on my studies. This would have never been achieved without his continuous efforts.

I am deeply thankful for my day-to-day supervisor, Dr. Jelena Popovic-Neuber. She has always been so supportive and welcoming for any kinds of discussion. I have found that she is a great scientist, full of motivation and enthusiasm, not only academically but also in regard to her general attitude about science. Discussing with her has always been a great pleasure for me.

Sincerely many thanks to our secretaries, Sofia Weiglein and Madeleine Burkhardt, who always kindly supported administrative things. Also, I feel so grateful for Birgit King who took care of my registration in Germany and visa. Thanks for their help, I was able to go through the complicated administrative process in Germany.

I feel so grateful to the technicians from our group. Florian Kaiser is an amazing technician whom I have never met in my life before. Udo Klock, Annette Fuchs, Arming Sorg and Uwe Traub are very professional and always willing to help me. Also, many thanks to Dr. Rotraut Merkle, Dr. Klaus-Dieter Kreuer and Dr. Davide Moia for scientific discussions.

My PhD works required lots of challenging characterizations since I dealt with one of the most reactive materials in the earth. I would like to thank for the people of Nanostructuring lab; Dr. Jürgen Weis who is a group leader of the lab and also a member of my annual thesis committee meeting. Bernhard Fenk and Ulrike Waizmann also put tremendous efforts on measuring my samples with FIB-SEM, which was very challenging. Marion Hagel kindly synthesized Al_2O_3 on my samples. Many thanks to Dr. Kathrin Küster and Tolga Acartürk for interface analyses with

XPS and ToF-SIMS. I am also grateful for Samir Hammoud who carried out ICP-OES measurements. I am so thankful for Dr. Helga Hoier who performed a number of XRD measurements for my samples. I deeply appreciate Julia Deuschle and Tobias Heil for trying out measuring my Li samples with cryo-TEM, which now appears to be very challenging. Thanks to Armin Schulz who performed Raman on my samples.

I also would like to express my gratitude to Dr. Robert Usiskin, who was always cheerful and open to any kind of discussions. He provided me many scientific ideas and introduced me how to run MBE.

Many thanks to my fellow PhD students who made my daily life much more energetic and joyful: Dr. Andreas Münchinger, Dr. Torben Saatkamp and Dr. Simon Lorger who shared the office with me, Chuanlian Xiao, Dr. Giulia Raimondi, Dr. Yuanye Huang, Dr. Markus Joos, Ya-Ru Wang, Dr. Maximilian Hödl and Mina Jung. Also, thanks to Dr. Christian Berger, Dr. Chuanhai Gan, Dr. Eugene Kotomin, Dr. Igor Moudrakovski and Dr. Yue Zhu.

Special thanks to Dr. Gee Yeong Kim and Dr. Minjae Kim who mentally helped me a lot in the beginning of my PhD years. We have spent lots of greatest moments together in Stuttgart and I will never forget about them.

The final greatest thanks go to my family, my parents and two sisters. Their presence itself has already been my mental support, based on which I was able to go through all the challenges of my PhD studies. I thank to my fiancé, Dr. Hun-ho Kim who provided the endless support during my entire PhD years.

References

[1] J. Maier, Conductivity in an activity gradient, Journal of Physics and Chemistry of Solids, 46 (1985) 197-200.

[2] B. Gates, How to Avoid a Climate Disaster, Alfred A. Knopf, United States (2021).

[3] S. Chu, A. Majumdar, Opportunities and challenges for a sustainable energy future, Nature, 488 (2012) 294-303.

[4] O. Inderwildi, D. King, Energy, transport & the environment, Springer (2012).

[5] A. Kalair, N. Abas, M.S. Saleem, A.R. Kalair, N. Khan, Role of energy storage systems in energy transition from fossil fuels to renewables, Energy Storage, 3 (2021) e135.

[6] W. Xu, J. Wang, F. Ding, X. Chen, E. Nasybulin, Y. Zhang, J.-G. Zhang, Lithium metal anodes for rechargeable batteries, Energy & Environmental Science, 7 (2014) 513-537.

[7] B. Lee, E. Paek, D. Mitlin, S.W. Lee, Sodium Metal Anodes: Emerging Solutions to Dendrite Growth, Chemical Reviews, 119 (2019) 5416-5460.

[8] H. Wu, H. Jia, C. Wang, J.-G. Zhang, W. Xu, Recent Progress in Understanding Solid Electrolyte Interphase on Lithium Metal Anodes, Advanced Energy Materials, 11 (2021) 2003092.

[9] J. Popovic, The importance of electrode interfaces and interphases for rechargeable metal batteries, Nature Communications, 12 (2021) 6240.

[10] J. Popovic, 10 - Nanostructured alkali and alkaline earth metal interfaces for high-energy batteries, in: R. Raccichini, U. Ulissi (Eds.) Frontiers of Nanoscience, Elsevier (2021) 327-359.

[11] E. Peled, S. Menkin, Review—SEI: Past, Present and Future, Journal of The Electrochemical Society, 164 (2017) A1703-A1719.

[12] E. Peled, D. Golodnttsky, G. Ardel, C. Menachem, D.B. Tow, V. Eshkenazy, The role of SEI in lithium and lithium ion batteries, MRS Online Proceedings Library, (1995) 393.

[13] M.D. Tikekar, S. Choudhury, Z. Tu, L. Archer, Design principles for electrolytes and interfaces for stable lithium-metal batteries, Nature Energy, 1 (2016) 1-7.

[14] E. Peled, The electrochemical behavior of alkali and alkaline earth metals in nonaqueous battery systems—the solid electrolyte interphase model, Journal of The Electrochemical Society, 126 (1979) 2047.

[15] A. Wang, S. Kadam, H. Li, S. Shi, Y. Qi, Review on modeling of the anode solid electrolyte interphase (SEI) for lithium-ion batteries, npj Computational Materials, 4 (2018) 15.

[16] P. Verma, P. Maire, P. Novák, A review of the features and analyses of the solid electrolyte interphase in Li-ion batteries, Electrochimica Acta, 55 (2010) 6332-6341.

[17] E. Matios, H. Wang, C. Wang, W. Li, Enabling Safe Sodium Metal Batteries by Solid Electrolyte Interphase Engineering: A Review, Industrial & Engineering Chemistry Research, 58 (2019) 9758-9780.

[18] X. Shan, Y. Zhong, L. Zhang, Y. Zhang, X. Xia, X. Wang, J. Tu, A Brief Review on Solid Electrolyte Interphase Composition Characterization Technology for Lithium Metal Batteries: Challenges and Perspectives, The Journal of Physical Chemistry C, 125 (2021) 19060-19080.

[19] X.-B. Cheng, R. Zhang, C.-Z. Zhao, Q. Zhang, Toward Safe Lithium Metal Anode in Rechargeable Batteries: A Review, Chemical Reviews, 117 (2017) 10403-10473.

[20] K.J. Kim, M. Balaish, M. Wadaguchi, L. Kong, J.L.M. Rupp, Solid-State Li–Metal Batteries: Challenges and Horizons of Oxide and Sulfide Solid Electrolytes and Their Interfaces, Advanced Energy Materials, 11 (2021) 2002689.

[21] W. Liu, P. Liu, D. Mitlin, Review of Emerging Concepts in SEI Analysis and Artificial SEI Membranes for Lithium, Sodium, and Potassium Metal Battery Anodes, Advanced Energy Materials, 10 (2020) 2002297.

[22] S. Lorger, R.E. Usiskin, J. Maier, Transport and Charge Carrier Chemistry in Lithium Sulfide, Advanced Functional Materials, 29 (2019) 1807688.

[23] B. Bertheville, D. Low, H. Bill, F. Kubel, Ionic conductivity of Na2S single crystals between 295 and 1350 K experimental setup and first results, Journal of Physics and Chemistry of Solids, 58 (1997) 1569-1577.

[24] J. Maier, Physical chemistry of ionic materials: ions and electrons in solids, John Wiley & Sons (2004).

[25] J.B. Goodenough, Y. Kim, Challenges for Rechargeable Li Batteries, Chemistry of Materials, 22 (2010) 587-603.

[26] T. Thompson, S. Yu, L. Williams, R.D. Schmidt, R. Garcia-Mendez, J. Wolfenstine, J.L. Allen, E. Kioupakis, D.J. Siegel, J. Sakamoto, Electrochemical Window of the Li-Ion Solid Electrolyte Li7La3Zr2O12, ACS Energy Letters, 2 (2017) 462-468.

[27] B.V. Lotsch, J. Maier, Relevance of solid electrolytes for lithium-based batteries: A realistic view, Journal of Electroceramics, 38 (2017) 128-141.

[28] Y. Zhang, T.-T. Zuo, J. Popovic, K. Lim, Y.-X. Yin, J. Maier, Y.-G. Guo, Towards better Li metal anodes: Challenges and strategies, Materials Today, 33 (2020) 56-74.

[29] E. Peled, D. Golodnitsky, J. Penciner, Handbook of Battery Materials, Wiley-VCH1999.

[30] K. Xu, Electrolytes and Interphases in Li-Ion Batteries and Beyond, Chemical Reviews, 114 (2014) 11503-11618.

[31] D. Aurbach, M.L. Daroux, P.W. Faguy, E. Yeager, Identification of Surface Films Formed on Lithium in Propylene Carbonate Solutions, Journal of The Electrochemical Society, 134 (1987) 1611-1620.

[32] D. Aurbach, B. Markovsky, M.D. Levi, E. Levi, A. Schechter, M. Moshkovich, Y. Cohen, New insights into the interactions between electrode materials and electrolyte solutions for advanced nonaqueous batteries, Journal of Power Sources, 81-82 (1999) 95-111.

[33] S. Shi, P. Lu, Z. Liu, Y. Qi, L.G. Hector, H. Li, S.J. Harris, Direct Calculation of Li-Ion Transport in the Solid Electrolyte Interphase, Journal of the American Chemical Society, 134 (2012) 15476-15487.

[34] P. Lu, S.J. Harris, Lithium transport within the solid electrolyte interphase, Electrochemistry Communications 13 (2011) 1035-1037.

[35] A.M. Tripathi, W.-N. Su, B.J. Hwang, In situ analytical techniques for battery interface analysis, Chemical Society Reviews, 47 (2018) 736-851.

[36] Z. Zhang, Y. Li, R. Xu, W. Zhou, Y. Li, S.T. Oyakhire, Y. Wu, J. Xu, H. Wang, Z. Yu, D.T. Boyle, W. Huang, Y. Ye, H. Chen, J. Wan, Z. Bao, W. Chiu, Y. Cui, Capturing the swelling of solid-electrolyte interphase in lithium metal batteries, Science, 375 (2022) 66-70.

[37] M.J. Zachman, Z. Tu, S. Choudhury, L.A. Archer, L.F. Kourkoutis, Cryo-STEM mapping of solid–liquid interfaces and dendrites in lithium-metal batteries, Nature, 560 (2018) 345-349.

[38] B. Han, Z. Zhang, Y. Zou, K. Xu, G. Xu, H. Wang, H. Meng, Y. Deng, J. Li, M. Gu, Poor Stability of Li2CO3 in the Solid Electrolyte Interphase of a Lithium-Metal Anode Revealed by Cryo-Electron Microscopy, Advanced Materials, 33 (2021) 2100404.

[39] A.C. Thenuwara, P.P. Shetty, N. Kondekar, S.E. Sandoval, K. Cavallaro, R. May, C.-T. Yang, L.E. Marbella, Y. Qi, M.T. McDowell, Efficient Low-Temperature Cycling of Lithium Metal Anodes by Tailoring the Solid-Electrolyte Interphase, ACS Energy Letters, 5 (2020) 2411-2420.

[40] V. Vanpeene, J. Villanova, J.-P. Suuronen, A. King, A. Bonnin, J. Adrien, E. Maire, L. Roué, Monitoring the morphological changes of Si-based electrodes by X-ray computed tomography: A 4D-multiscale approach, Nano Energy, 74 (2020) 104848.

[41] Z. Shadike, H. Lee, O. Borodin, X. Cao, X. Fan, X. Wang, R. Lin, S.-M. Bak, S. Ghose, K. Xu, C. Wang, J. Liu, J. Xiao, X.-Q. Yang, E. Hu, Identification of LiH and nanocrystalline LiF in the solid–electrolyte interphase of lithium metal anodes, Nature Nanotechnology, 16 (2021) 549-554.

[42] C. Cao, M.F. Toney, T.-K. Sham, R. Harder, P.R. Shearing, X. Xiao, J. Wang, Emerging X-ray imaging technologies for energy materials, Materials Today, 34 (2020) 132-147.

[43] A.J. Ilott, A. Jerschow, Probing Solid-Electrolyte Interphase (SEI) Growth and Ion Permeability at Undriven Electrolyte–Metal Interfaces Using 7Li NMR, The Journal of Physical Chemistry C, 122 (2018) 12598-12604.

[44] M. Nie, D.P. Abraham, Y. Chen, A. Bose, B.L. Lucht, Silicon Solid Electrolyte Interphase (SEI) of Lithium Ion Battery Characterized by Microscopy and Spectroscopy, The Journal of Physical Chemistry C, 117 (2013) 13403-13412.

[45] A.B. Gunnarsdóttir, S. Vema, S. Menkin, L.E. Marbella, C.P. Grey, Investigating the effect of a fluoroethylene carbonate additive on lithium deposition and the solid electrolyte interphase in lithium metal batteries using in situ NMR spectroscopy, Journal of Materials Chemistry A, 8 (2020) 14975-14992.

[46] Y.-C. Hsieh, J.H. Thienenkamp, C.-J. Huang, H.-C. Tao, U. Rodehorst, B.J. Hwang, M. Winter, G. Brunklaus, Revealing the Impact of Film-Forming Electrolyte Additives on Lithium Metal Batteries via Solid-State NMR/MRI Analysis, The Journal of Physical Chemistry C, 125 (2021) 252-265.

[47] Y. Xiang, G. Zheng, Z. Liang, Y. Jin, X. Liu, S. Chen, K. Zhou, J. Zhu, M. Lin, H. He, J. Wan, S. Yu, G. Zhong, R. Fu, Y. Li, Y. Yang, Visualizing the growth process of sodium microstructures in sodium batteries by in-situ 23Na MRI and NMR spectroscopy, Nature Nanotechnology, 15 (2020) 883-890.

[48] N. Schulz, R. Hausbrand, L. Dimesso, W. Jaegermann, XPS-surface analysis of SEI layers on Li-ion cathodes: Part I. Investigation of initial surface chemistry, Journal of The Electrochemical Society, 165 (2018) A819.

[49] N. Schulz, R. Hausbrand, C. Wittich, L. Dimesso, W. Jaegermann, XPS-surface analysis of SEI layers on Li-ion cathodes: Part II. SEI-composition and formation inside composite electrodes, Journal of The Electrochemical Society 165 (2018) A833.

[50] N. Galushkin, N. Yazvinskaya, D. Galushkin, Mechanism of gases generation during lithium-ion batteries cycling, Journal of The Electrochemical Society, 166 (2019) A897.

[51] B. Rowden, N. Garcia-Araez, A review of gas evolution in lithium ion batteries, Energy Reports 6 (2020) 10-18.

[52] Y. Wang, S. Nakamura, M. Ue, P.B. Balbuena, Theoretical studies to understand surface chemistry on carbon anodes for lithium-ion batteries: reduction mechanisms of ethylene carbonate, Journal of the American Chemical Society 123 (2001) 11708-11718.

[53] O. Borodin, M. Olguin, C.E. Spear, K.W. Leiter, J. Knap, Towards high throughput screening of electrochemical stability of battery electrolytes, Nanotechnology, 26 (2015) 354003.

[54] K. Leung, J.L. Budzien, Ab initio molecular dynamics simulations of the initial stages of solid–electrolyte interphase formation on lithium ion battery graphitic anodes, Physical Chemistry Chemical Physics 12 (2010) 6583-6586.

[55] K. Tasaki, K. Kanda, S. Nakamura, M. Ue, Decomposition of LiPF6 and Stability of PF5 in Li-Ion Battery Electrolytes, Journal of The Electrochemical Society, 150 (2003) A1628.

[56] E.W.C. Spotte-Smith, R.L. Kam, D. Barter, X. Xie, T. Hou, S. Dwaraknath, S.M. Blau, K.A. Persson, Towards a Mechanistic Model of Solid-Electrolyte Interphase Formation and Evolution in Lithium-ion Batteries, Chemrxiv, (2022).

[57] N. Perez, Kinetics of activation polarization, Electrochemistry and corrosion science, Springer (2016) 101-150.

[58] M. Broussely, S. Herreyre, P. Biensan, P. Kasztejna, K. Nechev, R.J. Staniewicz, Aging mechanism in Li ion cells and calendar life predictions, Journal of Power Sources, 97-98 (2001) 13-21.

[59] J. Christensen, J. Newman, A Mathematical Model for the Lithium-Ion Negative Electrode Solid Electrolyte Interphase, Journal of The Electrochemical Society, 151 (2004) A1977.

[60] M. Tang, S. Lu, J. Newman, Experimental and Theoretical Investigation of Solid-Electrolyte-Interphase Formation Mechanisms on Glassy Carbon, Journal of The Electrochemical Society, 159 (2012) A1775-A1785.

[61] M.B. Pinson, M.Z. Bazant, Theory of SEI Formation in Rechargeable Batteries: Capacity Fade, Accelerated Aging and Lifetime Prediction, Journal of The Electrochemical Society, 160 (2012) A243-A250.

[62] H.J. Ploehn, P. Ramadass, R.E. White, Solvent Diffusion Model for Aging of Lithium-Ion Battery Cells, Journal of The Electrochemical Society, 151 (2004) A456.

[63] C.J.Z.f.p.C. Wagner, Beitrag zur theorie des anlaufvorgangs, 21 (1933) 25-41.

[64] U.R. Evans, The Mechanism of Oxidation and Tarnishing, Transactions of The Electrochemical Society, 91 (1947) 547.

[65] B.E. Deal, A.S. Grove, General Relationship for the Thermal Oxidation of Silicon, Journal of Applied Physics, 36 (1965) 3770-3778.

[66] N. Cabrera, N.F. Mott, Theory of the oxidation of metals, Reports on Progress in Physics, 12 (1949) 163-184.

[67] P.M. Attia, W.C. Chueh, S.J. Harris, Revisiting the t0.5 Dependence of SEI Growth, Journal of The Electrochemical Society, 167 (2020) 090535.

[68] R. Usiskin, J. Maier, Interfacial Effects in Lithium and Sodium Batteries, Advanced Energy Materials, 11 (2021) 2001455.

[69] R.E. Bedworth, N.B. Pilling, The oxidation of metals at high temperatures, J Inst Met, 29 (1923) 529-582.

[70] S. Wenzel, S.J. Sedlmaier, C. Dietrich, W.G. Zeier, J. Janek, Interfacial reactivity and interphase growth of argyrodite solid electrolytes at lithium metal electrodes, Solid State Ionics, 318 (2018) 102-112.

[71] Z. Yu, D.G. Mackanic, W. Michaels, M. Lee, A. Pei, D. Feng, Q. Zhang, Y. Tsao, C.V. Amanchukwu, X. Yan, H. Wang, S. Chen, K. Liu, J. Kang, J. Qin, Y. Cui, Z. Bao, A Dynamic, Electrolyte-Blocking, and Single-Ion-Conductive Network for Stable Lithium-Metal Anodes, Joule, 3 (2019) 2761-2776.

[72] S. Lorger, R. Usiskin, J. Maier, Transport and charge carrier chemistry in lithium oxide, Journal of The Electrochemical Society 166 (2019) A2215.

[73] S. Shi, Y. Qi, H. Li, L.G. Hector, Defect Thermodynamics and Diffusion Mechanisms in Li2CO3 and Implications for the Solid Electrolyte Interphase in Li-Ion Batteries, The Journal of Physical Chemistry C, 117 (2013) 8579-8593.

[74] J. Pan, Y.-T. Cheng, Y. Qi, General method to predict voltage-dependent ionic conduction in a solid electrolyte coating on electrodes, Physical Review B, 91 (2015) 134116.

[75] J. Pan, Q. Zhang, X. Xiao, Y.-T. Cheng, Y. Qi, Design of Nanostructured Heterogeneous Solid Ionic Coatings through a Multiscale Defect Model, ACS Applied Materials & Interfaces, 8 (2016) 5687-5693.

[76] Q. Zhang, J. Pan, P. Lu, Z. Liu, M.W. Verbrugge, B.W. Sheldon, Y.-T. Cheng, Y. Qi, X. Xiao, Synergetic Effects of Inorganic Components in Solid Electrolyte Interphase on High Cycle Efficiency of Lithium Ion Batteries, Nano Letters, 16 (2016) 2011-2016.

[77] K. Lim, B. Fenk, J. Popovic, J. Maier, Porosity of Solid Electrolyte Interphases on Alkali Metal Electrodes with Liquid Electrolytes, ACS Applied Materials & Interfaces, 13 (2021) 51767-51774.

[78] C. Li, X. Guo, L. Gu, D. Samuelis, J. Maier, Ionic Space-Charge Depletion in Lithium Fluoride Thin Films on Sapphire (0001) Substrates, Advanced Functional Materials 21 (2011) 2901-2905.

[79] J. Mizusaki, H. Tagawa, K. Saito, K. Uchida, M. Tezuka, Lithium carbonate as a solid electrolyte, Solid State Ionics 53 (1992) 791-797.

[80] L. Schafzahl, H. Ehmann, M. Kriechbaum, J.r. Sattelkow, T. Ganner, H. Plank, M. Wilkening, S.A. Freunberger, Long-chain Li and Na alkyl carbonates as solid electrolyte interphase components: structure, ion transport, and mechanical properties, Chemistry of Materials 30 (2018) 3338-3345.

[81] R.T. Johnson Jr, R.M. Biefeld, J.D. Keck, Ionic conductivity in Li5AlO4 and LiOH, Materials Research Bulletin, 12 (1977) 577-587.

[82] C.F. Bauer, D.H. Whitmore, Ionic conductivity of sodium fluoride, Physica Status Solidi (b), 37 (1970) 585-598.

[83] P. Cerisier, F. Roux, A study of the electrical conductivity and transition points of sodium carbonate, Journal of Solid State Chemistry, 22 (1977) 245-251.

[84] M. Spaeth, K. Kreuer, T. Dippel, J. Maier, Proton transport phenomena in pure alkaline metal hydroxides, Solid State Ionics 97 (1997) 291-297.

[85] N. von Aspern, G.-V. Röschenthaler, M. Winter, I. Cekic-Laskovic, Fluorine and Lithium: Ideal Partners for High-Performance Rechargeable Battery Electrolytes, Angewandte Chemie, 58 (2019) 15978-16000.

[86] L. Suo, Y.-S. Hu, H. Li, M. Armand, L. Chen, A new class of Solvent-in-Salt electrolyte for high-energy rechargeable metallic lithium batteries, Nature Communications, 4 (2013) 1481.

[87] J. Qian, W.A. Henderson, W. Xu, P. Bhattacharya, M. Engelhard, O. Borodin, J.G. Zhang, High rate and stable cycling of lithium metal anode, Nature Communications, 6 (2015) 6362.

[88] F. Ding, W. Xu, G.L. Graff, J. Zhang, M.L. Sushko, X. Chen, Y. Shao, M.H. Engelhard, Z. Nie, J. Xiao, X. Liu, P.V. Sushko, J. Liu, J.G. Zhang, Dendrite-free lithium deposition via self-healing electrostatic shield mechanism, Journal of the American Chemical Society 135 (2013) 4450-4456.

[89] Y. Zhang, J. Qian, W. Xu, S.M. Russell, X. Chen, E. Nasybulin, P. Bhattacharya, M.H. Engelhard, D. Mei, R. Cao, Dendrite-free lithium deposition with self-aligned nanorod structure, Nano Letters, 14 (2014) 6889-6896.

[90] R. Xu, X.-B. Cheng, C. Yan, X.-Q. Zhang, Y. Xiao, C.-Z. Zhao, J.-Q. Huang, Q. Zhang, Artificial Interphases for Highly Stable Lithium Metal Anode, Matter, 1 (2019) 317-344.

[91] X.-B. Cheng, R. Zhang, C.-Z. Zhao, F. Wei, J.-G. Zhang, Q. Zhang, A Review of Solid Electrolyte Interphases on Lithium Metal Anode, Advanced Science, 3 (2016) 1500213.

[92] D. Kang, M. Xiao, J.P. Lemmon, Artificial Solid-Electrolyte Interphase for Lithium Metal Batteries, Batteries&Supercaps, 4 (2021) 445-455.

[93] P. Zhai, L. Liu, X. Gu, T. Wang, Y. Gong, Interface Engineering for Lithium Metal Anodes in Liquid Electrolyte, Advanced Energy Materials, 10 (2020) 2001257.

[94] L. Fan, X. Li, Recent advances in effective protection of sodium metal anode, Nano Energy, 53 (2018) 630-642.

[95] T. Wang, Y. Hua, Z. Xu, J.S. Yu, Recent Advanced Development of Artificial Interphase Engineering for Stable Sodium Metal Anodes, Small, 18 2102250.

[96] G. Zheng, S.W. Lee, Z. Liang, H.-W. Lee, K. Yan, H. Yao, H. Wang, W. Li, S. Chu, Y. Cui, Interconnected hollow carbon nanospheres for stable lithium metal anodes, Nature Nanotechnology 9 (2014) 618-623.

[97] N.-W. Li, Y.-X. Yin, C.-P. Yang, Y.-G. Guo, An Artificial Solid Electrolyte Interphase Layer for Stable Lithium Metal Anodes, Advanced Materials 28 (2016) 1853-1858.

[98] A.C. Kozen, C.-F. Lin, A.J. Pearse, M.A. Schroeder, X. Han, L. Hu, S.-B. Lee, G.W. Rubloff, M. Noked, Next-Generation Lithium Metal Anode Engineering via Atomic Layer Deposition, ACS Nano 9 (2015) 5884-5892.

[99] B. Zhu, Y. Jin, X. Hu, Q. Zheng, S. Zhang, Q. Wang, J. Zhu, Poly(dimethylsiloxane) Thin Film as a Stable Interfacial Layer for High-Performance Lithium-Metal Battery Anodes, Advanced Materials 29 (2017) 1603755.

[100] J. Xie, L. Liao, Y. Gong, Y. Li, F. Shi, A. Pei, J. Sun, R. Zhang, B. Kong, R. Subbaraman, J. Christensen, Y. Cui, Stitching h-BN by atomic layer deposition of LiF as a stable interface for lithium metal anode., Science Advances, 3 (2017) eaao3170.

[101] Y. Liu, D. Lin, P.Y. Yuen, K. Liu, J. Xie, R.H. Dauskardt, Y. Cui, An Artificial Solid Electrolyte Interphase with High Li-Ion Conductivity, Mechanical Strength, and Flexibility for Stable Lithium Metal Anodes, Advanced Materials, 29 (2017) 1605531.

[102] C. Yang, B. Liu, F. Jiang, Y. Zhang, H. Xie, E. Hitz, L. Hu, Garnet/polymer hybrid ion-conducting protective layer for stable lithium metal anode, Nano Research, 10 (2017) 4256-4265.

[103] F. Marchini, B. Porcheron, G. Rousse, L. Albero Blanquer, L. Droguet, D. Foix, T. Koç, M. Deschamps, J.M. Tarascon, The Hidden Side of Nanoporous β-Li3PS4 Solid Electrolyte, Advanced Energy Materials, 11 (2021) 2101111.

[104] A. Miura, N.C. Rosero-Navarro, A. Sakuda, K. Tadanaga, N.H.H. Phuc, A. Matsuda, N. Machida, A. Hayashi, M. Tatsumisago, Liquid-phase syntheses of sulfide electrolytes for all-solid-state lithium battery, Nature Reviews Chemistry, 3 (2019) 189-198.

[105] P. Mirmira, J. Zheng, P. Ma, C.V. Amanchukwu, Importance of multimodal characterization and influence of residual Li2S impurity in amorphous Li3PS4 inorganic electrolytes, Journal of Materials Chemistry A, 9 (2021) 19637-19648.

[106] H.-D. Lim, X. Yue, X. Xing, V. Petrova, M. Gonzalez, H. Liu, P. Liu, Designing solution chemistries for the low-temperature synthesis of sulfide-based solid electrolytes, Journal of Materials Chemistry A, 6 (2018) 7370-7374.

[107] E.C. Self, Z.D. Hood, T. Brahmbhatt, F.M. Delnick, H.M. Meyer, G. Yang, J.L.M. Rupp, J. Nanda, Solvent-Mediated Synthesis of Amorphous Li3PS4/Polyethylene Oxide Composite Solid Electrolytes with High Li+ Conductivity, Chemistry of Materials, 32 (2020) 8789-8797.

[108] M. Takahashi, S. Yang, K. Yamamoto, K. Ohara, N.H.H. Phuc, T. Watanabe, T. Uchiyama, A. Sakuda, A. Hayashi, M. Tatsumisago, H. Muto, A. Matsuda, Y. Uchimoto, Improvement of lithium ionic conductivity of Li3PS4 through suppression of crystallization using low-boiling-point solvent in liquid-phase synthesis, Solid State Ionics, 361 (2021) 115568.

[109] A. Hayashi, K. Noi, N. Tanibata, M. Nagao, M. Tatsumisago, High sodium ion conductivity of glass–ceramic electrolytes with cubic Na3PS4, Journal of Power Sources, 258 (2014) 420-423.

[110] A. Hayashi, K. Noi, A. Sakuda, M. Tatsumisago, Superionic glass-ceramic electrolytes for room-temperature rechargeable sodium batteries, Nature Communications, 3 (2012) 856.

[111] K.M. Abraham, S.M. Chaudhri, The Lithium Surface Film in the Li / SO 2 Cell, Journal of The Electrochemical Society, 133 (1986) 1307-1311.

[112] K.N. Wood, G. Teeter, XPS on Li-Battery-Related Compounds: Analysis of Inorganic SEI Phases and a Methodology for Charge Correction, ACS Applied Energy Materials, 1 (2018) 4493-4504.

[113] M. Fantauzzi, B. Elsener, D. Atzei, A. Rigoldi, A. Rossi, Exploiting XPS for the identification of sulfides and polysulfides, RSC Advances, 5 (2015) 75953-75963.

[114] K. Mc Carthy, H. Gullapalli, K.M. Ryan, T. Kennedy, Review—Use of Impedance Spectroscopy for the Estimation of Li-ion Battery State of Charge, State of Health and Internal Temperature, Journal of The Electrochemical Society, 168 (2021) 080517.

[115] H. Nara, T. Yokoshima, T. Osaka, Technology of electrochemical impedance spectroscopy for an energy-sustainable society, Current Opinion in Electrochemistry, 20 (2020) 66-77.

[116] M. Gaberšček, Understanding Li-based battery materials via electrochemical impedance spectroscopy, Nature Communications, 12 (2021) 6513.

[117] N. Meddings, M. Heinrich, F. Overney, J.-S. Lee, V. Ruiz, E. Napolitano, S. Seitz, G. Hinds, R. Raccichini, M. Gaberšček, J. Park, Application of electrochemical impedance

spectroscopy to commercial Li-ion cells: A review, Journal of Power Sources, 480 (2020) 228742.

[118] S. Wang, J. Zhang, O. Gharbi, V. Vivier, M. Gao, M.E. Orazem, Electrochemical impedance spectroscopy, Nature Reviews Methods Primers, 1 (2021) 41.

[119] F.T. Krauss, I. Pantenburg, B. Roling, Transport of Ions, Molecules, and Electrons across the Solid Electrolyte Interphase: What Is Our Current Level of Understanding?, Advanced Materials Interfaces, 9 (2022) 2101891.

[120] R.R. Gaddam, L. Katzenmeier, X. Lamprecht, A.S. Bandarenka, Review on physical impedance models in modern battery research, Physical Chemistry Chemical Physics, 23 (2021) 12926-12944.

[121] R. Koch, R. Kuhn, I. Zilberman, A. Jossen, Electrochemical impedance spectroscopy for online battery monitoring - power electronics control, 2014 16th European Conference on Power Electronics and Applications, (2014), 1-10.

[122] M. E. Orazem, B. Tribollet, Electrochemical impedance spectroscopy, John Wiley & Sons, Inc.2008.

[123] J. Fleig, The grain boundary impedance of random microstructures: numerical simulations and implications for the analysis of experimental data, Solid State Ionics, 150 (2002) 181-193.

[124] P. Ravn Sørensen, T. Jacobsen, Conductivity, charge transfer and transport number—an ac-investigation of the polymer electrolyte LiSCN-poly(ethyleneoxide), Electrochimica Acta, 27 (1982) 1671-1675.

[125] S.-K. Otto, T. Fuchs, Y. Moryson, C. Lerch, B. Mogwitz, J. Sann, J. Janek, A. Henss, Storage of Lithium Metal: The Role of the Native Passivation Layer for the Anode Interface Resistance in Solid State Batteries, ACS Applied Energy Materials, 4 (2021) 12798-12807.

[126] A. Schechter, D. Aurbach, H. Cohen, X-ray Photoelectron Spectroscopy Study of Surface Films Formed on Li Electrodes Freshly Prepared in Alkyl Carbonate Solutions, Langmuir, 15 (1999) 3334-3342.

[127] S.M. Nojabaee, Interfacial Effects in Solid-Liquid Glyme-Based Electrolytes for Lithium Batteries, Max-Planck-Institut für Festkörperforschung, Universität Stuttgart, (2018).

[128] R.E. Honig, Vapor pressure data for the more commen elements, Radio Corporation of America, RCA Laboratories, Industry Service Laboratory, (1957).

[129] E. Peled, D. Golodnitsky, G. Ardel, V. Eshkenazy, The sei model—application to lithium-polymer electrolyte batteries, Electrochimica Acta, 40 (1995) 2197-2204.

[130] T.Q. Nguyen, C. Breitkopf, Determination of Diffusion Coefficients Using Impedance Spectroscopy Data, Journal of The Electrochemical Society, 165 (2018) E826-E831.

[131] R. Demir-Cakan, M. Morcrette, F. Nouar, C. Davoisne, T. Devic, D. Gonbeau, R. Dominko, C. Serre, G. Férey, J.-M. Tarascon, Cathode Composites for Li–S Batteries via the Use of Oxygenated Porous Architectures, Journal of the American Chemical Society, 133 (2011) 16154-16160.

[132] C. Niu, H. Lee, S. Chen, Q. Li, J. Du, W. Xu, J.-G. Zhang, M.S. Whittingham, J. Xiao, J. Liu, High-energy lithium metal pouch cells with limited anode swelling and long stable cycles, Nature Energy, 4 (2019) 551-559.

[133] J. Maier, Concentration Polarization of Salt-Containing Liquid Electrolytes, 21 (2011) 1448-1455.

[134] C. Brissot, M. Rosso, J.N. Chazalviel, S. Lascaud, Dendritic growth mechanisms in lithium/polymer cells, Journal of Power Sources, 81-82 (1999) 925-929.

[135] P. Bai, J. Li, F.R. Brushett, M.Z. Bazant, Transition of lithium growth mechanisms in liquid electrolytes, Energy & Environmental Science, 9 (2016) 3221-3229.

[136] R. Usiskin, Y. Lu, J. Popovic, M. Law, P. Balaya, Y.-S. Hu, J. Maier, Fundamentals, status and promise of sodium-based batteries, Nature Reviews Materials, (2021).

[137] G. Liu, W. Lu, A model of concurrent lithium dendrite growth, SEI growth, SEI penetration and regrowth, Journal of the Electrochemical Society, 164 (2017) A1826.

[138] D.I. Iermakova, R. Dugas, M.R. Palacín, A. Ponrouch, On the Comparative Stability of Li and Na Metal Anode Interfaces in Conventional Alkyl Carbonate Electrolytes, Journal of The Electrochemical Society, 162 (2015) A7060-A7066.

[139] M. Mandl, J. Becherer, D. Kramer, R. Mönig, T. Diemant, R.J. Behm, M. Hahn, O. Böse, M.A. Danzer, Sodium metal anodes: Deposition and dissolution behaviour and SEI formation, Electrochimica Acta, 354 (2020) 136698.

[140] T. Osaka, T. Momma, D. Mukoyama, H. Nara, Proposal of novel equivalent circuit for electrochemical impedance analysis of commercially available lithium ion battery, Journal of Power Sources, 205 (2012) 483-486.

[141] E. Peled, D. Golodnitsky, G. Ardel, Advanced Model for Solid Electrolyte Interphase Electrodes in Liquid and Polymer Electrolytes, Journal of The Electrochemical Society, 144 (1997) L208-L210.

[142] P. Gao, C. Zhang, G. Wen, Equivalent circuit model analysis on electrochemical impedance spectroscopy of lithium metal batteries, Journal of Power Sources, 294 (2015) 67-74.

[143] N. Yao, X. Chen, X. Shen, R. Zhang, Z.-H. Fu, X.-X. Ma, X.-Q. Zhang, B.-Q. Li, Q. Zhang, An Atomic Insight into the Chemical Origin and Variation of the Dielectric Constant in Liquid Electrolytes, Angewandte Chemie, 60 (2021) 21473-21478.

[144] I.N. Daniels, Z. Wang, B.B. Laird, Dielectric Properties of Organic Solvents in an Electric Field, The Journal of Physical Chemistry C, 121 (2017) 1025-1031.

[145] K.F. Young, H.P.R. Frederikse, Compilation of the Static Dielectric Constant of Inorganic Solids, Journal of Physical and Chemical Reference Data, 2 (1973) 313-410.

[146] J. Maier, G. Schwitzgebel, Conductance measurements on orthorhombic and on TiO2-stabilized tetragonal lead oxide, Materials Research Bulletin, 17 (1982) 1061-1069.

[147] J. Maier, Nanoionics: ion transport and electrochemical storage in confined systems, Nature Materials, 4 (2005) 805-815.

[148] C. Li, J. Maier, Ionic space charge effects in lithium fluoride thin films, Solid State Ionics, 225 (2012) 408-411.

[149] L.A. Ma, A.J. Naylor, L. Nyholm, R. Younesi, Strategies for Mitigating Dissolution of Solid Electrolyte Interphases in Sodium-Ion Batteries, Angewandte Chemie, 60 (2021) 4855-4863.

[150] R. Mogensen, D. Brandell, R. Younesi, Solubility of the Solid Electrolyte Interphase (SEI) in Sodium Ion Batteries, ACS Energy Letters, 1 (2016) 1173-1178.

[151] Z.W. Seh, J. Sun, Y. Sun, Y. Cui, A Highly Reversible Room-Temperature Sodium Metal Anode, ACS Central Science, 1 (2015) 449-455.

[152] L. Lutz, D. Alves Dalla Corte, M. Tang, E. Salager, M. Deschamps, A. Grimaud, L. Johnson, P.G. Bruce, J.-M. Tarascon, Role of Electrolyte Anions in the Na–O2 Battery: Implications for NaO2 Solvation and the Stability of the Sodium Solid Electrolyte Interphase in Glyme Ethers, Chemistry of Materials, 29 (2017) 6066-6075.

[153] M. Goktas, C. Bolli, J. Buchheim, E.J. Berg, P. Novák, F. Bonilla, T. Rojo, S. Komaba, K. Kubota, P. Adelhelm, Stable and Unstable Diglyme-Based Electrolytes for Batteries with Sodium or Graphite as Electrode, ACS Applied Materials & Interfaces, 11 (2019) 32844-32855.

[154] K. Lim, B. Fenk, K. Küster, T. Acartürk, J. Weiss, U. Starke, J. Popovic, J. Maier, Influence of Porosity of Sulfide-Based Artificial Solid Electrolyte Interphases on Their Performance with Liquid and Solid Electrolytes in Li and Na Metal Batteries, ACS Applied Materials & Interfaces, 14 (2022) 16147-16156.

[155] Properties of substance: lithium sulfide, Chemister.

[156] G. Lindberg, A. Larsson, M. Råberg, D. Boström, R. Backman, A. Nordin, Determination of thermodynamic properties of Na2S using solid-state EMF measurements, The Journal of Chemical Thermodynamics, 39 (2007) 44-48.

[157] R.A. Sharma, Equilibrium Phases in the Lithium-Sulfur System, Journal of The Electrochemical Society, 119 (1972) 1439.

[158] J. Sangster, A. Pelton, The Na-S (sodium-sulfur) system, Journal of phase equilibria, 18 (1997) 89.

[159] M.J. Klein, G.M. Veith, A. Manthiram, Chemistry of Sputter-Deposited Lithium Sulfide Films, Journal of the American Chemical Society, 139 (2017) 10669-10676.

[160] K. Hauffe, Scaling Processes in Metals and Alloys with Formation of Thick Protective Layers, Oxidation of Metals, Springer US, Boston, MA, (1995) 144-364.

[161] C. Xiao, R. Usiskin, J. Maier, Passivation Layers in Lithium and Sodium Batteries: Potential Profiles, Stabilities, and Voltage Drops, Advanced Functional Materials, 31 (2021) 2100938.

[162] S. Contarini, J.W. Rabalais, Ion bombardment-induced decomposition of Li and Ba sulfates and carbonates studied by X-ray photoelectron spectroscopy, Journal of Electron Spectroscopy and Related Phenomena, 35 (1985) 191-201.

[163] A. Manthiram, Y. Fu, S.-H. Chung, C. Zu, Y.-S. Su, Rechargeable Lithium–Sulfur Batteries, Chemical Reviews, 114 (2014) 11751-11787.

[164] Y.-X. Wang, B. Zhang, W. Lai, Y. Xu, S.-L. Chou, H.-K. Liu, S.-X. Dou, Room-Temperature Sodium-Sulfur Batteries: A Comprehensive Review on Research Progress and Cell Chemistry, Advanced Energy Materials, 7 (2017) 1602829.

[165] X. Fan, W. Sun, F. Meng, A. Xing, J. Liu, Advanced chemical strategies for lithium–sulfur batteries: A review, Green Energy & Environment, 3 (2018) 2-19.

[166] D. Kumar, S.K. Rajouria, S.B. Kuhar, D.K. Kanchan, Progress and prospects of sodium-sulfur batteries: A review, Solid State Ionics, 312 (2017) 8-16.

[167] H. Chen, A. Pei, D. Lin, J. Xie, A. Yang, J. Xu, K. Lin, J. Wang, H. Wang, F. Shi, D. Boyle, Y. Cui, Uniform High Ionic Conducting Lithium Sulfide Protection Layer for Stable Lithium Metal Anode, Advanced Energy Materials, 9 (2019) 1900858.

[168] W.D. Richards, L.J. Miara, Y. Wang, J.C. Kim, G. Ceder, Interface Stability in Solid-State Batteries, Chemistry of Materials, 28 (2016) 266-273.

[169] V. Lacivita, Y. Wang, S.-H. Bo, G. Ceder, Ab initio investigation of the stability of electrolyte/electrode interfaces in all-solid-state Na batteries, Journal of Materials Chemistry A, 7 (2019) 8144-8155.

[170] G. Nazri, Preparation, structure and ionic conductivity of lithium phosphide, Solid State Ionics, 34 (1989) 97-102.

[171] C. Hänsel, P.V. Kumar, D. Kundu, Stack Pressure Effect in Li3PS4 and Na3PS4 Based Alkali Metal Solid-State Cells: The Dramatic Implication of Interlayer Growth, Chemistry of Materials, 32 (2020) 10501-10510.

[172] S. Wenzel, D.A. Weber, T. Leichtweiss, M.R. Busche, J. Sann, J. Janek, Interphase formation and degradation of charge transfer kinetics between a lithium metal anode and highly crystalline Li7P3S11 solid electrolyte, Solid State Ionics, 286 (2016) 24-33.

[173] A. Kato, H. Kowada, M. Deguchi, C. Hotehama, A. Hayashi, M. Tatsumisago, XPS and SEM analysis between Li/Li3PS4 interface with Au thin film for all-solid-state lithium batteries, Solid State Ionics, 322 (2018) 1-4.

[174] S. Wenzel, T. Leichtweiss, D.A. Weber, J. Sann, W.G. Zeier, J. Janek, Interfacial Reactivity Benchmarking of the Sodium Ion Conductors Na3PS4 and Sodium β-Alumina for Protected Sodium Metal Anodes and Sodium All-Solid-State Batteries, ACS Applied Materials & Interfaces, 8 (2016) 28216-28224.

[175] H. Eickhoff, C. Dietrich, W. Klein, W.G. Zeier, T.F. Fässler, On the Crystal Structure and Conductivity of Na3P, Zeitschrift für Anorganische und Allgemeine Chemie, 647 (2021) 28-33.

[176] X.-f. Yu, G. Giorgi, H. Ushiyama, K. Yamashita, First-principles study of fast Na diffusion in Na3P, Chemical Physics Letters, 612 (2014) 129-133.

[177] K.-H. Chen, K.N. Wood, E. Kazyak, W.S. LePage, A.L. Davis, A.J. Sanchez, N.P. Dasgupta, Dead lithium: mass transport effects on voltage, capacity, and failure of lithium metal anodes, Journal of Materials Chemistry A, 5 (2017) 11671-11681.

[178] H. Wang, E. Matios, J. Luo, W. Li, Combining theories and experiments to understand the sodium nucleation behavior towards safe sodium metal batteries, Chemical Society Reviews, 49 (2020) 3783-3805.

[179] J.L. Barton, J.O. Bockris, apos, m., A.R.J.P. Ubbelohde, The electrolytic growth of dendrites from ionic solutions, Proceedings of the Royal Society A, 268 (1962) 485-505.

[180] Y. Zhao, L.V. Goncharova, A. Lushington, Q. Sun, H. Yadegari, B. Wang, W. Xiao, R. Li, X. Sun, Superior Stable and Long Life Sodium Metal Anodes Achieved by Atomic Layer Deposition, Advanced Materials, 29 (2017) 1606663.

[181] S.R. Pollack, C.E. Morris, Electron Tunneling through Asymmetric Films of Thermally Grown Al2O3, Journal of Applied Physics, 35 (1964) 1503-1512.

[182] H.J. Kim, S.Y. Cha, D.J. Choi, Memory characteristics of Al2O3/La2O3/Al2O3 multi-layer films with various blocking and tunnel oxide thicknesses, Materials Science in Semiconductor Processing, 13 (2010) 9-12.

[183] G. Ardel, D. Golodnitsky, E. Peled, Y. Wang, W. Gang, S. Bajue, S. Greenbaum, Bulk and interfacial ionic conduction in LiI/Al2O3 mixtures, Solid State Ionics, 113-115 (1998) 477-485.

[184] Y. Zhu, X. He, Y. Mo, Strategies Based on Nitride Materials Chemistry to Stabilize Li Metal Anode, Advanced Science 4 (2017) 1600517.